Development of polarimetric and emission pattern analysis : applied to determine a single nanoplatelet dipole

Thu-Loan Nguyen

THESE DE DOCTORAT DE L'UNIVERSITÉ PIERRE ET MARIE CURIE

Spécialité

La physique, de la particule à la matière condensée

Présentée par

Thu-Loan NGUYEN

Pour obtenir le grade de

DOCTEUR de l' UNIVERSITÉ PIERRE ET MARIE CURIE

Development of polarimetric and emission pattern analysis: Applied to determine a single nanoplatelet dipole

---

Thèse dirigée par Agnès MAITRE

à l'Institut des NanoSciences de Paris

soutenue le 26 Octobre 2017

devant le jury composé de:

Marie-Claire SCHANNE-KLEIN (Rapporteur)

Isabelle ROBERT-PHILIP (Rapporteur)

Nicolas TREPS

Alexandra FRAGOLA

Isabelle MAURIN

Agnès MAITRE (Directrice de thèse)

Contents

Acknowledgements

Since it may be one of my very few chances to express my genuine thanks to these great people in writing, I would be more verbose than normal. Honestly, to complete this PhD degree could not have been possible without the help and support from all of them: my supervisors, colleagues, friends and family.

First of all, I would like to send my deepest thanks and appreciation to my supervisor, Professor Agnes Maitre. From my very first day in the lab until now, her irreplaceable guidance and continuous encouragement have always enlightened me, even during tough times of my PhD. I greatly appreciate her enormous patience, insightful ideas, and effective suggestions to help me finish this huge amount of work. It has been an honor to have had a caring advisor like her. Our remarkable time working together will never be forgotten.

Next, I would like to extend my gratefulness to other advisors in the ′Nanostructures et optique′ group, Catherine Schwob and Jean-Marc Frigerio, for the precious help on my experimental work and stimulating discussions. My sincere gratitude goes to Laurent Coolen for the precious theoretical advices and Willy Daney de Marcillac for the crucial technical assistances. I also acknowledge Professor Benoit Dubertret and his group who had an initial support on this study. You all made it happen.

My great thanks go to Dr. Clotilde Lethiec, who is a recent PhD graduate of our research group. In many ways, her outstanding thesis bring to me the foundation and motivation for my own one. It should be acknowledged that some parts of this dissertation were cited from her articles. I am particularly grateful to Fu Feng, with whom I shared the experiments for about half of my PhD. Thank you very much for your concern, care, and attentions.

I would like to express my heartfelt appreciation to the students in my research group whom I have had such a pleasure working together: Celine Bourdillon, Guillaume Binard, Amit Raj Dhawan, Ali Mcheik, Juan Uriel Esparza, and the interns. Thanks to all of you, my time in INSP is really happy and enjoyable. Your contribution to not only my professional but

also my personal life has helped me to make this degree achievable.

The sincere thankfulness goes to my friends and collegues in Institute of Materials Science in Vietnam for their time and support. Moreover, I considered myself lucky to have meet many interesting friends outside work. I am grateful for all these invaluable memories. Among them, a special thanks to Nhu Y, Pheobe and Phuc, we spent such a wonderful time in Europe.

Lastly, I would like to thank the family Colomban for their kind hospitality when I finished up my degree. There are not enough words to describe my gratitude. Last but certainly not least, my thoughts and feelings go to my beloved family who have made what I am. I will always be grateful for your unconditional love and encouragement during all this time. The most special thanks to Dad and Mom, you have raised me with a love of science and always supported me in all my decisions even though it meant travelling thousands of miles away from home to live on a different continent. I am blessed with my little sister, who knew only to encourage and never complained about anything that she was affected from my absence during these years. I am deeply indebted to them, without their endless love, this work would never be completed. To you all, I dedicate this thesis. *Con cam on.*

Chapter 1

Introduction

1.1 Motivation

A source of single-photons, which emits individual photons at periodic intervals, is a key component for a vast range of applications using quantum technologies like quantum information, photonics, sensing, and so on [1–5]. Therefore, single-photon sources have become a hot subject for many different fields of research. Single-photon sources are generally considered as the whole complex of a single-photon emitter and supporting components required to serve for extracting single-photons in a determined direction. There have been recent papers reviewing on the single-photon emitters [1,6], extracting single-photons emitted in optical cavities [7], light coupling to nanoantennas [8] and metrology of single-photon sources and detectors [1, 9, 10].

Single-photon emitters could be designed and fabricated from highly luminescent semiconductor in the nano-sized structures; while extracting photons in a determined direction requires nanophotonics to enhance light-matter interactions. Among them, one can mention (i) resonant microcavities, in which a nanoemitter is embedded [7,11]; (ii) waveguides [12,13], or (iii) optical nanoantennas [14–16]. The physical properties, the potential applications and the recent developments in the field of nanoantennas have been reviewed in details by Lukas Novotny and Niek van Hulst [17]. The concept of optical antennas are emerging rapidly in modern physical optics. They are a counterpart working in visible regime of conventional radio wave and microwave antennas. They convert the optical radiation from free space into localized energy, and vice versa [17]. Therefore, they are able to manipulate and control the field at the sub-wavelength scale which could not be achieved normally due to the diffraction limit. Researchers find them very promising in order to enhance the performance and efficiency of photonic/plasmonic de-

vices. However, as optical wavelengths are at nanometer scale, the characteristic dimensions of an antenna working at optical frequencies are also in the nanometer range. Thanks to the increasingly important developments in nanoscience and nanotechnology, some optical antennas has been explored recently [14, 16–19]. As a nanoantenna has a vectorial field distribution, the coupling of the light emitted from a nanoemitter and the nanoantenna requires the overlap of the dipole of the emitter with the nanoantenna field. Therefore, a facile/reproducible technique to determine the orientation of the emitting dipole of a nanoemitter should be developed in order to maximize the coupling strength.

Different from the conventional antenna, feeding energy into an optical antenna can be done either from the far field [20] or from the near field by a local emitter [19, 21]. The latter offers the possibility of exciting a nanostructure at expected wavelength and position. Nano-sized emitters have already been utilized as light sources in a wide broad of applications such as optoelectronic devices [22, 23] or biosensors [24, 25]. Especially, the ability to tune the band-gap energies together with significant absorption cross sections and high photoluminescence quantum yields of semiconductor nanoemitter like quantum dots, nanoplatelets, and nanowires/nanorods make these nanostructures promising candidates for next generation photonic/plasmonic devices.

As mentioned above, the efficient coupling between nanoemitters and nanophotonic structures for achieving high directivity and fast dynamics needs the control and optimization of the emission properties including spectral range and dipolar orientation. In the case of nanoemitters embedded in optical cavities and nanoantennas, the spectral tuning of the emitter is necessary to get efficient coupling of the light emitted to the nanostructures′ modes. Spatial positioning of the nanoemitter at the location having maximum intensity of the resonant nanostructure mode and a proper orientation of the nanoemitter′s dipole with respect to the mode field of the structures are also crucial requirements. The two first conditions, spectral and spatial matching have been addressed by several strategies. In plasmonics, since resonances are spectrally broad, it is easy to achieve the matching. Although positioning of nanoemitters can be now successfully performed (for example by the in-situ optical lithography [16, 26]), the emitting dipolar orientation of an nanoemitter remains a challenge. Therefore, determining the dipolar orientation becomes a very important topic to make the coupling between nanoemitter and optical microcavity or antennas efficient. In other words, the determination of the orientation of the emitting dipole from a nanoemitter plays a great role in the fields of the single-photon sources.

In our team, we have started building a polarimetric method for determining the dipolar

orientation of a point source by analyzing its emission polarization and polarization anisotropy distribution [27]. We have also developed an analytical model to interpret the data in a range of possible experimental conditions. This polarimetric method gives accurate results, however, they are ambiguous as there are several dipolar situations which could lead to the same polarimetric data. In order to clarify the interpretations, we have improved the method by introducing a complementary emission pattern measurement. Particularly, the polarimetric method combining the emission polarization characterization and emission pattern imaging is applicable for all kinds of nanoemitters with high accuracy. This study is dedicated to both the numerical and experimental optimization for the setup. Since our aim is the orientation determination of an emitting dipole, the simulations and experiments are simultaneously discussed in each related chapter.

Our method determining the orientation of a nanoemitter with its properly electrical dipole will be applied for nanoplatelets made from highly luminescent semiconductor. Nanoplatelets have been grown from a wide variety of materials, but those made from semiconductors, which act as two-dimensional quantum wells, give very promising optical properties [28]. Recently, II-VI nanoplatelets such as CdSe or CdS have been investigated widely because of their high luminescence quantum yield [28–31].

In our case, we did our study on CdSe/CdS core/shell structure. These CdSe/CdS core/shell nanoplatelets are atomically-flat, few monolayers-thick nanostructures consisting of a thin crystalline slabs of the CdSe core sandwiched between two CdS shell layers. As the thickness of the nanoplatelets is much smaller than the exciton Bohr radius, while the lateral dimensions are much larger, they can be considered as an atomic system with high spatial confinement in a single dimension. Similar to CdSe/CdS quantum dots, CdSe/CdS nanoplatelets′ emission can cover almost all the visible spectrum by changing their thickness [32]. Additionally, the core/shell structure is very helpful for improving the optical properties of this light source. Last but not least, their two dimensional structure holds such an interesting characteristic: when distributed on a planar surface, most of them stay by their faces stably, which will induce an orientation of the emitting dipole.

1.2 Thesis structure

This thesis is organized in 6 chapters. We firstly introduce in Chapter 1 the motivation, main objectives, experimental methods, samples, and organization of the thesis. The main subject of the thesis is to complete an effective and accurate polarimetric method to determine

the orientation of a nanoemitter′s dipole and its dimensionality from its emission.

The theoretical basis and the experimental setup for emission polarimetric determination are presented respectively in Chapter 2. Then, we discuss in the following chapters the techniques and the procedures involved in the polarimetric experiments: emission polarization characterization (Chapter 3) and emission pattern imaging (Chapter 4). In order to optimize the setup, all the optical elements have been numerically and experimentally analyzed. Details of systems′ organization and critical modifications are then studied properly with schematics of each setup improvement step. Lastly, we elaborate the experimental setup for emission polarimetric measurements and emission pattern imagings. We also address newly developed theories necessary for understanding and interpreting the experimental results.

Chapter 5 starts with literature reviews on the colloidal semiconductor nanoplatelets. We apply the experimental setup developed and described in Chapter 3 and Chapter 4 for the polarimetric measurements of the light emission by individual CdSe/CdS nanoplatelets. Each nanoplatelet is imaged by a microscope, then its emission is measured by avalanche photodiodes whereas its angular emission pattern is directly captured. This combination of the two experimental methods enables us to determine the dipolar dimensionality and orientation with high accuracy. In the final sections of Chapter 5, a geometry-dependent study of the emission polarization and emission pattern is investigated, confirming the physical interpretations made in the previous sections.

Our conclusions are given in the last chapter.

Chapter 2

Microscopy setup for polarimetric determination measurements

Introduction

Fluorescence microscopy has been widely used in many areas of scientific research to observe and characterize microscopic sized specimens that are not observable with the unaided human eye. However, it is always desirable to have the possibility to conduct more sensitive analysis on the optical properties of single particles. A confocal strategy has its advantages in this area.

The idea of confocal microscopy was first created by Marvin Minsky in the early 1950s [33]. By utilizing a pinhole in front of the detector to select a single plane of the sample, it would ideally minimize the unwanted effects from the surroundings and the fluorescing sample carriers (glass/metal plates). Thus the strategy can potentially improve the signal to noise ratio in single emission studies. The use of the laser together with a high numerical aperture objective enabled us to illuminate a very small spot on the specimen and detect the light coming only from the illuminated spot. The availability of sensitive single photon detectors, for example, an avalanche photodiode, helped confocal microscopy to detect very weak light emission. Therefore, fluorescence confocal microscopy is now being employed in many optical researchs, especially the single-molecule fields [34–37].

The efficient coupling of a single photoluminescent nanoemitter to photonic or plasmonic structures plays a very important role in the function of the next generation devices, such as nanoantennas [16, 38, 39]. It has been long suggested that the orientation of the emitting

dipole has a strong effect on its coupling to the local environment, especially in photonic studies [16, 38, 40–42]. Numerous theoretical and experimental studies have been conducted in order to deterministically couple nanoemitters to photonic nanostructures. Several researching groups have already published on spatial positioning of an emitter [16,43,44] and spectral tuning of its emission to cavity modes [45, 46]. However, up to now the deterministic control of the orientation of an emitting dipole within a nanostructure is still a challenging task. Determining the dipolar orientation of the photoluminescent emitter is a requirement in plasmonics and dielectric cavities since, for example, in the case of surface plasmon polariton (SPP) excitation, the dipole has to be perpendicular to the surface. Thanks to the orientation determination, we could select well oriented dipoles to achieve the good plasmonic/photonic devices.

A method has been developed in our group to determine the three-dimensional orientation of an emitting dipole by analysing its emission′s polarization together with its emission pattern. We also provide an analytical model that can be used to interpret the data in a wide range of realistic experimental conditions, including a very typical case in plasmonics when the nanoemitters lie on a gold film, a situation for which the more popular defocused imaging could not provide reliable information for some kinds of emitters such as those described by two dimensional dipoles.

In this chapter, a brief theoretical review will be given on the polarimetric determination of an emitting dipole. We first introduce the dimensionality of a single emitting dipole. After the effects of the dipolar orientation and the sample environment on the polarization state of the collected emission are explained, we present the theoretical basis to interprete the polarimetric results in order to extract the information about the dipolar orientation. We also consider the systemetic errors resulting from the polarization effects of the realistic eperimental setup. Finally, the experimental microscopy setup is designed and constructed to accomplish the mentioned subject and newly studied theories needed in order to characterize the polarization effects of the setup are discussed.

2.1 Determining the orientation of an emitting dipole

The determination of an emitting dipole can be accomplished by several different methods. Some authors have considered the defocused [47, 48] or aberrated [49] fluorescence image of the emitters. Although these techniques are quite conveniently applied in the experiments, their precision requires high quality emitters and highly sensitive CCD camera. Moreover, it could only give reliable informations in the case when the emission diagram of the emitter dipole is

strongly dependent on its orientation.

Other methods including ours are based on the polarization of the emission [50–52]. We will start by summarizing the important definitions employed in building our model for determining the orientation of an emitting dipole by analyzing the detected emission polarization. Then the influence of the imperfect polarizing components of the realistic measurement setup is discussed.

2.1.1 The dimensionality of a single emitting dipole

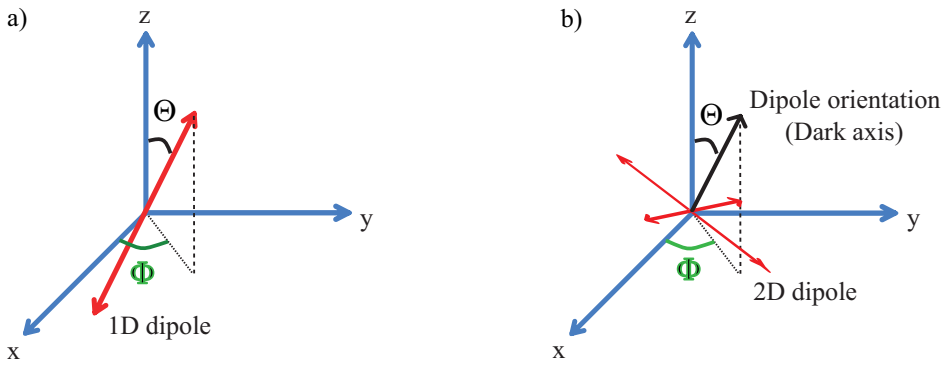

FIGURE 2.1: Schematic of a dipole orientation with in-plane angle Φ *with respect to x axis of the setup and off-axis angle* Θ *with respect to z axis of the setup for (a) one dimensional dipole and (b) two dimensional dipole.*

One of the most important properties for many recent fields of studies especially in plasmonics or photonics is the photoluminescence of a single nanoemitter coupled to a nanostructure which mainly depends on the orientation of its emitting dipole with respect to the structure. The determination of the orientation of the emitting dipole therefore becomes very crucial to further advance the technology for more efficient coupling.

The photoluminescence from a single nanoemitter could be modeled as an electric dipole since the charges oscillate in certain directions. The simplest case is a linear orientation, corresponding to the case when the charges oscillate along a well defined axis. It is also called an one dimensional (1D) dipole [41, 53]. As an example, the dot-in-rod (spherical core with an elongated rod-like shell) nanocrystal is experimentally proven to be an one dimensional emitting dipole [54–57].

However, in many other cases, the emission originates from a twofold degenerated emitting energy level [50, 58, 59]. It could be described as an incoherent sum of two orthogonal linear dipoles, referring to the charge oscillations in a specific plane. Therefore, it is named a two dimensional (2D) dipole. For instance, some molecules such as benzene have orthogonal

emitting dipoles thanks to their group symmetry [60]. That behavior has also been reported for single nitrogen-vacancy centers in nanodiamond [61], or colloidal CdSe/ZnS quantum dots at both low [50] and room temperature [58, 59]. The degeneration of the energy structure is believed to relate to the spin of the charges, and the polarization are known to be $\sigma+$ and $\sigma-$. In the case of room temperature, at the excitation energy above the emitting transition energy, these two transitions are incoherent. Therefore, we could describe the emitting dipole as a sum of two orthogonal linear dipoles. The knowledge of the dipolar one or two dimensionality of a nanoemitter is thus important to provide information on the energy level structure of the emitters, which is crucial for determining the orientation of the emitting dipole.

Figure 2.1 illustrates the one and two dimensional dipoles with their dipolar orientation respectively. The orientation of an one dimensional dipole corresponds to the orientation of its dipolar axis as shown in Figure 2.1(a); whereas in the case of a two dimensional dipole, the dipolar orientation is defined along its dark axis, a vector perpendicular to the plane formed by two component linear dipoles (Figure 2.1(b)). The orientation of the dipole is described by the polar angle Θ (with respect to z axis of the reference system where $\Theta = 0$ for the case that the dipole is normal to the sample plane) and the azimuthal angle Φ (with respect to x axis of the reference system) in the spherical coordinates.

2.1.2 Role of the dipolar orientation on the detected emission polarization

We consider a single photoluminescent emitter in homogenous media. It is well known that the orientation of the emitting dipole is directly encoded in the angular distribution of the emitted light which is so called the emission pattern.

In free space, the emission pattern of a linear dipole is characterized by a $\sin^2\theta$ distribution where θ is the angle between the dipolar axis and the direction of propagation/observation. For one dimensional dipole, in an homogeneous dielectric infinite environment, the emission is symmetrically distributed about the axis of the dipole, as shown in Figure 2.2(a). It should be noted that there is no radiation along this dipolar axis (referring to $\theta = 0$). $\vec{e_r}$ is a unit vector in the direction of propagation/observation, which is described as (θ, ϕ) in the spherical coordinates centered by the dipolar axis. The created electric field $\vec{E}$ is along the component vector $\vec{e_\theta}$, which is perpendicular to the direction of propagation.

Figure 2.2(b) illustrates two extreme cases of a vertical and horizontal dipole, respectively. Since the electric field collected by the objective can be in any directions within the limit

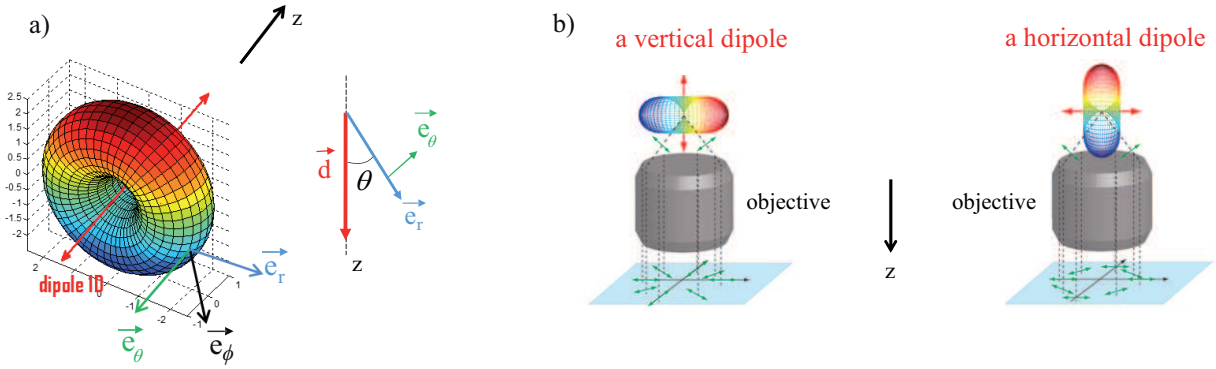

FIGURE 2.2: (a) Emission diagrams of one dimensional dipole in homogeneous media with θ is the angle between the reference axis z and the direction of propagation/observation $\vec{e_r}$ (in blue), referring to the electrical field aligned along the unit vector $\vec{e_\theta}$ (in green). (b) Schematics of 2 extreme cases when the dipole is vertical and horizontal, respectively. The collected emission by the objective in the case of the vertical dipole is not polarized whereas it reachs maximum for the horizontal case.

imposed by its numerical aperture for an emitting dipole oriented along z axis (a vertical one), the total detected light is not polarized. On the other hand, if the dipole is perpendicular to the z axis, the direction of the collected vectors $\vec{e_\theta}$ just varies slightly in the considering zone of the emission diagram. Then the electrical field will be mainly along a certain direction, resulting in a maximum polarization. Therefore, by analyzing the polarization of the detected emission, we could determine the orientation of the emitting dipole.

2.1.3 Determination of the dipolar orientation by polarimetric measurements

Theoretical modelling of our study can be derived by considering an individual emitter in a three dimensional coordinate system. The z axis is along the direction of propagation whereas the x and y axis correspond to the proper axes of the microscope as illustrated in Figure 2.3(b). These calculations are developed in the thesis of Clotilde Lethiec [27,52,62], based on the works done by Lukosz [63,64]. Figure 2.3(a) describes in the xyz reference coordinates, the emitting dipole $\vec{d}$ which is oriented with an out-plane angle Θ relative to the z axis (the polar angle) and an in-plane Φ relative to the x axis (the azimuthal angle) while the propagation vector is defined by a polar angle θ and an azimuthal angle ϕ. The setup is presented in Figure 2.3(b), consisting of a 450 nm excitation laser. The emission of the dipole is collected by a microscope′s objective and then analyzed by a linear polarizer which is rotated around the z reference axis with an in-plane rotation angle β.

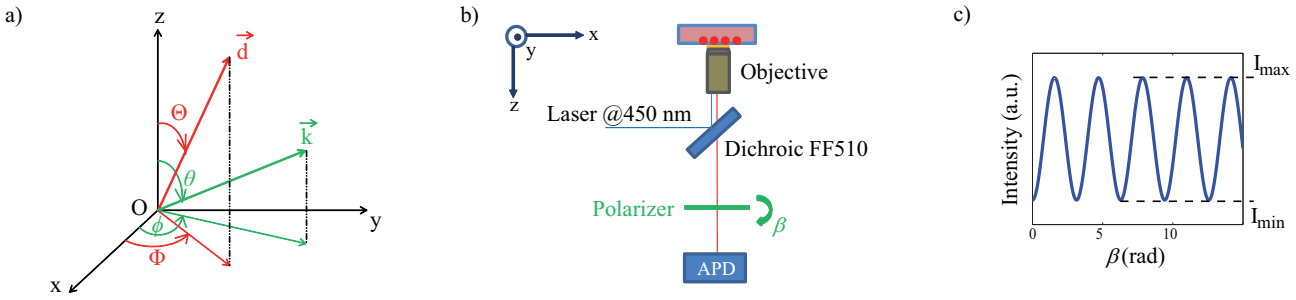

FIGURE 2.3: (a) Schematic of an emitting dipole $\vec{d}$ with in-plane angle Φ and out-plane angle Θ and the propagation vector $\vec{k}$ with in-plane angle ϕ and out-plane angle θ. (b) Schematic of the simulated measurement: the emitter is excited by a 450 nm laser and its emission is collected by an objective; while the polarizer is turned around the z axis (the propagation direction) with an angle of β, the intensity data are recored by an APD. (c) An example of the obtained polarimetric curve: The dependence of detected intensity as a function of the polarization analysis angle β.

While the polarizer is continuously rotated with an angle of β, the photoluminescence intensity corresponding to different polarization directions is measured by an avalanche photodiode (APD). The recorded intensity oscillates between a minimum value (I_{min}) and a maximum value (I_{max}), as observed in Figure 2.3(c).

The normalized curve obtaind by the transmission APD is then fitted by the function [52, 62]:

$$I(\beta) = I_{min} + (I_{max} - I_{min})\cos^2(\Phi' - \beta) \tag{2.1}$$

In the case of an one dimensional dipole, $\Phi' = \Phi$, the detected intensity is maximum when the axis of the polarizer is aligned with the axis of the dipole in the sample′s plane ($\beta = \Phi$). For a two dimensional dipole, as $\Phi' = \Phi + \pi/2$, when β is equal to Φ the detected intensity is minimum, implying that the dipole′s plane is perpendicular to the axis of the polarizer. Therefore, we could estimate the azimuthal angle Φ of the emitting dipole from the phase of the detected polarimetric curve.

The degree of the linear polarization is defined as :

$$\delta(\Theta) = \frac{I_{max} - I_{min}}{I_{max} + I_{min}} \tag{2.2}$$

with $\delta = 1$ for a completely linearly polarized light.

When the dipole is in the vicinity of an optical interface, its emission polarization is modified [64]. Therefore, the degree of polarization measured from the experiment depends on the dimensionality of the dipole, but also on other parameters: the polar angle Θ (between the

dipolar orientation and the optical axis of the objective), the objective's numerical aperture NA, and the experimental interface configuration between the sample and the objective, as well.

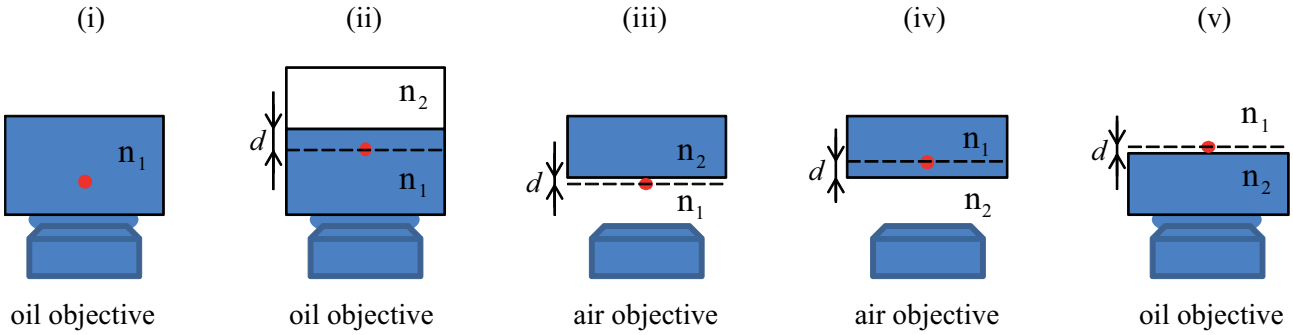

FIGURE 2.4: Schematic of the five cases corresponding to different experimental configurations between the sample and the objective, numbered from (i) to (v) with d being the distance from an emitter to the medium interface, n_1 denoting the index of the medium containing the emitter, and n_2 for the index of the other medium.

There are five relevant experimental single interface sample-objective configurations which are possibly performed in the microscope, as presented in Figure 2.4. For all situations, we use n_1 for the index of the medium containing the emitter and n_2 for the index of the other medium. Therefore, if the objective is an oil immersion one with the refractive index of 1.5, we consider three following cases:

- (i) emitters are in an homogeneous medium of n_1
- (ii) $n_1 = 1.5$ and $n_1 > n_2$: emitters are deposited on a planar substrate of index n_1 and covered by a polymer layer with a thickness d of the same index while the upper medium has the index n_2
- (v) $n_2 = 1.5$ and $n_2 > n_1$: emitters are in the medium of index n_1 (as deposited at a distance d (with d tending towards 0) from a planar surface without the covering layer), observed by an oil objective of index n_2

Similarly, in the case of an air objective with the index of 1, there are 2 different cases:

- (iii) $n_1 = 1$ and $n_2 > n_1$: emitters are at a distance d (with d tending towards 0) from a substrate with an index n_2 without any protecting layer
- (iv) $n_2 = 1$ and $n_1 > n_2$: emitters are on a planar substrate with a polymer protecting layer of index n_1

For one dimensional dipole, we have [52, 62] :

$$\delta_{1D}(\Theta) = \frac{Csin^2(\Theta)}{(2A - 2B + C)sin^2(\Theta) + 2B} \tag{2.3}$$

and in the case of two dimensional dipole :

$$\delta_{2D}(\Theta) = \frac{Csin^2(\Theta)}{(2B - 2A - C)sin^2(\Theta) + 4A + 2C} \tag{2.4}$$

where A, B, C could be calculated from the numerical aperture of the objective and the refractive index, depending on the medium in which the emitter is embedded and the interface configuration between the sample and the objective. Therefore, from the detected intensity $I(\beta)$, knowing the dimensionality of the dipole, the polar angle Θ could be extracted.

For example, if we consider the case of an emitter in a semi-infinite dielectric medium of index 1.5, at 50 nm from a semi-infinite medium of gold when its emission is collected by an oil immersion objective with the numerical aperture of 1.4 (configuration case (ii)), the relationship between the degree of polarization δ and the polar angle Θ for each dipolar dimensionality is a bijective function, as illustrated in Figure 2.5. It means the knowledge of δ (calculated from the detected intensity) would give information on the dipolar orientation Θ. In the case when the dipolar orientation along the z direction ($\Theta = 0$), refer to a vertical one dimensional dipole or a horizontal two dimensional dipole, the emission is fully unpolarized ($\delta = 0$), as expected due to the symmetry of the system. When the polar angle Θ is larger, the degree of polarization δ increases, refering to more polarized emission. Then in the case of $\Theta = 90^o$, δ reachs its maximum of $\frac{C}{2A + C}$ for an one dimensional dipole and $\frac{C}{2A + 2B + C}$ for a two dimensional one, which is theoretically given for a certain situation.

Moreover, for an one dimensional dipole, in the experimental configuration described in Figure 2.5(a), if the dipole is orientated at $\Theta = 90^o$, the degree of polarization δ can reach nearly 100% while δ of the emission from a two dimensional dipole maximizes around 80%. The emission from two incoherent dipoles is always less polarized than the one from a single linear dipole for the same dipolar orientation. For both cases, since we collect the signals from each the possible directions within the objective′s numerical aperture, the maximum polarization achievable for the whole beam can never reach 100%.

In conclusion, thanks to the polarimetric measurements, if the dipolar dimensionality is known, we could extract the polar angle Θ and the azimuthal angle Φ of the emitting dipole from the detected intensity curves, leading to the determination of the dipolar orientation.

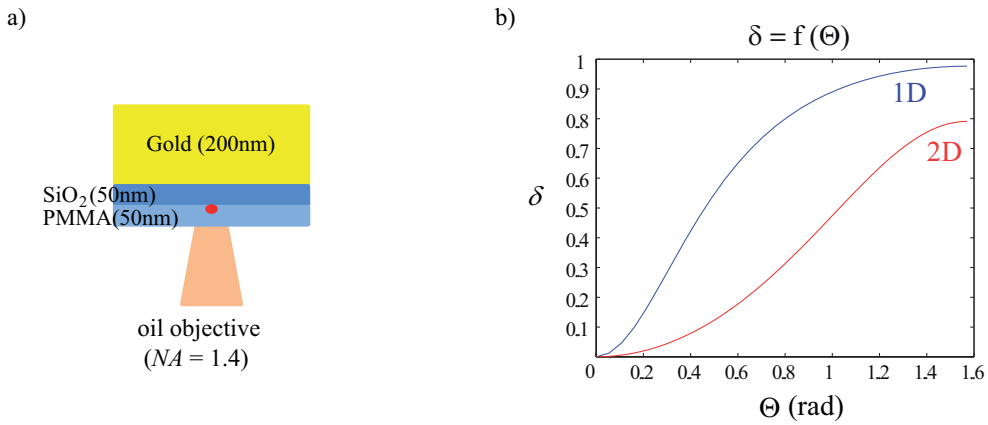

FIGURE 2.5: (a) Schematic of the experimental configuration corresponding to interface case (ii): an individual emitter sandwiched between a 50 nm SiO_2 covered gold substrate and a 50 nm PMMA layer, observed by an oil objective with $NA = 1.4$. (b) The corresponding calculated relation between the degree of polarisation δ and the dipolar orientation (the polar angle Θ).

2.1.4 Effect of a phase retardation induced by the setup′s optical elements

Our above theoretical modelling has been developed under ideal conditions without considering any additional polarization effects which may be introduced by the optical elements of the measurement setup. However, the non-ideal nature of a realistic experimental setup definitely affects its accuracy for characterizing the polarization state of the transmitted light. For instance, due to the birefringence of the setup, the outgoing polarization has been shifted by a phase retardation ψ compared to the incident one.

As discussed before in Figure 2.3(b), in the reference coordinates with z axis along the direction of propagation whereas the x and y axes correspond to the proper axes of the microscope, the polarization orientation of an emitting dipole is determined by the azimuthal angle Φ with respect to x axis and the polar angle Θ with respect to z axis. When the polarizer is rotated in the $x-y$ plane by an angle β, our model (which does not consider any polarizing effect induced by optical elements) gives a value of the 'so-called' actual azimuthal angle $\Phi = \beta$. Therefore, the measured value Φ_{mes} which is extracted from the experimental data obtained by the realistic measurement setup having a phase retardation of ψ will be different from the actual value Φ which corresponds to the dipolar orientation. We can prove (see Appendix) that the actual azimuthal angle Φ of the dipole is related to the measured value Φ_{mes} by:

$$tan2\Phi = \frac{tan2\Phi_{mes}}{cos\psi} \tag{2.5}$$

It is mentioned above that there is a theoretical relationship between the degree of polarization δ and the dipole′s polar angle Θ. Therefore, we could extract the polar angle Θ from δ, as described in Figure 2.5(b). We also define δ_{mes} as the degree of polarization measured from the experiments by the realistic setup with a retardation of ψ. It is related to $\delta(\Theta)$, the actual degree of polarization of the emission from the dipole (the actual value we would obtain with a setup without any retardation effect), by the following equation :

$$\delta_{mes} = \delta(\Theta)\frac{cos2\Phi}{cos2\Phi_{mes}} \tag{2.6}$$

We define a factor $M = \dfrac{cos2\Phi}{cos2\Phi_{mes}}$ as a correction factor corresponding to the ratio between the measured values and the actual values. When $M = 1$, the measured value is exactly the actual value describing the polarization state of the dipole.

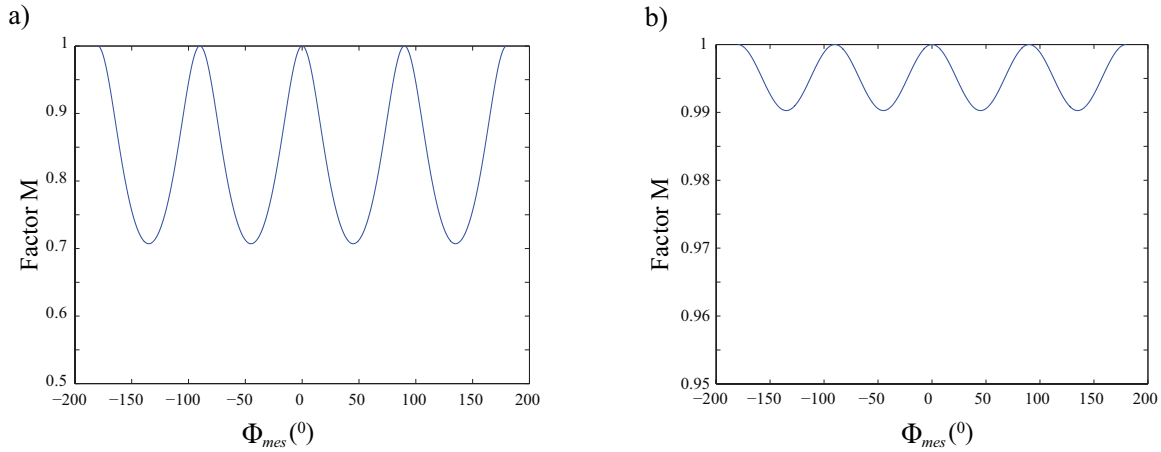

FIGURE 2.6: The dependence of the factor M on the measured azimuthal angle Φ_{mes} when the phase retardation ψ is (a) 55^o and (b) 8^o.

Figure 2.6(a) shows the influence of the setup′s phase retardation ψ on the factor M. When the phase shift between two orthogonal components of the beam transmitted through the setup is $\psi = 55^o$, the factor M evolves between 1 and 0.7. M gets maximum ($M = 1$) when the measured azimuthal angle $\Phi_{mes} = r_1\, 90^o$ with $r_1 \in \mathbb{Z}$, corresponding to the x or y proper polarization direction. It means that the retardation induced by the birefringent elements of the setup has no effect on the resulting phase determination. In this case, $\Phi_{mes} = \Phi$ and $\delta_{mes} = \delta$. Moreover, M reachs its minimum at 0.7 when $\Phi_{mes} = 45^o + r_1\, 90^o$, referring the analyzer′s axis is along the 45^o linear polarization directions. For this dipolar orientation Φ_{mes}, the phase retardation introduced by the setup has the maximum impact on the measured data.

It should be noted that when the setup has no dephasing ($\psi = 0$), $\Phi_{mes} = \Phi$ and $\delta_{mes} = \delta$.

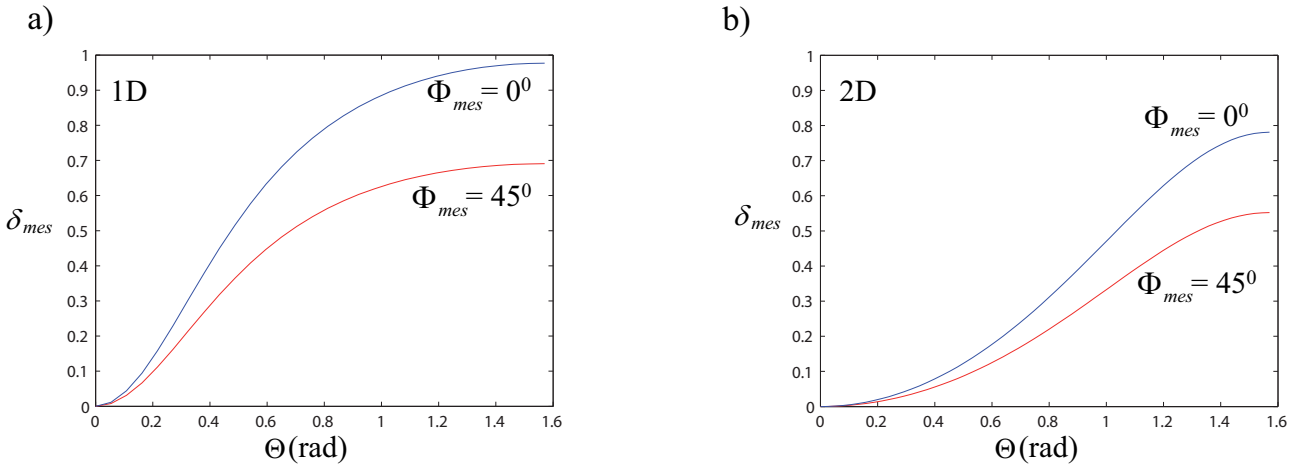

FIGURE 2.7: The values of δ_{mes} as a function of the angle Θ for an one dimensional dipole (a) or a two dimensional dipole (b), calculated in the reflection configuration (the emitter is at a distance of 50 nm to the gold-PMMA interface, oil objective with $NA = 1.4$) in two extreme cases when the setup introduces a phase retardation of $\psi = 55^o$.

We then plotted in Figure 2.7 the correspondence between the measured degree of polarization δ_{mes} measured by the setup with $\psi = 55^o$ and the polar angle Θ of the emitting dipole in two extreme cases of the $\Phi_{mes} = 45^o$ (factor M is at its minimum of 0.7, red lines) and $\Phi_{mes} = 0^o$ (factor M reaches its maximum $M = 1$, blue lines) for an one dimensional and a two dimensional dipole. When $\Phi_{mes} = 0^o$, the measured degree of polarization δ_{mes} is equal to the actual value δ which is obtained when there is no setup′s retardation ($M = 1$). This is not a surprise since the state of polarization is not influenced by any retardation effect as long as the linear direction of the dipole is along the x or y proper axis.

On the contrary, when $\Phi_{mes} = 45^o$, the effect of the setup′s retardation is maximum, leading to the biggest difference between the measured value δ_{mes} and the actual value δ (without considering the phase retardation induced by the setup). The change in polarization state caused by the phase retardation becomes more important when the dipolar orientation is close to the sample′s plane ($\Theta = \pi/2$). Therefore, in order to avoid as much as possible post-correction of the data (recalculation of $\delta(\Theta)$ and Φ from δ_{mes} and Φ_{mes}), the phase retardation of the setup ψ has to be characterized and minimized.

2.2 Polarimetric determination measurement

This section addresses our experimental design for measuring the polarization of the emission from an individual emitter. Firstly, we construct the initial proposed microscopy setup

based on the simulated experimental schematic as presented in Figure 2.3(b). Since it is proved in the subsection 2.1.4 that the polarization effect of the setup plays an important role in interpreting the polarimetric data, we develop the theoretical and practical procedures to characterize our measurement setup in term of polarization.

2.2.1 Basic experimental setup for measuring emission polarization

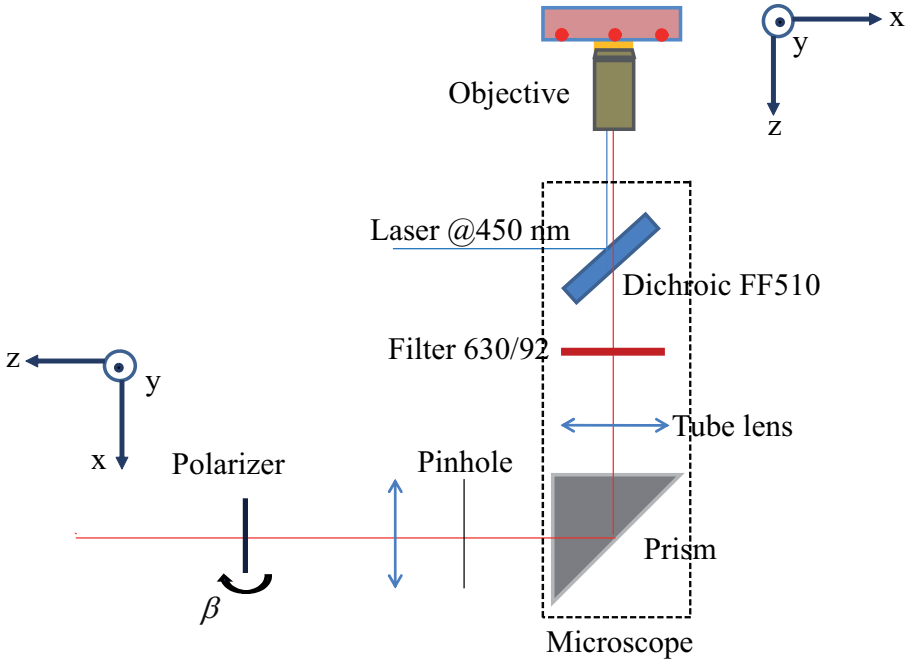

FIGURE 2.8: Schematic configuration of the proposed setup for emission polarization measurement. An individual emitter is excited and its emission is collected by a microscope. Polarization measurement is performed by rotating a linear polarizing analyzer made of a halfwave plate ($\lambda/2$) and a polarizing beamsplitter cube (PBS). Noted that the z axis is always oriented in the direction of propagation and the vectors normal to the dichroic and prism interfaces in the $x-z$ plane are fixed at 45^o with respect to the z direction thanks to the microscope. The mirror and the cube are also aligned to have their normal vectors in their planes of incidence at 45^o to the z direction.

We propose an experimental setup in order to realize the emission polarization measurement, schematized in Figure 2.8. The blue laser (the wavelength of 450 nm, pulse mode with a duration of 80 ps) is injected into a standard inverted microscope (Olympus IX71). After reflecting on a dichroic beamsplitter, the light is focused by a 100x objective. Since the typical wavelength of the emission for the emitters concerned in this thesis lies from 630 to 640 nm, the dichroic FF510-Di01 (@Semrock) is chosen to efficiently separate the laser and the emission.

The sample holder is mounted on a nanometer precision piezoelectric scanner that trans-

lates the sample in the focal plane (x, y). The emitters are excited by the laser, then the photoluminescent light is collected by the same objective. A bandpass filter with center wavelength at 630 nm and the bandwidth of 92 nm (@Semrock) which rejects the laser by 7 orders of magnitude is inserted right after the dichroic beamsplitter in order to remove most of the remaining laser beam.

After reflecting on the prism inside the microscope, the emitting light is focused on a 150 μm pinhole (placed at the image plane of the microscope) in order to spatially filter the background noise. It is then recollimated by a lens, passing through a halfwave plate ($\lambda/2$), and finally separated into 2 parts with orthogonal polarization directions by a polarizing beam splitter cube (PBS). Each part is focused and captured on a respective single photo counting avalanche photodiode (APD).

The rotating halfwave plate together with the polarizing beam splitter cube actually acts like a linear polarizer whose direction could be controlled. When the halfwave plate is turned by an angle of ϖ, it corresponds to turning the polarizer by an angle $\beta = 2\varpi$. The electric field E of the linear polarized light is thus rotated by an angle which is two times of the angle between its polarization direction and the fast axis of the halfwave plate.

Using a rotable halfwave plate and a beam splitter cube instead of a linear polarizer will enable us to obtain two different detection parts to perform the antibunching measurement as well. Moreover, it also offers us the possibility to normalize the obtained intensity. We will analyze the data recorded by the transmssion APD (APD 1) since the polarizing beamsplitter cube transmits only horizontal component of the light. These data are normalized by the total intensity collected by both photodiode $I_{norm_1}(\varpi) = \dfrac{I_1(\varpi)}{I_1(\varpi) + I_2(\varpi)}$, so we could reduce the noises due to the fluctuations of the total intensity (blinking). The polarization measurement of the photoluminescence from the sample will be accomplished by analyzing the normalized intensity $I_{norm_1}(\varpi)$ when turning the halfwave plate.

2.2.2 Representation of polarization by Jones matrix formalism

Although light is composed of oscillating electric and magnetic fields, by convention, the polarization of light refers to the polarization of the electric field. An optical element can modify the polarization state of the transmitted light by changing the amplitude or the phase of the components of the electric vector $\vec{E}$ [65, 66].

There are two types of polarization materials [67, 68]. In both types, we define two main

axes so that when a linearly polarized light propagates along one of these axes, its polarization state is not modified. The first type is the diattenuating element, so called a diattenuator of which the intensity transmittance of the exiting beam is different for both proper directions, therefore, the output′s intensity depends on the polarization orientation of an incident beam [69]. The other one is the dephasing element or also called a retarder which introduces a differential phase shift between the two polarization components of a light wave, thereby altering its polarization state [70].

In our proposed experimental setup, there are a dichroic beamsplitter (a diattenuator and a dephaser) and a prism (a retarder) which may introduce some polarization effects (amplitude or phase change) to the transmitted light. Therefore, it is necessary to characterize the setup in term of the polarization of transmission. We will use the Jones matrix formalism, a helpful means to mathematically decribe the light′s polarization state.

Similar to the Stokes polarization parameters and the Mueller matrix formalism, Jones formalism is a complete and quantitative technique not only for representing the light's polarization state but for calculating the effects of optical elements that modify polarization of the incident light, as well. It was developed by R. Clark Jones in the 1940s [65, 66].

In Jones formalism, the polarization state of light is given by a 2×1 Jones vector and the linear operation of a polarization element is described using a 2×2 Jones matrix. The effect of a system consisting of many elements will be represented by the product of the Jones matrix for each element [71–78].

Moreover, the Jones matrix formalism is applicable to the field which includes the phase and the amplitude. As it quantifies the phase change of the electric field components, the Jones formalism can be used to analyze the interference. On the other hand, the Stokes parameters/Mueller formalism determine the beam′s intensity. In the case when the beam rapidly and randomly changes in phase (an incoherent beam), the physic is usually described by the intensity, therefore, the Stokes parameters and Mueller formalism are chosen. For coherent beams which require the information of the phase relationship, the Jones formalism is more suitable.

2.2.2.1 The Jones vector

Although light is composed of oscillating electric and magnetic fields, the traditional approach to study the polarized light is considering the polarization of the electric field. Therefore, R. C. Jones started by representing light propagating along the z direction in terms of the x

and y components of the electric fields [71, 72]. The plane-wave components of the field can be written as:

$$E_x(z,t) = E_{0x}e^{i(\omega t - kz + \delta_x)} \tag{2.7}$$

$$E_y(z,t) = E_{0y}e^{i(\omega t - kz + \delta_y)} \tag{2.8}$$

where E_{0x}, δ_x and E_{0y}, δ_y denote the amplitudes and phases of the x and y components, respectively, of the electric vector $\boldsymbol{E}$ in the plane transverse to the propagation direction of the light.

These both components are oscillating in time with the same frequency but the amplitudes and phases may differ. Therefore, the propagator $\omega t - kz$ could be deduced, then the equations 2.7 and 2.8 are rewritten as:

$$E_x(z,t) = E_{0x}e^{i\delta_x} \tag{2.9}$$

$$E_y(z,t) = E_{0y}e^{i\delta_y} \tag{2.10}$$

These two equations 2.9 and 2.10 can be arranged in a column matrix $\boldsymbol{E}$ with

$$\boldsymbol{E} = \begin{pmatrix} E_x \\ E_y \end{pmatrix} = \begin{pmatrix} E_{0x}e^{i\delta_x} \\ E_{0y}e^{i\delta_y} \end{pmatrix} \tag{2.11}$$

This vector is known as a Jones vector [79]. Since the state of polarization is fully determined by the relative amplitudes and phases, the Jones vector is a complete description of a general elliptical polarization state of the light. In Equation 2.11, the maximum amplitudes E_{0x} and E_{0y} are real and positive numbers. The presence of the exponent with imaginary arguments causes E_x and E_y to be complex quantities.

However, it is not necessary to know the exact amplitudes and phases of the Jones vector components. Normalizing the Jones vectors helps simplify the calculus. For example, the following vectors involve different expressions but they are all describing the same polarization state.

$$\begin{pmatrix} E_{0x}e^{i\delta_x} \\ E_{0x}e^{i\delta_y} \end{pmatrix} \rightarrow \begin{pmatrix} e^{i\delta_x} \\ e^{i\delta_y} \end{pmatrix} \rightarrow \begin{pmatrix} 1 \\ e^{i(\delta_y - \delta_x)} \end{pmatrix} \tag{2.12}$$

It should be noted that a complex vector is said to be normalized when the product of the

vector with its complex conjugate yields a value of unity:

$$\boldsymbol{E^*}\,\boldsymbol{E} = {E_x}^*\,E_x + {E_y}^*\,E_y = E_{0x}^2 + E_{0y}^2 = E_0^2 = 1 \tag{2.13}$$

For example, the linear horizontally polarized light refers to $E_y = 0$ so Equation 2.11 becomes:

$$\boldsymbol{E_H} = \begin{pmatrix} E_{0x}e^{i\delta_x} \\ 0 \end{pmatrix} \tag{2.14}$$

From the normalization condition expressed in Equation 2.13, we have $E_{0x}^2 = 1$. Then, the part $e^{i\delta_x}$ can be suppressed as it is unimodular, the normalized Jones vector for linear horizontal polarization state could be represented as:

$$\boldsymbol{E_H} = \begin{pmatrix} 1 \\ 0 \end{pmatrix} \tag{2.15}$$

The normalized Jones vector describing the linear vertical polarization state is similarly found since $E_x = 0$ and $E_{0y}^2 = 1$ so that:

$$\boldsymbol{E_V} = \begin{pmatrix} 0 \\ 1 \end{pmatrix} \tag{2.16}$$

When the electric field is oriented at a 45° angle with respect to the basic states, we have $E_x = E_y$ so $2E_{0x}^2 = 1$ and normalized Jones vector for this state is written as:

$$\boldsymbol{E_{45^o}} = \frac{1}{\sqrt{2}} \begin{pmatrix} 1 \\ 1 \end{pmatrix} \tag{2.17}$$

Thus, in general, the normalized Jones vector representing a beam linearly polarized at an angle α from the horizontal axis is given by:

$$\boldsymbol{E_\alpha} = \begin{pmatrix} cos\alpha \\ sin\alpha \end{pmatrix} \tag{2.18}$$

Two other typical polarization states are right-circular and left-circular. In both cases, the

two x and y components have equal amplitudes but in the case of right circularly polarized light, the phase of the y component leads the x component by 90° ($\delta_y - \delta_x = 90°$) and conservely for left circularly polarized light ($\delta_y - \delta_x = -90°$). Therefore, we have the normalized representation for right circular polarization as:

$$\boldsymbol{E_{Rt}} = \frac{1}{\sqrt{2}} \begin{pmatrix} 1 \\ i \end{pmatrix} \tag{2.19}$$

and for left circular polarization:

$$\boldsymbol{E_{Lt}} = \frac{1}{\sqrt{2}} \begin{pmatrix} 1 \\ -i \end{pmatrix} \tag{2.20}$$

2.2.2.2 The Jones matrix

Jones formalism describes the change of light′s polarization state after passing through a polarization element. Let us consider a beam of light with a given polarization state described by the Jones vector $\boldsymbol{E}$, as in Equation 2.11, incident on an optical element. The light will interact with the element, then the new polarization state of the light emerging from the element will be presented as:

$$\boldsymbol{E'} = \begin{pmatrix} E'_x \\ E'_y \end{pmatrix} \tag{2.21}$$

Assuming that the components of the output light are linearly related to ones of the input, we have:

$$E'_x = a\,E_x + b\,E_y \tag{2.22}$$

$$E'_y = c\,E_x + d\,E_y \tag{2.23}$$

where a, b, c, d are the transforming factors.

These two equations 2.22 and 2.23 can be rewritten in matrix form as:

$$\boldsymbol{E'} = \boldsymbol{J}\boldsymbol{E} \tag{2.24}$$

where

$$\boldsymbol{J} = \begin{pmatrix} a & b \\ c & d \end{pmatrix} \tag{2.25}$$

It is called the Jones matrix of an optical element [79]. Any polarization element can be

represented by its corresponding Jones matrix and vice versa.

It is possible to get a single 2×2 Jones matrix representing the whole system of many elements by matrix multiplication. If light passes through cascaded optical elements, for example, M1 then M2, we will multiply each element′s Jones matrix in the reversed order to yield a total Jones matrix of the system:

$$\boldsymbol{J_{tot}} = \boldsymbol{J_{M2}}\,\boldsymbol{J_{M1}} \tag{2.26}$$

The effect of an optical element on the polarization could be analyzed in term of either the amplitudes or the relative phases separately. The element modifying the amplitudes is called a diattenuator and the element changing the relative phase is called a retarder.

The Jones matrix of a diattenuator is given by:

$$\boldsymbol{J}_D = \begin{pmatrix} t_s & 0 \\ 0 & t_p \end{pmatrix} \tag{2.27}$$

where $T_s = {t_s}^2$ and $T_p = {t_p}^2$ is the intensity transmittance of the s and p component of the incident light. The s and p designations are related to the plane of incidence of the element. It is the plane defined by the propagation vector of the incoming light and the normal vector of the surface. The component of the electric field parallel to this plane is termed p-like while the component perpendicular to this plane is called s-like. Therefore, the polarized light with its electric field in the plane of incidence is known as p-polarized, while light whose electric field is normal to the plane of incidence is known as s-polarized [79].

The values of t_s and t_p parameter depend on the considered dichroic element and describe a wide range of situations. For example, when $t_s \neq 0$ and $t_p = 0$ or vice versa: the element only lets one component of the incident light transmit and completely absorbs the other component, implying that the investigated element behaves as a linear polarizer. For example, the following is the Jones matrices representing two typical ideal polarizers: for a polarizer with horizontal transmission axis

$$\begin{pmatrix} 1 & 0 \\ 0 & 0 \end{pmatrix} \tag{2.28}$$

for a polarizer with vertical transmission axis

$$\begin{pmatrix} 0 & 0 \\ 0 & 1 \end{pmatrix} \tag{2.29}$$

In the case of $t_s = t_p$, the incoming light has been absorbed in an isotropic way, so that there is no diattenuating effect.

Another element in the traditional formalism is a retarder which introduces a phase difference between two orthogonal components of the electric vector. Its corresponding Jones matrix can be written as:

$$\boldsymbol{J}_R = \begin{pmatrix} \mathrm{e}^{\frac{i\psi}{2}} & 0 \\ 0 & \mathrm{e}^{\frac{-i\psi}{2}} \end{pmatrix} \tag{2.30}$$

where ψ is the unknown phase retardation generated by the element between the two components E_s and E_p. It should be noted that the s and p designations is specifically related to the element itself. If the incident light is polarized along the proper axes of the element (s or p direction), we observe no retardation in phase. When the electric field is, instead, oriented at angle of 45° to the proper axes of the element, the field components have the same amplitude ($E_s = E_p$) and the element introduces the maximum retardation.

Therefore, when building the setup, it is necessary to fix the element in order to let the proper axes of the element correspond to the x and y reference axis of the whole setup. Especially, the dichroic and the mirror need to be put in order to have their normal vector in their incident planes oriented at 45° to the direction of propagation. Then we have the Jones matrix for the entire set-up with the phase retardation ψ and the intensity transmittance $T_x = {t_x}^2$ and $T_y = {t_y}^2$ along x and y reference axis respectively :

$$\boldsymbol{J}_1 = \begin{pmatrix} t_x \mathrm{e}^{\frac{i\psi}{2}} & 0 \\ 0 & t_y \mathrm{e}^{\frac{-i\psi}{2}} \end{pmatrix} \tag{2.31}$$

.

2.2.2.3 The Jones matrices of rotating elements

The proper axes of a polarization element are not always oriented along the x and y reference dimensions. In order to take into account any angular position the element can assume during the experiment, we need the rotation transformation :

$$\boldsymbol{J}_2 = \boldsymbol{J}(-\beta)\, \boldsymbol{J}\, \boldsymbol{J}(\beta) \tag{2.32}$$

where $\boldsymbol{J}(\beta)$ is the rotation matrix :

$$\boldsymbol{J}(\beta) = \begin{pmatrix} cos\beta & sin\beta \\ -sin\beta & cos\beta \end{pmatrix} \tag{2.33}$$

with β denoting the angle between the the proper axis of the element and the x axis of the setup.

The Jones metrix for an ideal polarizer oriented along the x axis of the setup $\boldsymbol{J}$ with the intensity transmittance $T_{Pol} = t_{Pol}^2$ is given by $\boldsymbol{J_P} = t_{Pol} \begin{pmatrix} 1 & 0 \\ 0 & 0 \end{pmatrix}$.

Carrying out the matrix multiplication in Equation 2.32, we find that the Jones matrix representing a linear polarizer rotated by β and its intensity transmittance T_{Pol} is shown to be :

$$\boldsymbol{J}_2(\beta) = \boldsymbol{J}(-\beta)\,\boldsymbol{J_P}\,\boldsymbol{J}(\beta) = t_{Pol} \begin{pmatrix} cos^2\beta & sin\beta cos\beta \\ sin\beta cos\beta & sin^2\beta \end{pmatrix} \tag{2.34}$$

The Jones matrix for a retarder has been defined in Equation 2.30, we will rewrite here with φ is the retardation between the field components :

$$\boldsymbol{J}_R(\varphi) = \begin{pmatrix} \mathrm{e}^{\frac{i\varphi}{2}} & 0 \\ 0 & \mathrm{e}^{\frac{-i\varphi}{2}} \end{pmatrix} \tag{2.35}$$

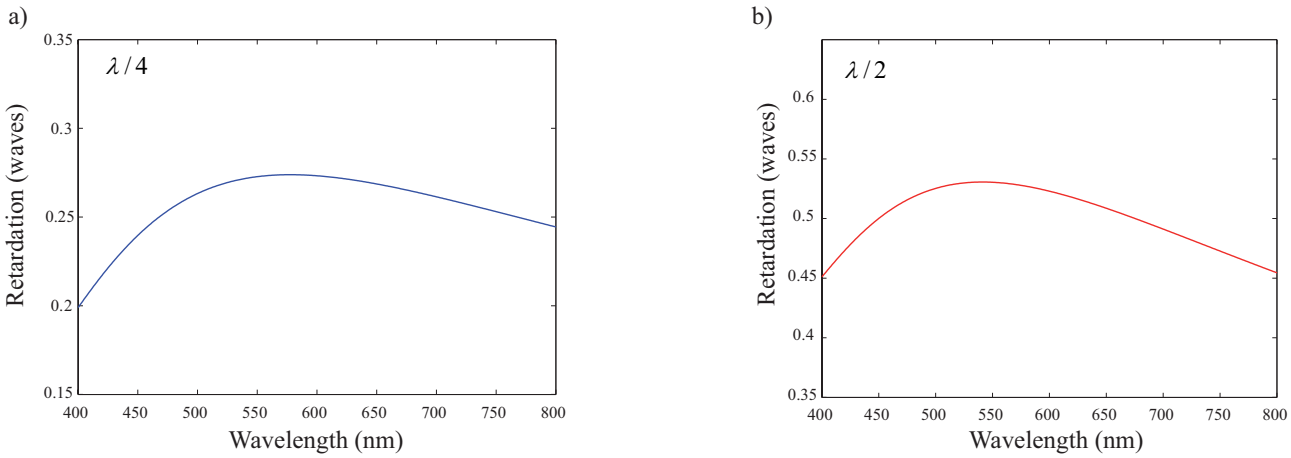

FIGURE 2.9: The retardation of a waveplate as a function of the wavelength, taken from the specification data of Thorlab homepage for (a) a quarterwave plate AQWP05M-600 and (b) a halfwave plate AHWP05M-600 [80].

Figure 2.9 presents the retardation of manufactured waveplates: a quarterwave plate AQWP05M-600 and a halfwave plate AHWP05M-600 [80]. These plates are broadband ones so that for a large spectral range ($400nm < \lambda < 800nm$), their retardation remains respectively close to $\frac{\lambda}{4}$ and $\frac{\lambda}{2}$. To achieve these specifications, the manufacturer has to compensate the dispersion of the materials. As the compensation is not perfect, the retardation is close to the target value but not strictly equal to it ($\pm 0.05\lambda$). In the followings, we will discuss these non-ideal quarterwave plate and halfwave plate.

We assume that at the considered emission's wavelength the retardation of the quarterwave plate is $\varphi_{\lambda/4} = 2\varphi'_{\lambda/4} = \frac{\pi}{2} + 2\vartheta$. With the rotation transformation by Equation 2.32, we find the Jones matrix for a non-ideal quarterwave retarder rotated by ν from the x reference axis is :

$$\begin{aligned} \boldsymbol{J}_{\lambda/4}(\varphi_{\lambda/4}, \nu) &= \boldsymbol{J}(-\nu)\, \boldsymbol{J}_R(\varphi_{\lambda/4})\, \boldsymbol{J}(\nu) \\ &= \begin{pmatrix} cos\varphi'_{\lambda/4} + i\, sin\varphi'_{\lambda/4}\, cos2\nu & i\, sin\varphi'_{\lambda/4}\, sin2\nu \\ i\, sin\varphi'_{\lambda/4}\, sin2\nu & cos\varphi'_{\lambda/4} - i\, sin\varphi'_{\lambda/4}\, cos2\nu \end{pmatrix} \end{aligned} \tag{2.36}$$

Similarly, we reduce the Jones matrix of a non-ideal halfwave plate rotated by ϖ from the x axis with the retardation $\varphi_{\lambda/2} = 2\varphi'_{\lambda/2} = \pi + 2\gamma$ at the wavelength of our emission by multiplying the Jones matrix of a retarder (Equation 2.35) by the rotation transformation (Equation 2.32) :

$$\begin{aligned} \boldsymbol{J}_{\lambda/2}(\gamma, \varpi) &= \boldsymbol{J}(-\varpi)\, \boldsymbol{J}_R(\varphi_{\lambda/2})\, \boldsymbol{J}(\varpi) \\ &= \begin{pmatrix} -sin\gamma + i\, cos\gamma\, cos2\varpi & i\, cos\gamma\, sin2\varpi \\ i\, cos\gamma\, sin2\varpi & -sin\gamma - i\, cos\gamma\, cos2\varpi \end{pmatrix} \end{aligned} \tag{2.37}$$

2.2.3 Analysis of the setup polarimetric responses

2.2.3.1 The calibration setup

The intensity of a light beam is obtained by carrying out the matrix multiplication between the complex transpose of the Jones vector and the Jones vector itself:

$$I = \boldsymbol{E}^* \, \boldsymbol{E} = {E_x}^* \, E_x + {E_y}^* \, E_y \tag{2.38}$$

Therefore, we could use a power meter as a means to extract the Jones vector of the light.

We can simplify the calibrating measurement as schematized in Figure 2.10. The objective has been removed and the red laser ($\lambda \sim 630\,\text{nm}$) was sent through the microscope, mimicking the emission of the nanostructures in its propagating path which passes through the objective's pupil and the pinhole.

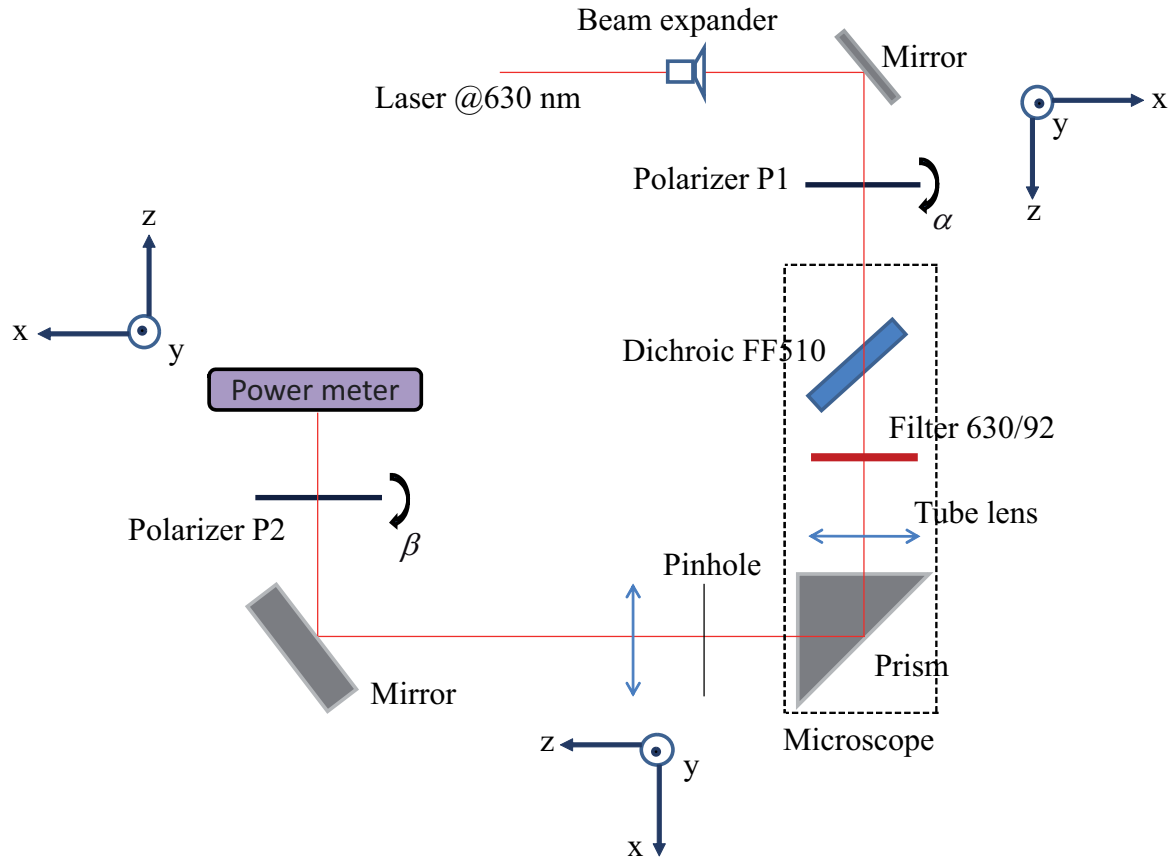

FIGURE 2.10: Schematic configuration of calibrating experiment for the emission polarization measurement setup. The red laser is sent through a beam expander in order to imitate the emission beam after the objective. The polarization of the light is analyzed by rotating a linear polarizer P2 followed by a power meter. Noted that the z axis is always oriented in the direction of propagation and the vectors perpendicular to the dichroic and prism interfaces in the $x-z$ plane are fixed at 45^o to the z direction thanks to the microscope. The mirror is aligned to have its normal vectors in their planes of incidence at 45^o to the z direction as well.

The polarization direction of the incoming light was controlled by a rotating polarization film (P1). We note down the angles indicated on rotating mounts corresponding to the situation when the polarization proper axis of the film is along the x and y reference axis of the entire setup (as illustrated in Figure 2.10). The z axis of the setup is always along the direction of propagation.

The objective is removed in order to keep a collimated beam all along the propagating path. After being reflected on the mirror, the laser followed the propagating way of the typical

emission light, through the dichroic, the filter, the tube lens, the prism, the lens, the mirror, and was finally detected by the power meter. The second polarization film (P2) was also fixed on the rotating mount with marked proper axes. This polarization film was employed as the polarization analyzer for the transmitted light. Experiment is performed by rotating the analyzer P2 around the axis of propagation of the probe light (z axis).

Thanks to the polarizer P1, we could set the input light to be linearly polarized along the x and y direction. The output light showed the same linear polarization state: the transmitted light is extincted if the polarizer P1 and analyzer P2 are crossed. It confirms that the x and y axes of the setup correspond to the proper axes of all the elements of the setup (the x and y polarization directions correspond to s or p directions for each elements).

2.2.3.2 Determination of the transmittance and the dephasing

It is of particular interest to restrict to the case where the incident beam is linearly polarized at an arbitrary angle. This could be done by rotating the axis of the linear polarizer P1 through the angle of α with respect to the x axis of the setup: when $\alpha = 0$ the incident polarization is along x axis of the setup. Its Jones vector is already presented in Equation 2.18 as

$$\boldsymbol{E_\alpha} = \begin{pmatrix} cos\alpha \\ \\ sin\alpha \end{pmatrix}$$

Thus, we have the intensity of the input signal (taken after the polarizer P1) as

$$I_0 = \boldsymbol{E_\alpha}^* \boldsymbol{E_\alpha}$$

The light emerging from the setup will be analyzed by the polarizer P2. We define $\boldsymbol{J}_1$ as the Jones matrix of the microscope, corresponding to the propagation path starting from the dichroic FF510 and finishing after the prism. Thus, the total Jones matrix of the whole system is the product of the Jones matrix for the microscope $\boldsymbol{J}_1$ (Equation 2.31) and the Jones matrix of the analyzer P2 rotated by β from the x axis $\boldsymbol{J}_2(\beta)$ (Equation 2.34). It is readily found as

$$\boldsymbol{J'} = \boldsymbol{J}_2(\beta)\boldsymbol{J}_1$$

The Jones vector of the beam coming out from the polarization analyzer P2 in the experiment shown in Figure 2.10 is then expressed by :

$$\boldsymbol{E'} = \boldsymbol{J'}\boldsymbol{E_\alpha} = t_{Pol}\begin{pmatrix} cos\alpha\, cos^2\beta\, t_x \mathrm{e}^{\frac{i\psi}{2}} + sin\alpha\, sin\beta\, cos\beta\, t_y \mathrm{e}^{\frac{-i\psi}{2}} \\ sin\alpha\, sin\beta\, cos\beta\, t_x \mathrm{e}^{\frac{i\psi}{2}} + sin\alpha\, sin^2\beta\, t_y \mathrm{e}^{\frac{-i\psi}{2}} \end{pmatrix} \tag{2.39}$$

where $t_{pol} = \sqrt{T_{Pol}}$ with T_{Pol} denoting the intensity transmittance of the analyzer P2.

From Equation 2.39, we derive the intensity of the beam emerging from the setup and analyzed by a linear polarizer with the transmittance T_{Pol} as:

$$I' = \boldsymbol{E'^*}\boldsymbol{E'} = I_0 T_{Pol}(cos^2\alpha\, cos^2\beta\, t_x^2 + sin^2\alpha\, sin^2\beta\, t_y^2 + \frac{1}{2}t_x t_y sin2\alpha\, sin2\beta\, cos\psi) \tag{2.40}$$

which depends on the rotating angle α of the first polarizer P1 and β of the analyzer P2. We notice that when they take specific values of 0°, 90°, and 45°, the intensity of the transmitted light holds as shown in 4 following cases:

- Case 1) $\alpha = \beta = 0°$: When P1 and P2 proper axes are along x direction, the normalized value of the intensity of the detected light I_1' over the incident light I_{01} is $\frac{I_1'}{I_{01}} = T_{Pol}\, T_x$ with T_x denoting the transmittance of the setup for the light polarized along x reference direction so that

$$t_x = \sqrt{T_x} = \frac{1}{t_{Pol}}\sqrt{\frac{I_1'}{I_{01}}} \tag{2.41}$$

- Case 2) $\alpha = \beta = 90°$: When P1 and P2 proper axes are along y direction, similarly, the normalized value of the intensity of the output I_2' over input I_{02} is $\frac{I_2'}{I_{02}} = T_{Pol}\, T_y$ with T_y denoting the transmittance of the setup for the light polarized along y reference axis and

$$t_y = \sqrt{T_y} = \frac{1}{t_{Pol}}\sqrt{\frac{I_2'}{I_{02}}} \tag{2.42}$$

- Case 3) $\alpha = \beta = 45°$: When P1 and P2 proper axes are along 45° with respect to the x direction, the normalized value of the intensity of the transmitted light I_3' over the incident light I_{03} is

$$\frac{I_3'}{I_{03}} = T_{Pol}\,(\frac{1}{4}\,{t_x}^2 + \frac{1}{4}\,{t_y}^2 + \frac{1}{2}\mid t_x \mid\mid t_y \mid cos\psi)$$

- Case 4) $\alpha = 45°$ and $\beta = 135°$: When P1 and P2 proper axes are along 45° and 135° with respect to the x direction respectively, the normalized value of the intensity of the detected light I_4' over the incident light I_{03} as

$$\frac{I'_4}{I_{03}} = T_{Pol}(\frac{1}{4}\,{t_x}^2 + \frac{1}{4}\,{t_y}^2 - \frac{1}{2} \mid t_x \mid\mid t_y \mid cos\psi)$$

which yields:

$$I'_3 - I'_4 = T_{Pol} I_{03} \mid t_x \mid\mid t_y \mid cos\psi$$

Then we can calculate the phase retardation ψ introduced by the setup as:

$$cos\psi = \frac{I'_3 - I'_4}{I_{03}\sqrt{\frac{I'_1}{I_{01}}}\sqrt{\frac{I'_2}{I_{02}}}} \tag{2.43}$$

On the other hand, we can characterize the diattenuating behavior of the setup by comparing the values of the transmittance $T_x = {t_x}^2$ (from Equation 2.41) and $T_y = {t_y}^2$ from Equation 2.42) as well.

Hence, by measuring the intensity of the input I_{0a} and the output I'_a with $a = 1, 2, 3, 4$ when the polarizer P1 and the analyzer P2 are put at particular angles, it is possible to obtain the effect that the setup has performed on the given polarization state of the input light. The advantage of this calibrating method is that it is independent of the intensity of the laser source. In addition, the precision rotating mounts make these measurements more accurate.

Conclusion

In this chapter, we have introduced basic informations on the role of polarimetric determination of an emitting dipole in plasmonic/photonic studies. Understand the dipolar orientation is a key factor for further achievements in fabrication of next generation devices with much efficient coupling between the emitter and the nanostructures.

A brief theoretical information of the polarimetric determination of an emitting dipole is reviewed. Our developed model uses the polarization of the collected photoluminescence to quantify the polar and azimuthal angles of the given dipole in the relative configuration with the microscopy substrate, corresponding to the dipolar orientation. The second part addresses our experimental setup in order to perform emission polarization measurement. The principle and the initial proposed experiment are introduced. Then, we present the details of the characterization modelling and analyzing procedures to study the polarization effect of the micsocopy setup. In the next chapter, we will apply these procedures to fully characterize the

realistic setup from analyzing parts to dectecting ones in order to build up a measurement setup with the smallest uncertainity.

Chapter 3

Emission polarization measurement and analysis

Introduction

Several researches have been published on the determination of an emitting dipole by analysing the emission polarization. For example, in her PhD study at INSP [27], C. Lethiec has proven that the dipolar nature of a nano-emitter (its 1D or 2D dimensionality) can be determined by the experimental study on the polarization anisotropy distribution of a statistical collection of several hundreds of individual emitters randomly oriented. Knowing its dipolar dimensionality, the dipolar orientation can be deduced from its photoluminescence′s degree of polarization [62].

However, this statistical method is effective only in the situation when the nanoemitters have random orientations on the substrate′s surface, so that the polarization anisotropy distribution contains all orientation information. It is possibly applied for spherical nanoemitters such as CdSe/CdS core/shell quantum dots [52]. On the other hand, for some new nanostructures such as dot-in-rods or nanoplatelets, the polarization anisotropy distribution is difficult to achieve since the emitters can not be deposited with random orientations [62].

Here, we have recently improved her method to determine an individual dipole by combining the emission polarization measurement and the emission pattern imaging. It should be noted that the emitter′s optical environment near to the planar interface is taken into account. This polarimetric determination measurement can give information on the dipolar dimensionality and the dipolar orientation for each single nanoemitter. Moreover, it avoids the statistical

study of the sample as required in the previously mentioned method.

The subject of this chapter is the emision polarization measurement. We start by characterizing how the microscopy setup modifies the polarization state of the incident emission. In order to limit any polarization change of the experiments, some improvements are performed in the measurement setup. We also consider two possible ways of detection in the realistic experimental setup. Finally, we will conclude on the specifications of the developments we have done in our microscopy setup and on its accuracy in determining the orientation of a given dipole.

3.1 Polarimetric characterization of the experimental setup

The polarization state of the beam transmitted through the experimental setup is determined by the amplitude ratio and the phase difference between two orthogonal components of electric vector. Thus, we will analyze the polarization effect of the setup in term of diattenuation (amplitude change) and retardation (phase change) respectively.

3.1.1 Diattenuation characterization

3.1.1.1 Determination of the diattenuation by the setup

We perform the calibrating measurement as schematized in Figure 2.10 with different laser intensity. The results are shown in Table 3.1. The transmittance T_x and T_y for the light polarized along x and y reference axes are calculated from Equation 2.41 and 2.42. A difference of $8-9\%$ between the transmittance T_x and T_y is the diattenuation due to the setup.

Exp. No.	I_{01}	I_{02}	I'_1	I'_2	T_x	T_y	$T_x - T_y$
1	219.8	132.4	197.1	107.3	89.7%	81%	8.7%
2	262.2	157.2	235.9	128.9	90%	82%	8%
3	240.7	145	215	117.6	89.3%	81.1%	8.2%

Table 3.1: The results of the calibrating measurement for diattenuation characterization perfomed by the initial proposed setup schematized in Figure 2.10. All the intensity are in μW units.

In order to find the main factor introducing the diattenuating effect(as presented in Table

3.1) in the setup, we perform a side calibrating measurement for the dichroic used in the setup. Figure 3.1 illustrates the experiment for characterizing our dichroic beamsplitter FF510-Di01. The dichroic is fixed on a rotation mount so that we can vary the incident angle β' by turning the mount. It should be noted that the uncertainty of the rotation mount is $\pm 0.5^{o}$. Two rotatable polarizer P1 and P2 with marked proper axes are placed before and after the dichroic in order to polarize the input and then select the polarization component of the output.

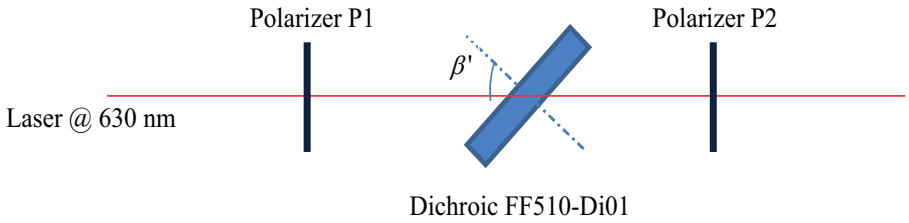

FIGURE 3.1: Schematic of diattenuation measurement of our dichroic beamsplitter FF510-Di01 (@Semrock) characterizing the relation of the transmittance for s and p polarized light of this dichroic and the incident angle β'.

The transmittance of an optical element is defined as the fraction of the incident light that is transmitted through the element, so that the transmittance along the s and p direction of the dichroic FF510-Di01 is given respectively by:

$$T_s = \frac{I^s_{P2}}{T_{P2} I^s_{P1}} \tag{3.1}$$

$$T_p = \frac{I^p_{P2}}{T_{P2} I^p_{P1}} \tag{3.2}$$

where I^s_{P1} and I^s_{P2} are obtained by a power meter placed right after the polarizer P1 and the analyzer P2, respectively, when both their transmission axes are along the s direction, while I^p_{P1} and I^p_{P2} are taken similarly when these axes parallel to the p direction with the maximum transmittance of the polarizing analyser P2 being $T_{P2} = 0.95$.

Figure 3.2(a) depicts the experimental values of the transmittance along the s and p direction of the dichroic beamsplitter employed in our setup obtained by the measurements as described in Figure 3.1. The difference between the transmittance T_p and T_s is about 6% when the incident angle is about 45^{o}. On the other hand, it is known from the specification data [81] that the dichroic beamsplitter FF510-Di01 employed in our setup has its natural diattenuation depending on the incident angle, as observed in Figure 3.2(b). When the incident angle varies from 40^{o} to 50^{o}, the diattenuation changes. When the light is incident on the dichroic at an angle of 45^{o}, the difference between the transmittance T_p and T_s is about 6%, confirming the experimental conclusion.

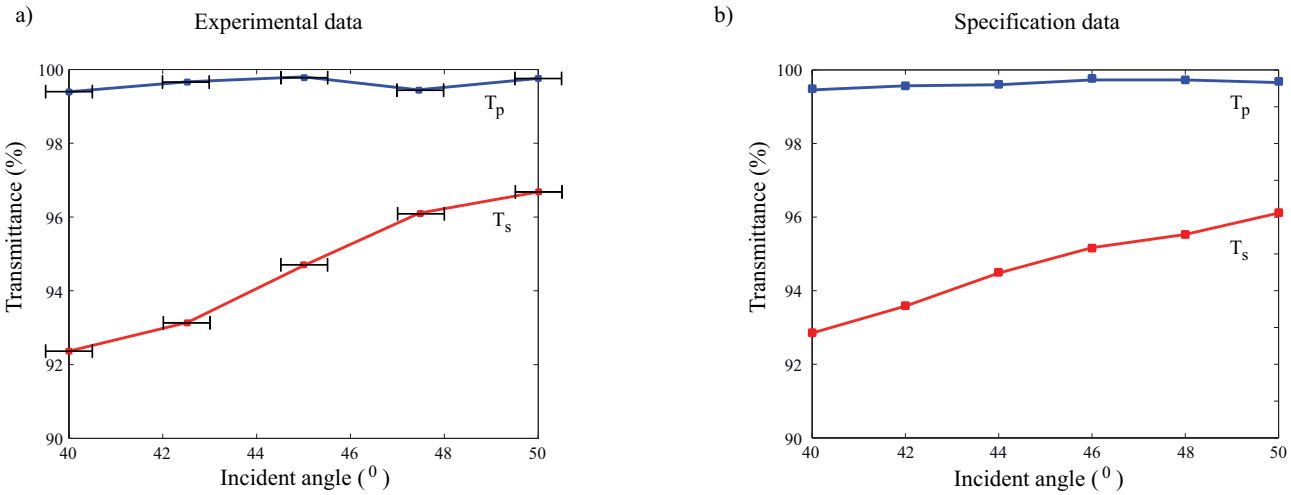

FIGURE 3.2: (a) The dependence on the incident angle β' of the transmittance for s and p polarized light of the dichroic beamsplitter FF510-Di01: (a) obtained by Equation 3.1 and 3.2 from the experiment schematized in Figure 3.1 with the mount 's uncertainty ($\pm 0.5^o$) and (b) taken from the specification data from Semrock [81].

It should be noted here that the s and p polarizations are in relation to the plane of incidence of the dichroic beamsplitter. In our experimental setup, thanks to the microscope, the dichroic is fixed with its s and p directions corresponding to the y and x directions of the setup, respectively. In the specifications provided by Thorlab company, the diattenuation $(T_p - T_s)$ of the dichroic is quite close to the value of $(T_x - T_y)$ measured in our proposed setup.

Since we did not obtain any considerable diattenuation effect in other optical elements of our setup as we found in the dichroic, the diattenuating effect of the setup mainly results from the nature of dichroic beamsplitter.

3.1.1.2 Balancing the diattenuation

To completely compensate this diattenuation effect, another dichroic beamsplitter with the same characteristics was inserted on the propagating way perpendicularly with respect to the first dichroic beamsplitter (which is permanently fixed inside the cube turret of the microscope). Let us consider the light with the component of along x reference direction, illustrated by a black arrow and y reference direction illustrated by a green arrow respectively in Figure 3.3.

As the plane of incidence of the first dichroic D1 is the plane normal to its surface along the direction of propagation (z axis), the x component of the incident beam would appear to be in this plane, so it is p polarized for the dichroic D1. Due to the orthogonal setting of 2 dichroic beamsplitters, their planes of incidence are also perpendicular to each other. Since the

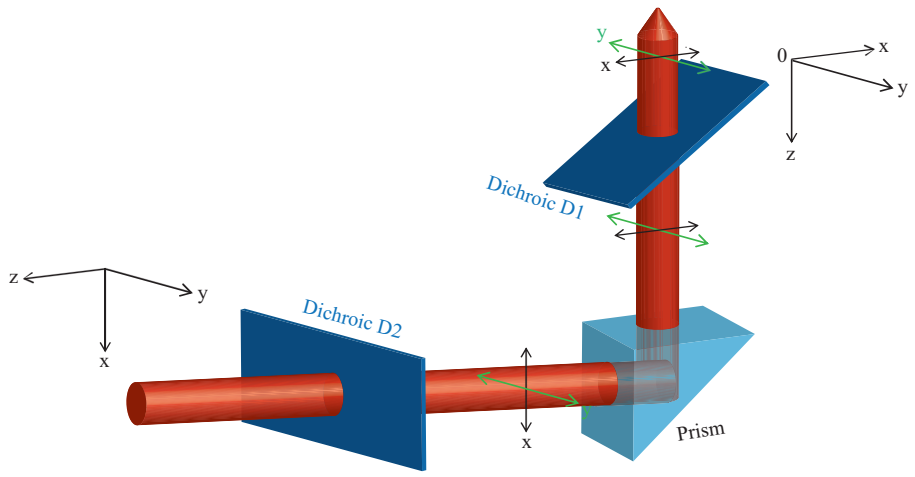

FIGURE 3.3: Schematic of the orthogonal setting of 2 identical dichroics in our setup. The component of the light along x axis (the black arrow) is p polarized with respect to the first dichroic D1 but it would be s polarized with respect to the additional dichroic D2.

beam reflects on the prism, the x component of the incident beam appearing as p polarization with respect to the first dichroic D1 will be orthogonal to the plane of the incidence of the additional dichroic D2, corresponding to the s polarization with respect to the dichroic D2 as described in Figure 3.3. Similarly, the y component of the beam is s polarized for the dichroic D1 but p polarized for the dichroic D2. Therefore, the difference of transmission between s and p polarized component of a beam will be nullified when it propagates through both dichroic beamsplitters.

The diattenuation eliminated setup is schematized in Figure 3.4. The adding dichroic beamsplitter D2 is also FF510-Di01 from Semrock. This additional dichroic D2 is fixed on a rotation mount which is capable of turning around the x reference axis. As seen in Figure 3.5, the s and p polarizing directions of the dichroic D2 correspond to the x and y reference axes and its plane of incidence is the (y-z) plane. By rotating the mount, we can change the incident angle β'_{D2}.

We perform the calibrating measurement in the setup depicted in Figure 3.4 with different values of β'_{D2} by using linearly polarized beam along x and y direction, and calculate the transmittance along reference axes T_y and T_x of the setup by Equation 2.41 and 2.42. The results are presented in Figure 3.6. It should be noted that nearly no light is transmitted (only tens of nW) in all the investigated situations when the transmission axes of the polarizer P1 and the analyzer P2 are placed orthogonally, indicating that the proper axes of all optical elements in our setup are along the x and y reference directions.

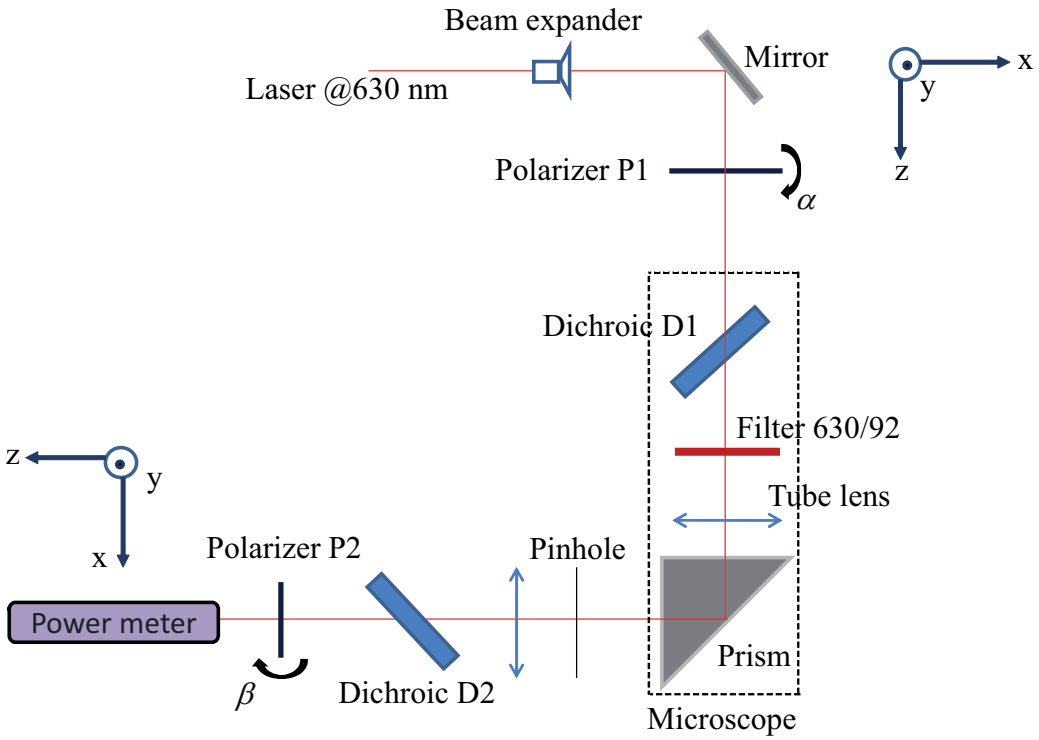

FIGURE 3.4: Schematic configuration of the emission polarization measurement setup with diattenuation elimination by adding the second dichroic beamsplitter. Noted that the z axis is always oriented along the direction of propagation and the vectors normal to the dichroic D1 and prism interfaces in the $(x-z)$ plane are fixed at 45^o to the z direction thanks to the microscope.

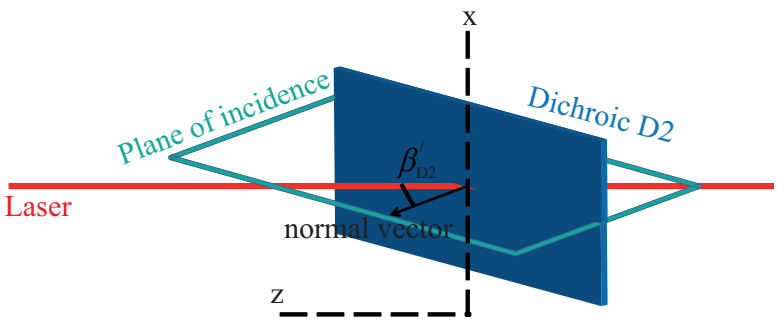

FIGURE 3.5: Schematic of the additional dichroic D2 in our setup.

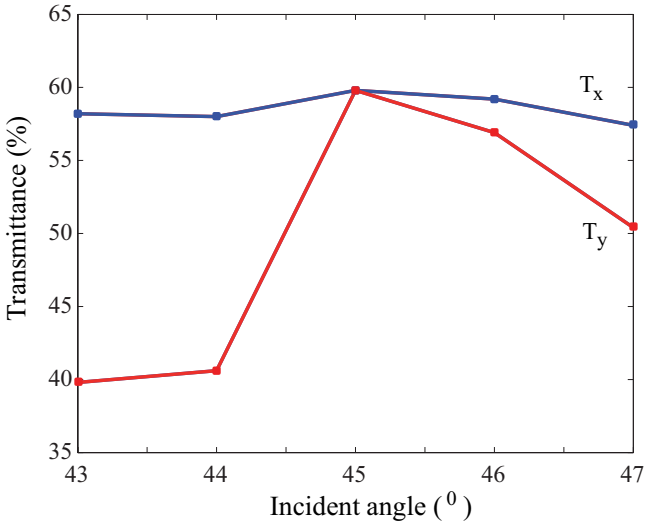

FIGURE 3.6: The transmittance along x and y reference axes of the diattenuation eliminated setup schematized in Figure 3.4 when increasing the incident angle β'_{D2} of the additional dichroic D2.

In Figure 3.6, the transmittance of the whole system along the reference axes $T_x \approx T_y \approx 0.6$ for the incident angle of the additional dichroic D2 of 45°, indicating that there is no diattenuating effect in our setup anymore. Therefore, the second dichroic beamsplitter D2 will be fixed in order to have the angle of 45° between its normal vector and the z direction in the (y-z) plane of the reference axes to remove the diattenuation caused by the first dichroic D1.

3.1.2 Retardation characterization

3.1.2.1 Determination of the dephasing of the experimental setup

After fixing the additional dichroic D2 position, we reperform the calibrating measurement with the diattenuation eliminated setup depicted in Figure 3.4 to characterize the retardation induced by the setup with different polarization state and intensity of the excition laser. The results are presented in Table 3.2. The first experiment (ex1) and the second one (ex2) are with same lasing polarization but different lasing intensity. Then we change the lasing polarization then repeat for the third (ex3) and the forth (ex4). By rotating the axis of the linear polarizer P1 through the angle of α with respect to the x axis of the setup ($\alpha = 0$ when the incident polarization is along x reference axis), we measure the intensity of the beam entering the setup by the power meter inserted right after the polarizer P1: I_{0a} with $a = 1, 2, 3$ as when the polarizer P1 are put at $\alpha = 0, 90°, 45°$ respectively. Similarly, the intensity of the output I'_a with $a = 1, 2, 3, 4$ are obtained by the power meter followed the polarizer P2 when $\beta =$

$0, 90^o, 45^o, 135^o$. In all the experiments, it is confirmed that there is no diattenuating effect as $T_x \approx T_y$. Thanks to Equation 2.43 the phase retardation ψ between the s and p polarization is estimated approximately 55^o:

Exp. No.	I_{01}	I_{02}	I_{03}	I'_1	I'_2	I'_3	I'_4	T_x	T_y	ψ
ex1	1250	96.8	407	685	52.9	163.5	30.6	58%	57%	54.8^o
ex2	4880	139	2030	2940	55.3	850	131.2	60%	61%	51.3^o
ex3	1932	858	258.4	1211	548	120	26.4	62%	63%	55.1^o
ex4	2250	1040	299	1410	651	133.8	35.5	62%	62%	58.4^o

Table 3.2: The results of the calibrating measurement for diattenuation and retardation characterization perfomed by the diattenuation eliminated setup schematized in Figure 3.4 with different polarization states of laser (ex1/ex2 and ex3/ex4) and differnet lasing intensity (ex1 and ex2; ex3 and ex4). All the intensity are in μW units.

3.1.2.2 Determination of the dephasing of prism

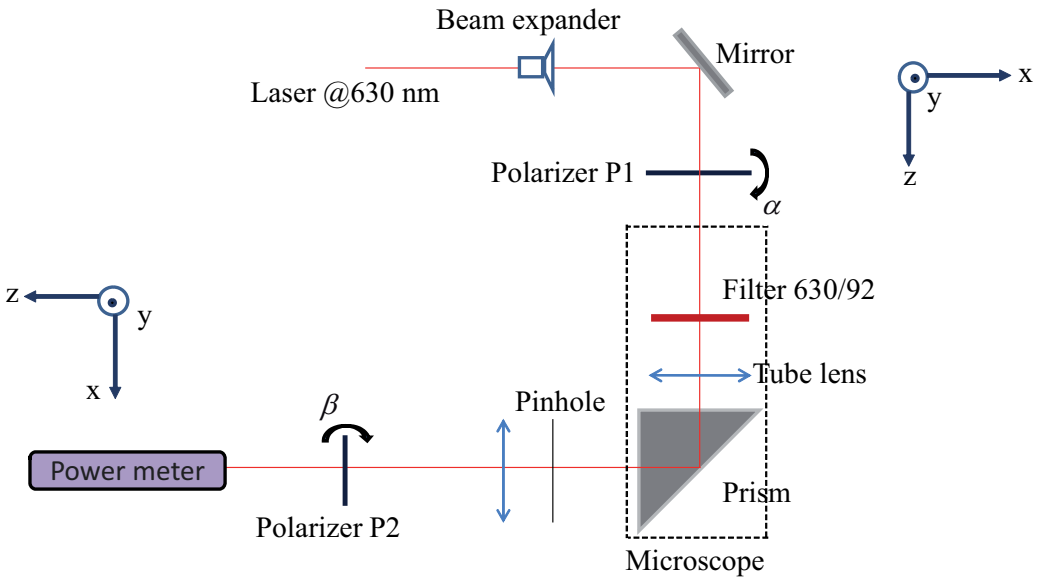

FIGURE 3.7: Schematic configuration of the side measurement for characterizing the retardation effect of the prism inside the microscope. Noted that the z axis is always oriented along the direction of propagation and the vectors normal prism interfaces in the $x-z$ plane are fixed at 45^o to the z direction thanks to the microscope.

As the prism of the microscope is normally considered as a retarder, we will characterize its retardation first. We make a small checking measurement for only the prism inside the microscope, as pictured in Figure 3.7. The obtained results are listed in Table 3.3. It is to be

α	β	I_{P1}	I_{P2}
0°	0°	4900	3170
0°	90°	4900	12
90°	0°	146.5	1.5
90°	90°	146.5	96
45°	45°	2040	1016
45°	135°	2040	188

Table 3.3: The results of the side checking measurement for retardation characterization perfomed by the setup illustrated in Figure 3.7. All the intensity are in μW units.

recalled that α and β are the angle to the x reference direction of the transmission axis of the polarizer P1 and the analyzer P2 respectively. When the analyzer P2 axis is at 90° and the polarizer P1 one is along x axis, the light is eliminated. It ensures that the vector normal to the prism interface lies in the $x - z$ reference plane and the s and p polarization directions of the prism are also along the y and x reference axes. If the polarizers P1 and P2 are turned to $\alpha = 45°$ and $\beta = 135°$, a small amount of the transmission light remains, resulting from the dephasing of the prism.

Carrying out the calculation in Equation 2.41, 2.42, and 2.43, we have the transmission of the microscope with only the prism along x and y direction $T_x \approx T_y \approx 0.65$ and the phase retardation $\psi \approx 52°$, close to the value obtained for the setup including the compensating two dichroics. Therefore, with our setup alignment, the retardation effect may mainly result from the prism inside the microscope.

3.1.2.3 Reducing the dephasing

Since the diattenuation effect of the setup has been eliminated by the additional dichroic beamsplitter, with the same idea, we will insert in the propagating way an other prism with the same retardation turned by 90° in respect to the first prism, as illustrated in Figure 3.8.

As the plane of incidence of the first prism Pm1 is the plane perpendicular to its surface containing the propagation vector (along z reference axis), the x component of the incident beam is in this plane, refering to p polarization. The additional prism Pm2 is inserted perpendicularly to the first prism Pm1 so that their planes of incidence are also perpendicular to each other. The p polarized component with respect to the first Pm1 will correspond to the s polarized one with respect to the additional prism Pm2 as illustrated in Figure 3.8. In a similar way, the y

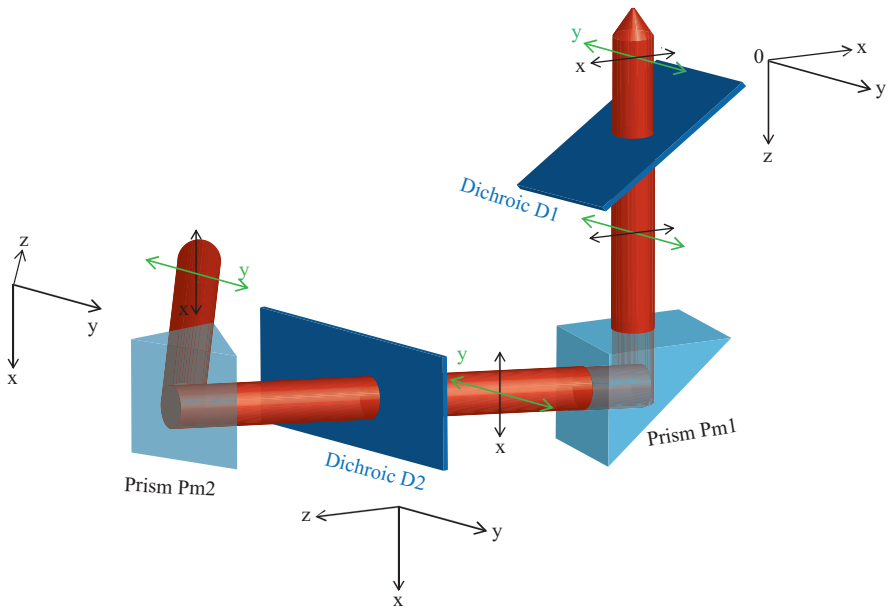

FIGURE 3.8: Schematic of the orthognal setting of 2 prisms in our setup. The component of the light along x axis (the black arrow) is p polarized one with respect to the first prism Pm1 but s polarized with respect to the additional prism Pm2.

component of the beam is s polarized for the prism Pm1 while it is considered as p polarized for the prism Pm2. Therefore, when light passes through both prisms, both orthogonal components are phase shifted in the same way, so the retardation between them would remain the same.

The retardation eliminated setup is presented in Figure 3.9. With this improvement, when we perform the calibrating measurement, we get the new phase retardation ψ down to $5^o - 8^o$, which is acceptable in the experimental accuracy limit.

When the phase retardation of the setup reduces to be 8^o, the corresponding theoretical dependence of the degree of polarization δ on the polar angle Θ of the emitting dipole in two extreme cases : when $\Phi_{mes} = 45^o$ (minimum M = 0.97, red lines) and $\Phi_{mes} = 0^o$ (maximum M = 1, blue lines) for a one dimensional and two dimensional dipole is represented in Figure 3.10. As discussed in subsection 2.1.4, the measured azimuthal angle Φ_{mes} is extracted directly from the phase of the sinusoidal curve. It is related to the actual orientation Φ of the dipole by:

$$cos\psi tan2\Phi = tan2\Phi_{mes}$$

The degree of polarization measured from the contrast of the sinusoidal curve δ_{mes} is related to the actual value $\delta(\Theta)$ (obtained when $\psi = 0$, which corresponds to the orientation of the dipole) by the following relationship:

$$\delta_{mes} = \delta(\Theta)\frac{cos2\Phi}{cos2\Phi_{mes}}$$

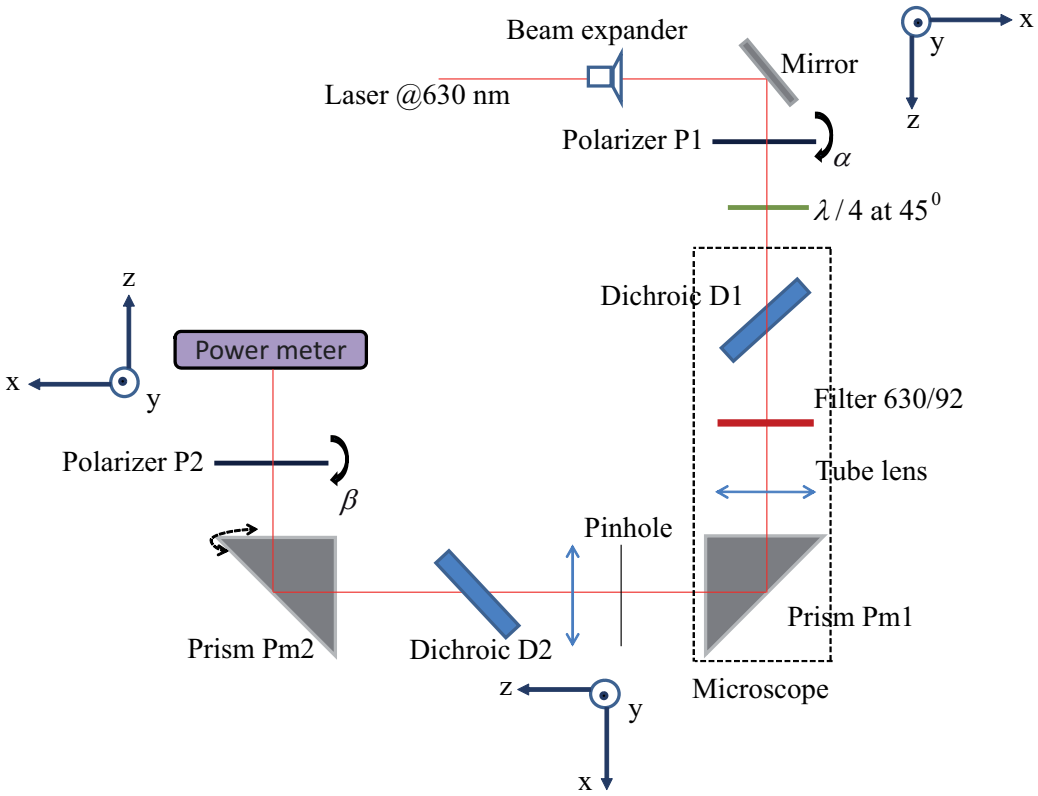

FIGURE 3.9: Schematic configuration of the emission polarization measurement setup with diattenuation elimination by adding the second dichroic beamsplitter and retardation elimination by replacing the mirror by an additional prism. The detailed orthogonal arrangement of the dichroics and prisms is presented in Figure 3.8. Noted that the z axis is always oriented in the direction of propagation.

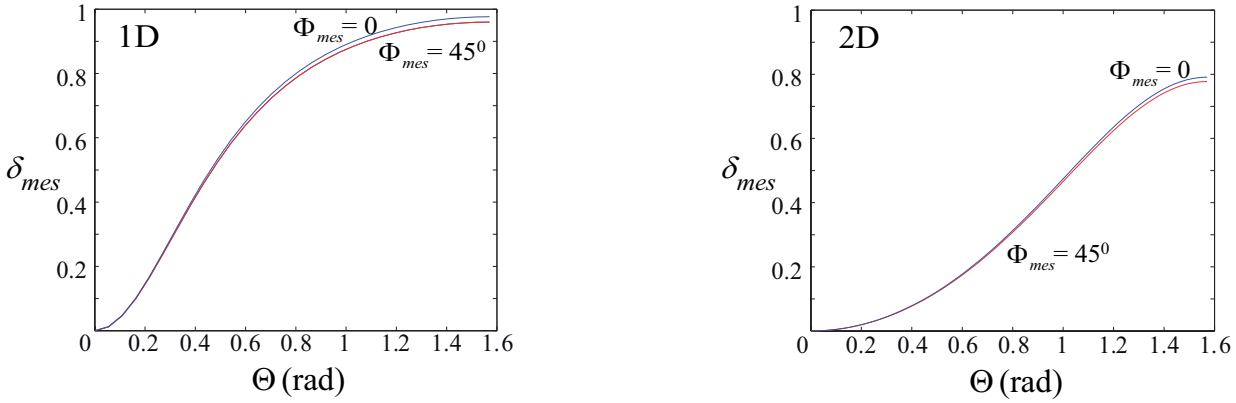

FIGURE 3.10: The setup's phase retardation $\psi = 8^o$: Theoretical values of δ as a function of the angle Θ for a one dimensional dipole (a) or a two dimensional dipole (b) in two extreme cases when factor M are maximum ($\Phi_{mes} = z_1\, 90^o$) and minimum ($\Phi_{mes} = 45^o + z_1\, 90^o$) respectively, calculated in the reflection configuration (the emitter is at a distance of 50 nm to the gold-PMMA interface, oil objective with $NA = 1.4$

It should be reminded that when $\Phi_{mes} = 0^o$, $\delta_{mes} = \delta(\Theta)$. From Figure 3.10, we have with the setup′s dephasing $\psi = 8^o$, the difference between δ_{mes} and $\delta(\Theta)$ when $\Phi_{mes} = 45^o$ is just 3%. Since $\Phi_{mes} = 45^o$ is the case for which the difference is the biggest, we can conlcude that **the difference between our measured values and the actual values is just less than 3%, which is acceptable**.

3.2 Realistic experimental setup including the detection part

In the experimental emission polarization measurement setup, we would like to perform the antibunching measurement as well. Therefore, we utilize the combination of a rotating halfwave plate and a polarizing beam splitter cube instead of a rotating polarizer. The new calibrating setup is displayed in Figure 3.11. Using two photodiodes namely AP1 and APD2 makes it possible to normalize obtained intensity so that the fluctuations of the photoluminescent intensity are removed.

3.2.1 The Jones matrix of the setup with two ways of detection

In order to check if the use of a halfwave plate and a polarizing cube instead of a polarizer affects the polarimetric measurement, we turn our attention to compare the Jones matrix of each detecting way. The polarization of the light entering the setup is controlled by a set of the polarizer P1 followed by the quarterwave plate, both of which are rotatable around the z axis (the direction of propagation), as described in Figure 3.11.

To be simple, we would fix the quarterwave plate to be at 45^o with respect to x direction of the reference axes. Thus, when the beam incident on the quarterwave plate is also polarized along the 45^o linear polarization direction with respect to x axis (by rotating the polarizer P1 to $\alpha = 45^o$), the axis of polarizer P1 is parallel with the axis of the quarterwave plate, so that the input of the setup (after the quarterwave plate) is linearly polarized. On the other hand, when the axis of the polarizer P1 is set along the x direction, the transmitting polarized light incident on the quarterwave plate has its polarization at 45^o with respect to proper axes of the quarterwave plate. It is transformed into a circularly polarized light after the quarterwave plate, then entering the microscope. From Equation 2.36, we have the Jones matrix representing the

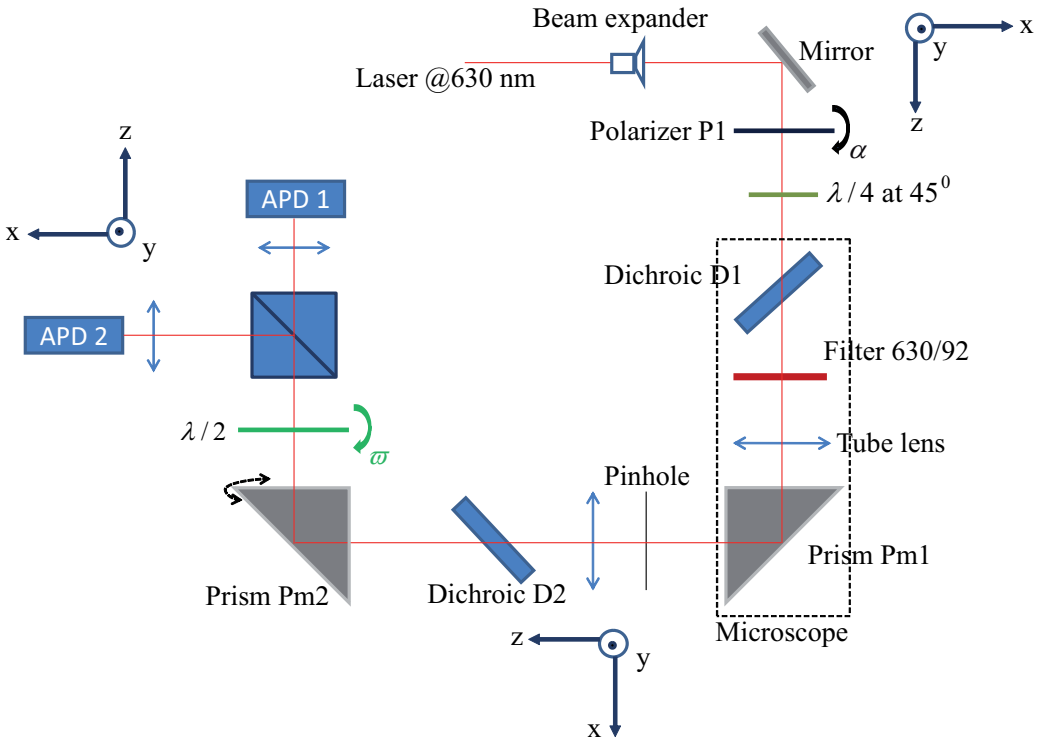

FIGURE 3.11: Schematic configuration of the emission polarization measurement setup with diattenuation and retardation corrections. The polarization analysis is performed by a combination of a rotating halfwave plate $\lambda/2$ and a polarizing beam splitter cube (PBS). Noted that the z axis is always oriented in the direction of propagation.

quarterwave plate with its fast axis at $\nu = 45^{o}$ from the x axis as

$$\boldsymbol{J}_{\lambda/4}(\varphi_{\lambda/4}, 45^{o}) = \begin{pmatrix} cos\varphi'_{\lambda/4} & i\,sin\varphi'_{\lambda/4} \\ i\,sin\varphi'_{\lambda/4} & cos\varphi'_{\lambda/4} \end{pmatrix} \tag{3.3}$$

where $\varphi_{\lambda/4} = 2\varphi'_{\lambda/4} = \dfrac{\pi}{2} + 2\vartheta$ with $\vartheta = 0$ when the quarterwave plate is ideal.

We compare two detection ways as follows:

- When analyzing the output by a polarization analyzer P2 rotated by β with respect to the x reference axis and its intensity transmittance of $T_{Pol} = 0.8$, we can simplify the Jones sequence representing each part of the setup to a total Jones matrix by :

$$\boldsymbol{J'}_2 = \boldsymbol{J}_2(\beta)\,\boldsymbol{J}_1\,\boldsymbol{J}_{\lambda/4}(\varphi_{\lambda/4}, 45^{o}) \tag{3.4}$$

  where the Jones matrix of the analyzer P2 $\boldsymbol{J}_2(\beta)$ is given by Equation 2.34, the Jones matrix of the setup $\boldsymbol{J}_1$ is given by Equation 2.31 with $T_x \approx T_y \approx 0.6$ and $\psi = 8^{o}$, and the Jones matrix of the 45^{o} turned quaterwave plate $\boldsymbol{J}_{\lambda/4}(\varphi_{\lambda/4}, 45^{o})$ is given by Equation 3.3 with $\varphi_{\lambda/4} = 0.56\pi$ taken from its specification sheet by Thorlab [80].

  Carrying out the matrix multiplication in Equation 3.4 yields the Jones matrix of the whole system :

$$\boldsymbol{J'}_2 = T_{Pol}\,T_x \begin{pmatrix} cos^2\beta\,cos\varphi'_{\lambda/4}\,e^{\frac{i\psi}{2}} + i\,sin\beta\,cos\beta\,sin\varphi'_{\lambda/4}\,e^{\frac{-i\psi}{2}} & i\,cos^2\beta\,sin\varphi'_{\lambda/4}\,e^{\frac{i\psi}{2}} + sin\beta\,cos\beta\,cos\varphi'_{\lambda/4}\,e^{\frac{-i\psi}{2}} \\ i\,sin^2\beta\,sin\varphi'_{\lambda/4}\,e^{\frac{-i\psi}{2}} + sin\beta\,cos\beta\,cos\varphi'_{\lambda/4}\,e^{\frac{i\psi}{2}} & sin^2\beta\,cos\varphi'_{\lambda/4}\,e^{\frac{-i\psi}{2}} + i\,sin\beta\,cos\beta\,sin\varphi'_{\lambda/4}\,e^{\frac{i\psi}{2}} \end{pmatrix} \tag{3.5}$$

- When we analyze the transmitted beam by a halfwave plate rotated by ϖ, which introduces a phase retardation of $\varphi_{\lambda/2} = 2\varphi'_{\lambda/2} = \pi + 2\gamma$ ($\gamma = 0$ for the ideal quarterwave plate) at the wavelength of emission $(630 - 650nm)$, and a polarizing beamsplitter cube with the corresponding Jones matrix written as :$\boldsymbol{J}_4 = \begin{pmatrix} t_{Cub} & 0 \\ 0 & 0 \end{pmatrix}$ with $T_{Cub} = t^2_{Cub} \approx 1$ being its transmittance for s polarized light.

  The resulting Jones matrix for the whole system with the rotated halfwave plate followed

by the polarizing cube is then expressed as :

$$\boldsymbol{J'}_3 = \boldsymbol{J}_4\,\boldsymbol{J}_{\lambda/2}(\gamma,\vartheta)\,\boldsymbol{J}_1\,\boldsymbol{J}_{\lambda/4}(\varphi_{\lambda/4}, 45^{\mathrm{o}}) \tag{3.6}$$

where the Jones matrix of the rotating halfwave plate $\boldsymbol{J}_{\lambda/2}(\gamma,\vartheta)$ is given by Equation 2.38 with $\gamma = (\varphi_{\lambda/2} - \pi)/2 \approx 2^{\mathrm{o}}$ as $\varphi_{\lambda/2} = 1.024\,\pi$ obtained from the specification data of Thorlab [80].

3.2.2 The incident light is linearly polarized

Firstly, we consider the case when the beam entering the setup is linearly polarized. The polarization state of the input light is controlled by a rotating linear polarizer P1 and a fixed quarterwave plate at 45° with respect to x direction of the reference axes.

Since the quarterwave plate is fixed at 45° to the x axis, by rotating the polarizer P1 in order to get $\alpha = 45^{\mathrm{o}}$, the input of the setup (after passing the polarizer P1 and the quarterwave plate) is actually linearly polarized at 45° with respect to the x reference direction. We have the incident Jones vector $\boldsymbol{E}_{0_{45}} = E_x \dfrac{1}{\sqrt{2}} \begin{pmatrix} 1 \\ 1 \end{pmatrix}$ and $I''_0 = \boldsymbol{E_{0_{45}}}^{*}\boldsymbol{E_{0_{45}}}$.

3.2.2.1 Analysis by a rotatable linear polarizer

When the output is analyzed by a linear analyzer rotated by β with the intensity transmittance of $T_{Pol} = 0.8$, the Jones vector of the output is represented by $\boldsymbol{E''}_1 = \boldsymbol{J'}_2\,\boldsymbol{E}_{0_{45}}$ and its intensity would be:

$$I''_1 = \frac{1}{2} I''_0\,T_{Pol}\,T_x\,(1 + sin2\beta\,cos\psi) \tag{3.7}$$

with the intensity transmittance and retardation of the set up being $T_x \approx 0.6$ and $\psi = 8^{\mathrm{o}}$, respectively.

3.2.2.2 Analysis by a rotatable halfwave plate and a polarizing beamsplitter cube

When analyzing the transmitted beam by a rotating halfwave plate ($\varphi_{\lambda/2} = \pi + 2\gamma = 1.024\,\pi$) rotated by ϖ followed by a polarizing beamsplitter cube with the transmittance of T_{Cub}, the Jones vector of the beam emerging from the setup is expressed as $\boldsymbol{E''}_2 = \boldsymbol{J'}_3\,\boldsymbol{E}_{0_{45}}$. The intensity of this emerging beam is thus calculated as:

$$I_2'' = \frac{1}{2} I_0'' \, T_{Cub} \, T_x \, (1 + 2 \, sin2\varpi \, cos\gamma(-sin\gamma \, sin\psi + cos2\varpi cos\gamma \, cos\psi)) \tag{3.8}$$

where $\gamma = 2^o$ and $T_{Cub} = 0.99$.

It should be noted that the Equation 3.7 can be reduced from the Equation 3.8 when $\gamma = 0$, referring to an ideal halfwave plate. We also have $2\varpi = \beta$, as a halfwave plate can rotate the polarization of linearly polarized light to twice the angle between its fast axis and the plane of polarization. In this case, a combination of an ideal halfwave plate and a polarizing beamsplitter cube works equivalentlly to a linear polarizer.

3.2.2.3 Comparison between two ways of detection

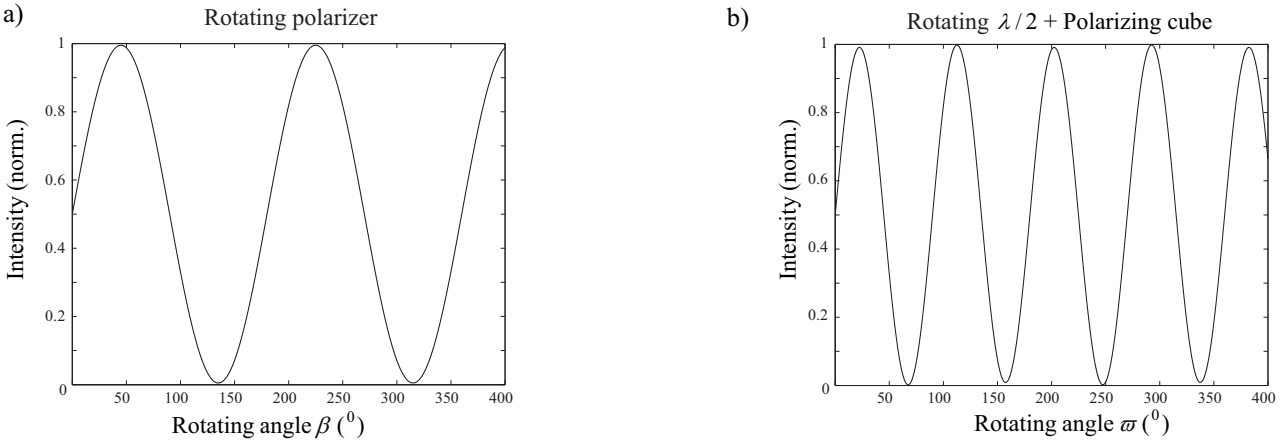

FIGURE 3.12: The simulating normalized intensity of the output when using 2 different setting way to obtain the signals when the incident light is linearly polarized at 45^o with respect to the proper axes of the setup: (a) by a rotating polarizer by angle β and (b) by a set of a rotating non-ideal halfwave plate ($\gamma = 2^o$) by angle ϖ followed by a polarizing beamsplitter cube, while rotations from 0^o to 400^o are performed.

The polarization of light is described quantitatively by the degree of polarization, defined as:

$$\delta = \frac{I_{max} - I_{min}}{I_{max} + I_{min}} \tag{3.9}$$

where I_{min} and I_{max} are the minimum and maximum intensities of the light, respectively. Figure 3.12 shows the calculating normalized intensity of the final output when it is analyzed by a rotating polarizer ($\frac{I_1''}{I_0'' \, T_{Pol} \, T_x}$ from Equation 3.7) or by a combination of a rotating halfwave plate and a polarizing beam splitter cube ($\frac{I_2''}{I_0'' \, T_{Cub} \, T_x}$ from Equation 3.8) while the input is linearly polarized along the direction at 45^o with respect to the x reference axis (referring to

the degree of polarization $\delta_{in} = 1$).

The degree of polarization of the output δ_{out} remains its maximum in both cases $\delta_{out1} = \delta_{out2} = 1$, indicating that the setup helps keeping the original linear polarization state of the input. Since the electrical field underges a rotation of two times the angle between its direction and the axis of the halfwave plate, the rotating angle β of the polarization analyzer P2 for a complete period is two times ϖ of the halfwave plate as expected. Therefore, **for the case of linearly polarized incident light, it is possible to change the analyzing polarizer to a set of a rotating halfwave plate and a polarizing beamsplitter cube**.

3.2.3 The incident light is circularly polarized

We move on to characterize the effect of the setup on an incident circularly polarized light. The quarterwave plate is fixed at 45° to the x axis. Therefore, if the light incident on the quarterwave plate is along the reference axis, for example, x direction, the beam, after passing through the polarizer P1 and the quarterwave plate, is circularly polarized when entering the setup.

3.2.3.1 State of polarization after the quarterwave plate

In order to analyze the beam incident on the system, we place the polarizer analyzer P2 right after the quarterwave retarder, so the total Jones matrix is calculated by :

$$\begin{aligned} \boldsymbol{J'}_1 &= \boldsymbol{J}_2(\beta)\, \boldsymbol{J}_{\lambda/4}(\varphi_{\lambda/4}, 45^o) \\ &= t_{Pol} \begin{pmatrix} cos^2\beta\, cos\varphi'_{\lambda/4} + i\, sin\beta\, cos\beta\, sin\varphi'_{\lambda/4} & i\, cos^2\beta\, sin\varphi'_{\lambda/4} + sin\beta\, cos\beta\, cos\varphi'_{\lambda/4} \\ i\, sin^2\beta\, sin\varphi'_{\lambda/4} + sin\beta\, cos\beta\, cos\varphi'_{\lambda/4} & sin^2\beta\, cos\varphi'_{\lambda/4} + i\, sin\beta\, cos\beta\, sin\varphi'_{\lambda/4} \end{pmatrix} \end{aligned} \tag{3.10}$$

where the Jones matrix for a rotated polarizer $\boldsymbol{J}_2(\beta)$ is given by Equation 2.34 with $t^2_{Pol} = T_{Pol} = 0.8$ is its intensity transmittance and for the 45° turned quater waveplate $\boldsymbol{J}_{\lambda/4}(\varphi_{\lambda/4}, 45^o)$ is given by Equation 3.3 with $\varphi_{\lambda/4} = 0.5\pi$ (the ideal quarterwave plate) or $\varphi_{\lambda/4} = 0.56\pi$ (specification data at the emission′ wavelength) [80].

As the incident light is linearly horizontally polarized (corresponding to x axis of the

setup), so its Jones vector is written by :

$$\boldsymbol{E}_{0_x} = E_x \begin{pmatrix} 1 \\ 0 \end{pmatrix} \tag{3.11}$$

.

Multiplying Equation 3.11 by Equation 3.10, we find the Jones vector of the beam entering the setup as :

$$\boldsymbol{E'}_1 = \boldsymbol{J'}_1 \, \boldsymbol{E}_{0_x} = E_x \, t_{Pol} \begin{pmatrix} cos^2\beta \, cos\varphi'_{\lambda/4} + i \, sin\beta \, cos\beta \, sin\varphi'_{\lambda/4} \\ i \, sin^2\beta \, sin\varphi'_{\lambda/4} + sin\beta \, cos\beta \, cos\varphi'_{\lambda/4} \end{pmatrix} \tag{3.12}$$

Then the intensity of the setup′s input obtained by placing the polarizer P2 right after the quarterwave plate is :

$$I'_1 = \boldsymbol{E'_1}^* \boldsymbol{E'_1} = I'_0 \, T_{Pol}(cos^2\varphi'_{\lambda/4} \, cos^2\beta + sin^2\varphi'_{\lambda/4} \, sin^2\beta) \tag{3.13}$$

where $I'_0 = \boldsymbol{E_{0_x}}^* \boldsymbol{E_{0_x}}$.

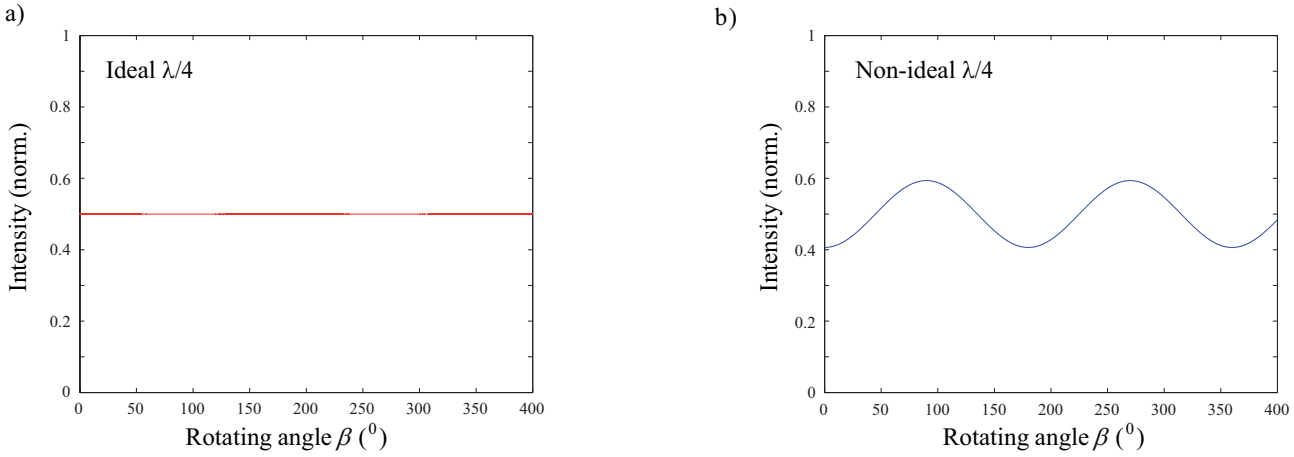

FIGURE 3.13: The normalized intensity of the incoming light of the setup simulated by Equation 3.13 for (a) an ideal quarterwave plate and (b) a non-ideal quarterwave plate when the rotation from 0^o to 400^o of the analyzer P2 (placed after the quarterwave plate) is performed.

Figure 3.13 depicts the normalized intensity $\frac{I'_1}{I'_0\,T_{Pol}}$ of the beam entering the setup calculated from Equation 3.13. If the quarterwave plate works ideally ($\varphi_{\lambda/4} = 0.5\pi$), the degree of polarization is $\delta_{in} = 0$, the input is perfectly circularly polarized, as shown in Figure 3.13(a). However, in the realistic setup, since the quarterwave plate has a retardation $\varphi_{\lambda/4} = 0.56\pi$ at the wavelength of about 650 nm [80], the degree of polarization of the light exiting the quarterwave plate is $\delta_{in} \approx 0.2$, indicating that it is not ideally circular polarization.

3.2.3.2 State of polarization of the detected light

Let us consider 2 detection cases:

- When the analyzing part of the setup is a polarization analyzer P2 rotated by β with respect to the x direction and its transmittance of T_{Pol}, corresponding to the case of placing the polarization analyzer P2 after the second prism (as schematized in Figure 3.9). The Jones matrix of the entire setup $\boldsymbol{J'}_2$ is already represented by Equation 3.5. The Jones vector $\boldsymbol{E'}_2$ and the intensity I'_2 of the setup′s output are similarly found to be:

$$\boldsymbol{E'}_2 = \boldsymbol{J'}_2\,\boldsymbol{E}_{0_x} = E_x\,t_{Pol}\,t_x \begin{pmatrix} cos^2\beta\,cos\varphi'_{\lambda/4}\,\mathrm{e}^{\frac{i\psi}{2}} + i\,sin\beta\,cos\beta\,sin\varphi'_{\lambda/4}\,\mathrm{e}^{\frac{-i\psi}{2}} \\ i\,sin^2\beta\,sin\varphi'_{\lambda/4}\,\mathrm{e}^{\frac{-i\psi}{2}} + sin\beta\,cos\beta\,cos\varphi'_{\lambda/4}\,\mathrm{e}^{\frac{i\psi}{2}} \end{pmatrix} \tag{3.14}$$

$$I'_2 = \boldsymbol{E'_2}^{*}\boldsymbol{E'_2} = I'_0\,T_{Pol}\,T_x\,(cos^2\varphi'_{\lambda/4}\,cos^2\beta + sin^2\varphi'_{\lambda/4}\,sin^2\beta \; + \frac{1}{2}sin2\varphi'_{\lambda/4}\,sin2\beta\,sin\psi) \tag{3.15}$$

- When we use a combination of a halfwave plate rotated by ϖ with a phase retardation of $\varphi_{\lambda/2} = \pi + 2\gamma = 1.024\pi$ at the wavelength of emission ($\gamma \approx 2^{\mathrm{o}}$) and a polarizing beamsplitter cube with the transmittance of T_{Cub}, we obtain the beam emerging from the setup with the Jones vector $\boldsymbol{E'}_3 = \boldsymbol{J'}_3\,\boldsymbol{E}_{0_x}$ where the Jones matrix of the setup $\boldsymbol{J'}_3$ is given by Equation 3.6. We derive the intensity of this emerging beam as:

$$\begin{aligned} I'_3 &= \boldsymbol{E'_3}^{*}\boldsymbol{E'_3} \\ &= I'_0\,T_{Cub}\,T_x[cos^2\varphi'_{\lambda/4}(sin^2\gamma + cos^2\gamma\,cos^2\varpi) + sin^2\varphi'_{\lambda/4}\,cos^2\gamma\,sin^2\varpi \\ &\qquad + sin2\varphi'_{\lambda/4}\,cos\gamma\,sin2\varpi\,(sin\gamma\,cos\psi + cos\gamma\,cos2\varpi\,sin\psi)] \end{aligned} \tag{3.16}$$

When the state of the setup′s input is perfectly circularly polarized ($\delta_{in} = 0$, as observed

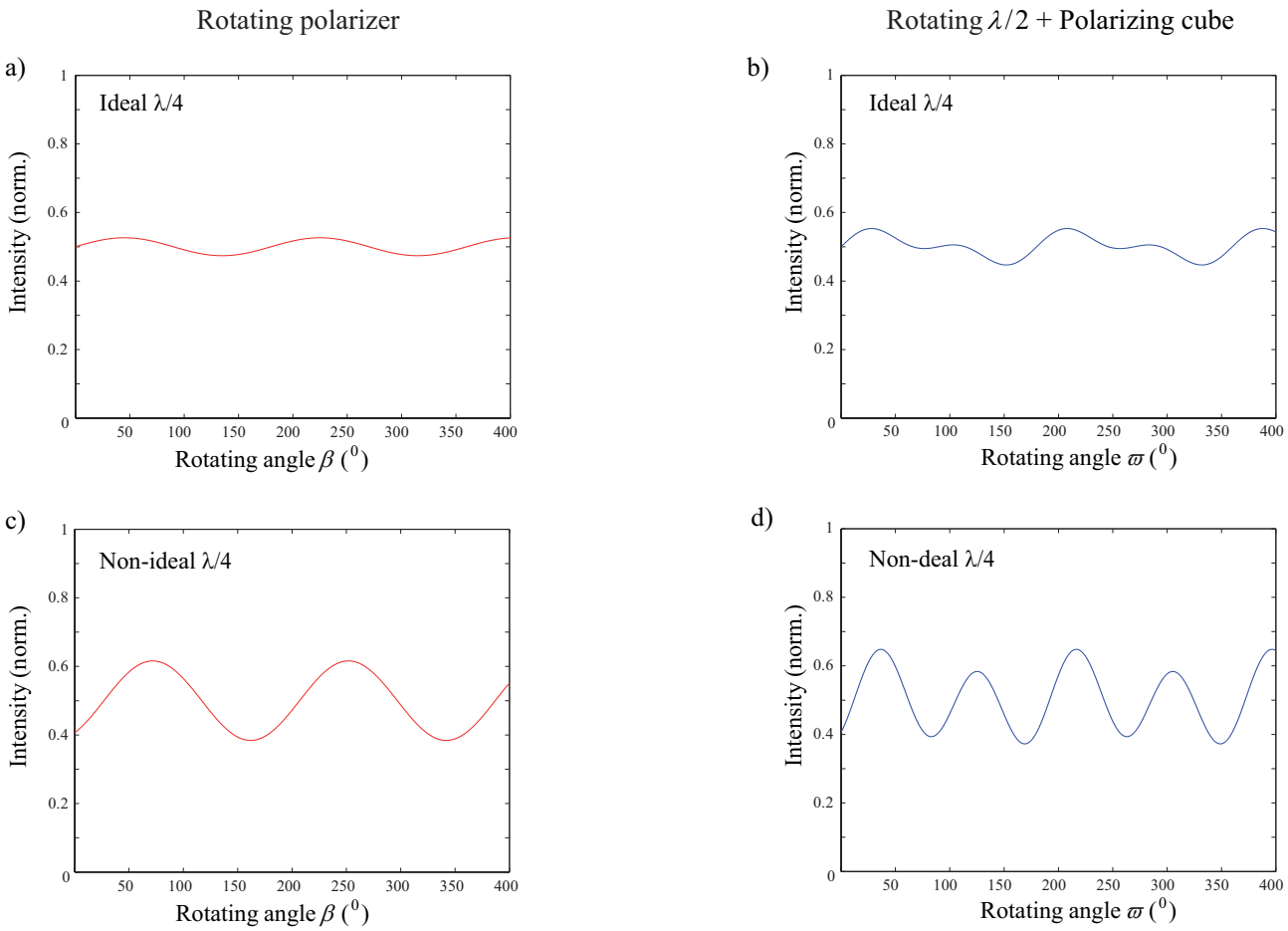

FIGURE 3.14: The simulating normalized intensity of the output when using 2 different setting way to obtain the signals: by a rotating polarizer (in red) and by a set of a rotating non-ideal halfwave plate (at the wavelength of emission $\gamma \approx 2^o$) followed by a polarizing beamsplitter cube (in blue) when the state of the beam entering the setup is perfect circularly polarization (a)/(b) or nearly circularly polarization (c)/(d) while rotations of the polarizer (β) and of the halfwave plate (ϖ) from 0^o to 400^o are performed. The retardation of the setup is $\psi = 8^o$.

in Figure 3.13(a)), the simulating normalized intensity of the beam exiting from the setup when it is analyzed by a rotating polarizer ($\frac{I'_2}{I'_0\,T_{Pol}\,T_x}$ from Equation 3.15) and by a rotating halfwave plate together with a polarizing beam splitter cube ($\frac{I'_3}{I'_0\,T_{Cub}\,T_x}$ from Equation 3.16) is plotted in Figure 3.14(a) and (b), respectively. The degree of polarization of the output in both case is $\delta_{out1} \approx \delta_{out2} \approx 0.04$, very close to the input value. The fact that it is not exactly 0 is because of the retardation induced by the setup ($\psi = 8^o$).

On the other hand, when we consider the non-ideal nature of the quarterwave plate, the beam entering the setup is nearly circularly polarized with $\delta_{in} \approx 0.2$, as observed in Figure 3.13(b). The degree of polarization of the calculating normalized intensity of the detected beam in both cases is $\delta_{out1} \approx \delta_{out2} \approx 0.2$, as presented in Figure 3.14(c) and (d). The agreement between the input and output values confirms the fact that **both detection ways is applicable for polarimetric measurements**.

However, beside the fact that the rotating angle β for one period of the polarizer P2 is 2 times ϖ of the halfwave plate, there is an obvious difference between two simulating curves: in the second case, the maximum/minimum values of the intensity varies in a periodic way. This difference may result from the fact that the halfwave plate is not ideal and therefore it is not equivalent in analyzing polarization state by a linear polarizer and by a halfwave plate followed by a polarizing cube. We will dicuss in the next subsection this interesting fact which only happens when the detection part consists of a rotating halfwave plate together with a polarizing beamsplitter cube.

3.2.3.3 The total polarization effect of the setup's dephasing ψ and the rotating non-ideal halfwave plate in the detection part

We focus on the fact that the detected signal is analyzed by a rotating halfwave plate followed by a polarizing beamsplitter cube in the followings. In order to characterize this periodic variation of the maximum/minimum values of the intensity, we consider the simulations of 4 relevant situations with different phase retardation of the setup ψ and different retardation of the halfwave plate $\varphi_{\lambda/2}$ in two cases: when the beam entering the setup is perfectly circularly polarized (the ideal case $\delta_{in} = 0$) and when it is not perfectly circularly polarized (the realistic case $\delta_{in} \approx 0.2$):

- a) The setup is ideal $\psi = 0$ and the halfwave plate is ideal $\varphi_{\lambda/2} = 180^0$
- b) The setup is non-ideal $\psi = 8^0$ and the halfwave plate is ideal $\varphi_{\lambda/2} = 180^0$

- c) The setup is ideal $\psi = 0$ and the halfwave plate is non-ideal $\varphi_{\lambda/2} = 184^0$
- d) The setup is non-ideal $\psi = 8^0$ and the halfwave plate is non-ideal $\varphi_{\lambda/2} = 184^0$

*** The ideal case: the input light is perfectly circularly polarized**

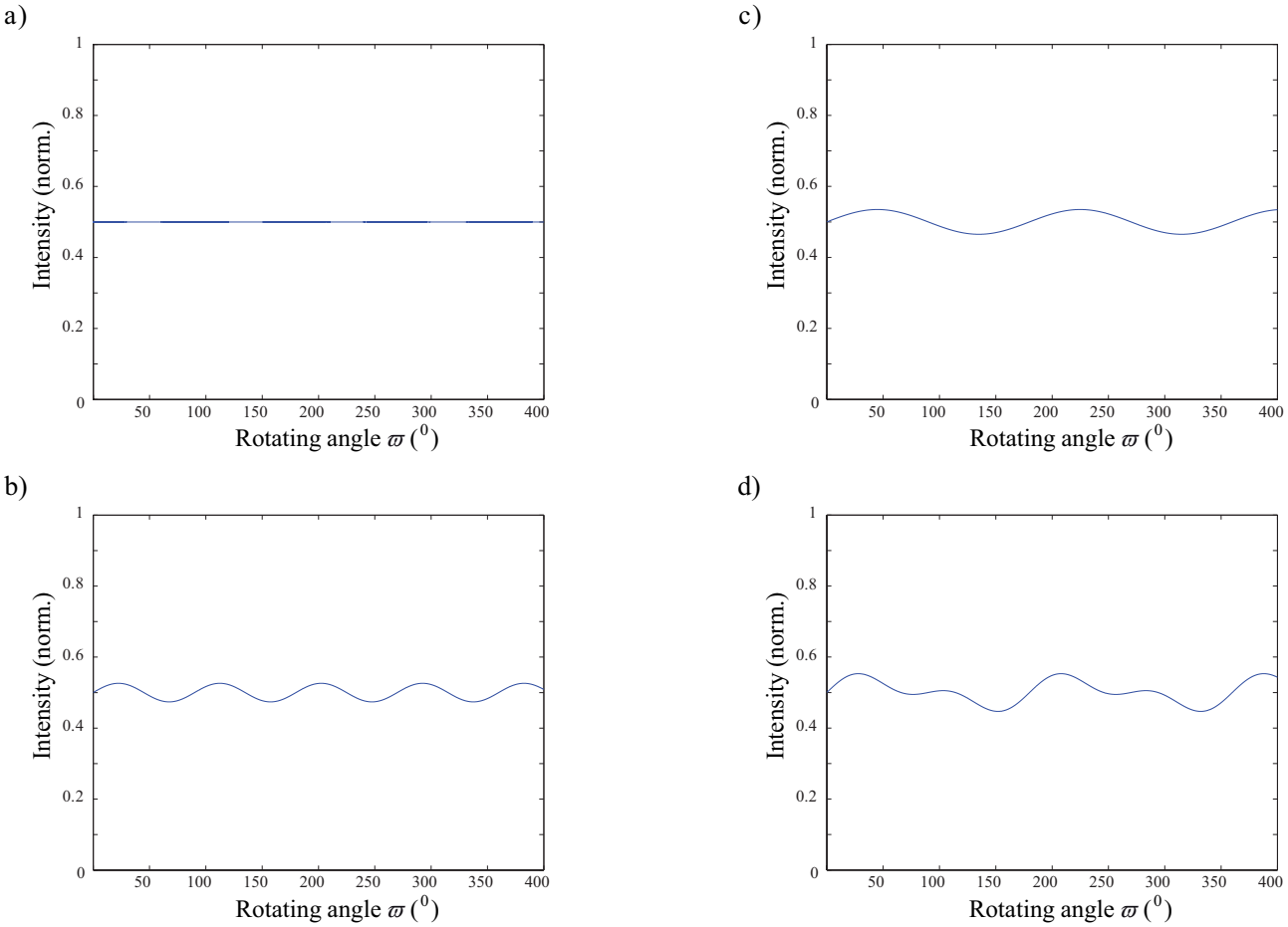

FIGURE 3.15: The simulating normalized intensity of the output analyzed by a set of a rotating halfwave plate followed by a polarizing beamsplitter cube with the beam entering the setup being perfectly circularly polarized ($\delta_{in} = 0$ from Figure 3.13(a)) when rotations from 0^o to 400^o of the halfwave plate are performed. The phase retardation ψ of the setup and different retardation of the halfwave plate $\varphi_{\lambda/2}$ are set as: (a) $\psi = 0$ and $\varphi_{\lambda/2} = 180^0$, (b) $\psi = 8^0$ and $\varphi_{\lambda/2} = 180^0$, (c) $\psi = 0$ and $\varphi_{\lambda/2} = 184^0$, (d) $\psi = 8^0$ and $\varphi_{\lambda/2} = 184^0$.

We report on the Figure 3.15 the calculating normalized intensity which is obtained when rotating the halfwave plate by $0^o < \varpi < 400^o$ for a perfectly circularly polarized light incident on the setup in 4 mentioned situations. The simulated curve representing the input$'$ signal is already discussed in Figure 3.13(a). We have:

- a) When the setup has no dephasing effect and the halfwave phate works ideally, the

beam exiting the setup is also perfectly circularly polarized $\delta_{out} = \delta_{in} = 0$, as shown in Figure 3.15(a).

- b) When there is a phase retardation of $\psi = 8^0$ introduced by the setup but the halfwave-plate remains being ideal, the signal oscillates with a period of 90^0, since the beam is analyzed by a rotating halfwave plate and a polarizing beamsplitter cube (Figure 3.15(a)). The degree of polarization of the output is $\delta_{out} = 0.04$, referring to a mostly perfectly circularly polarization state. It should be noted that the phase of the curve is slightly shifted comparing to the situation (a).

setup \ $\lambda/2$	ideal $\varphi_{\lambda/2} = 180^0$	non-ideal $\varphi_{\lambda/2} = 184^0$
ideal $\psi = 0$	(a) - $\delta_{out} = 0$ - Same as analyzing by a polarizer	(c) - $\delta_{out} = 0.04$ - Period of 180^0
non-ideal $\psi = 8^0$	(b) - $\delta_{out} = 0.04$ - Period of 90^0 - Phase shifted	(d) - $\delta_{out} = 0.04$ -Maximum and minimum values oscillate periodically of 180^0

FIGURE 3.16: Summary of the polarization state of the normalized intensity of the output analyzed by a set of a rotating halfwave plate followed by a polarizing beamsplitter cube with the beam entering the setup being perfectly circularly polarized ($\delta_{in} = 0$) for 4 simulated situations.

- c) We consider an ideal setup ($\psi = 0$), therefore, the transmitted beam is supposed to be perfectly circularly polarized. However, since the halfwave plate is non-ideal $\varphi_{\lambda/2} = 184^0$, the degree of polarization calculated for the output is $\delta_{out} = 0.04$. A complete period of the resulting curve is 180^0. It is explainable since the only element affects the phase in this situation is the imperfect halfwave plate.

- d) When both the setup and the halfwave plate are non-ideal with $\psi = 8^0$ and $\varphi_{\lambda/2} = 184^0$ respectively, the detected data vary with a period of 90^0 while the minimum and maximum values change with with a period of 180^0. The average degree of polarization δ_{out} keeps being 0.04.

Figure 3.16 presents a short summary of resulting polarization state of the perfectly circu-

larly polarized light after passing through the setup and being analyzed by a rotating halfwave plate in 4 simulated situations. The output is considered as perfectly circular polarized since the induced degree of polarization is within the range of measurement errors.

*** The realistic case: the input light is not perfectly circularly polarized**

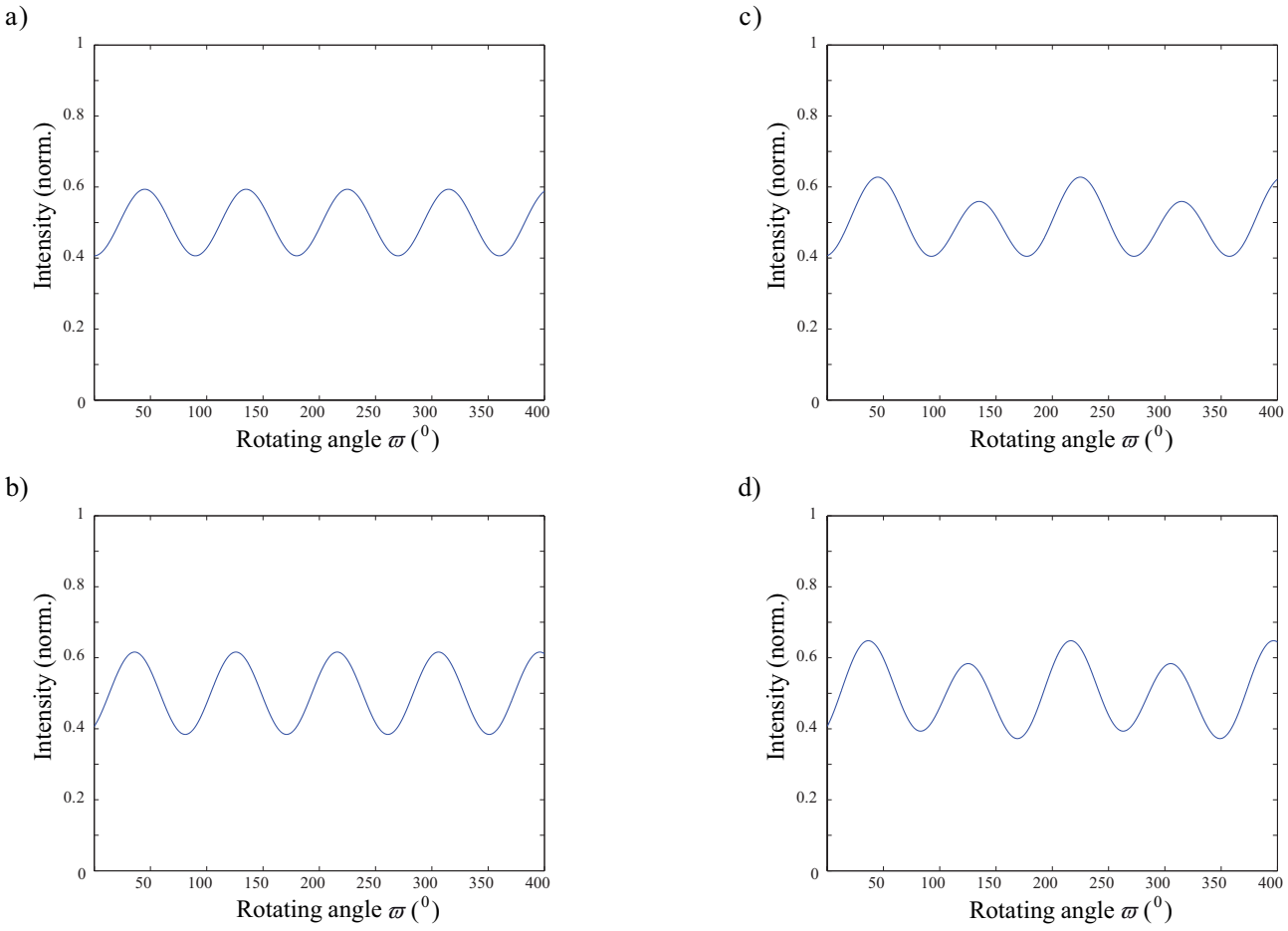

FIGURE 3.17: The simulating normalized intensity of the output analyzed by a set of a rotating halfwave plate followed by a polarizing beamsplitter cube with a nearly circularly polarized beam entering the setup ($\delta_{in} \approx 0.2$ from Figure 3.13(b)) when rotations from 0^o to 400^o of the halfwave plate are performed. The phase retardation ψ of the setup and different retardation of the halfwave plate $\varphi_{\lambda/2}$ are set as: (a) $\psi = 0$ and $\varphi_{\lambda/2} = 180^0$, (b) $\psi = 8^0$ and $\varphi_{\lambda/2} = 180^0$, (c) $\psi = 0$ and $\varphi_{\lambda/2} = 184^0$, (d) $\psi = 8^0$ and $\varphi_{\lambda/2} = 184^0$.

In the followings we discuss the realistic case when a nearly circularly polarized light enters the setup with $\delta_{in} \approx 0.2$, as presented in Figure 3.13(b). For all 4 simulated situations, the average degree of polarization δ_{out} keeps being 0.2 and the oscillating period of the curve is 90^0 as expected, but there is an obvious difference between these curves:

setup \ $\lambda/2$	ideal $\varphi_{\lambda/2} = 180^0$	non - ideal $\varphi_{\lambda/2} = 184^0$
ideal $\psi = 0$	(a) - $\delta_{out} = 0.2$ - Period of 90^0 - **Same** as analyzing by **a polarizer**	(b) - $\delta_{out} = 0.24$ - Period of 90^0 - **Minimum** values **remain**, **maximum** values **oscillate** periodically of 180^0
non-ideal $\psi = 8^0$	(c) - $\delta_{out} = 0.24$ - Period of 90^0 - **Phase shifted**	(d) - $\delta_{out} = 0.24$ - Period of 90^0 -**Minimum and maximum** values **oscillate** periodically of 180^0

FIGURE 3.18: Summary of the polarization state of the normalized intensity of the output analyzed by a set of a rotating halfwave plate followed by a polarizing beamsplitter cube with the beam entering the setup being nearly circularly polarized ($\delta_{in} \approx 0.2$) for 4 simulated situations.

- a) The ideal case when there are no retardation introduced by the whole system $\psi = 0$ and the output is analyzed by an ideal halfwave plate $\varphi_{\lambda/2} = 180^0$, the detected signal is the same to the result analyzed by rotating the analyzer P2, as described in Figure 3.17(a). We have $\delta_{in} = \delta_{out} = 0.2$

- b) While $\varphi_{\lambda/2} = 180^0$ but our setup induces a phase retardation of $\psi = 8^0$, we can observe the phase change of the intensity curves as seen in Figure 3.17(b): the first maximum peak is at $\varpi = 37^0$ instead of being at $\varpi = 45^0$ as obtained in Figure 3.17(a).

- c) We consider the non-ideal halfwave plate employed in our setup which has $\varphi_{\lambda/2} = 184^0$ [80]. When the setup has no retardation effect $\psi = 0$, only the maximum values of the intensity varies with a period double of the intensity values themselves while the minimum values remain the same, as shown in Figure 3.17(c).

- d) When the incident light is phase shifted after passing through the setup then the employed halfwave plate with a retardation of $\varphi_{\lambda/2} = 184^0$, both the maximum and minimum intensities changes periodically, as observed in Figure 3.17(d).

We summary the simulation results for 4 situations when the light entering the setup is nearly circularly polarized ($\delta_{in} \approx 0.2$) in Figure 3.18. It is confirmed that **the periodic**

deviation of the maximum or/and minimum values of the recorded intensity curve results from the fact that the halfwave plate used is imperfect.

3.2.4 Comparison between two detection ways

As summarized in Figure 3.19, there is a good agreement between two ways of analyzing the transmitted light: a rotating polarizer or a combination of a rotating halfwave plate and a polarizing beamsplitter cube, so that they are confirmed to be capable of replacing one by the other. Therefore, we will use the rotating halfwave plate followed by a fixed polarizing cube as planned.

Input	Output detected by a polarizer	Output detected by an non-ideal $\lambda/2$ and a polarizing cube
linearly polarized along 45^0 direction $\delta_{in} = 1$	- $\delta_{out} = 1$ - linearly polarized	- $\delta_{out} = 1$ - linearly polarized
perfectly circularly polarized $\delta_{in} = 0$	- $\delta_{out} = 0$ - perfectly circularly polarized	- $\delta_{out} = 0.04$ - mostly circularly polarized - oscillation of maximum and minimum values
nearly circularly polarized $\delta_{in} = 0.2$	- $\delta_{out} = 0.2$ - nearly circularly polarized	- $\delta_{out} = 0.24$ - nearly circularly polarized - oscillation of maximum and minimum values

FIGURE 3.19: Comparison between two detection ways: a rotating polarizer and a rotating non-ideal halfwave plate ($\varphi_{\lambda/2} = 184^0$) followed by a polarizing beamsplitter cube with three relevant polarization states of the incident beam and the dephasing of the setup $\psi = 8^0$.

3.2.5 Other determination of the retardation induced by the setup

In the realistic case, while detecting the output by a combination of a rotatable non-ideal halfwave plate and a polarizing beamsplitter cube, the oscillation of the minumum intensity

values only appears when there is a phase retardation ψ caused by the setup. It gives us an idea to characterize quantitatively ψ. Figure 3.20 depicts the difference between the periodic deviation of the minimum data calculated for three different values of ψ when the incident light is linearly polarized at 45° with respect to the x reference axis ($\delta_{in} = 1$).

We assume that the setup introduces no dephasing $\psi = 0$, then all the minimum value are exactly 0 (Figure 3.20 (a)). When there is a retardation induced by the setup, the minimum values no longer reach 0 and vary periodically of 180^0 depending on the ψ as described in Figure 3.20 (b) and (c). By comparing the experiment result with these simulated curves, we could estimate the phase shift induced by the experimental setup.

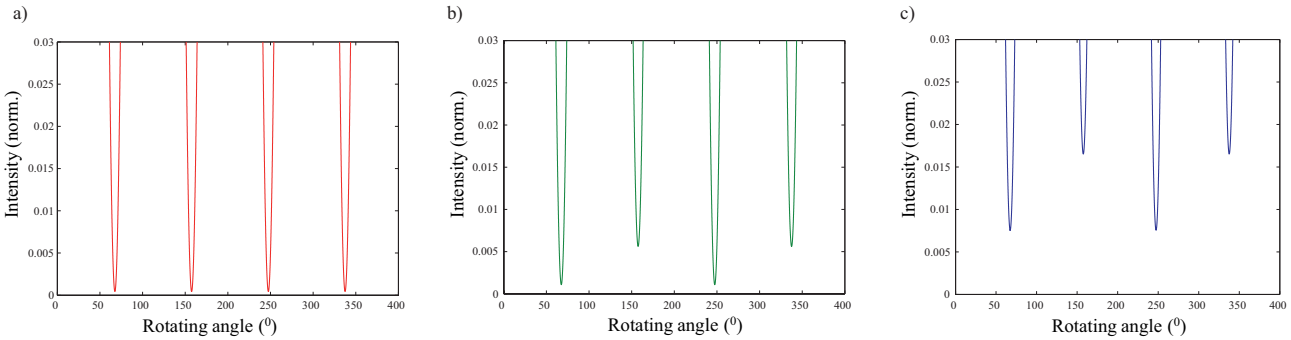

FIGURE 3.20: The minimum values of the normalized intensity of the output as the function of the rotating angle of the halfwave plate for a 45^o linearly polarized light (with respect to the x reference axis) incident on the setup calculated with different retardation introduced by the setup: (a) $\psi = 0$, (b) $\psi = 8^0$, and (c) $\psi = 16^0$. Noted that the halfwave plate is non-ideal $\varphi_{\lambda/2} = 184^0$.

3.3 Analysis of polarization property of the realistic experimental setup

We will use point-like emitters as the reference sample to finalize the setup calibrations. These emitters are spheres of polymer infiltrated with a high concentration of fluorescent molecules ($\lambda \sim 580 - 605nm$), commercialized by ThermoFisher. The diameter of each bead is typically 0.2 mm. Since we study photoluminescence from a single polymer microsphere which is much smaller than its emission wavelength, it is reasonable to treat it like a point like source. Each bead including many dye molecules randomly orientated, therefore, its emission is supposed to be isotropic in three dimensions with no preferential polarization in the homogenous media. So it could be considered as unpolarized emitters. The emission polarization measurements for several individual microspheres are performed in the setup schematized in Figure

3.21. We will perform the experimental measurements in order to compare to the simulation works discussed previously in the section 3.2. It should be noted that our employed quarterwave plate is non-ideal, we could not perform the case of a perfectly circularly polarized input.

3.3.1 Presentation of the realistic experimental setup

Figure 3.21 illustrates the experimental setup for the emission polarization measurement after diattenuation and retardation corrections. The photoluminescence incident on the second dichroic D2 and being reflected on the second prism (Prism 2) followed by a halfwave plate ($\lambda/2$). The halfwave plate is rotated around the direction of propagation (z axis) at a constant speed of $15^o/s$ by a motorized holder.

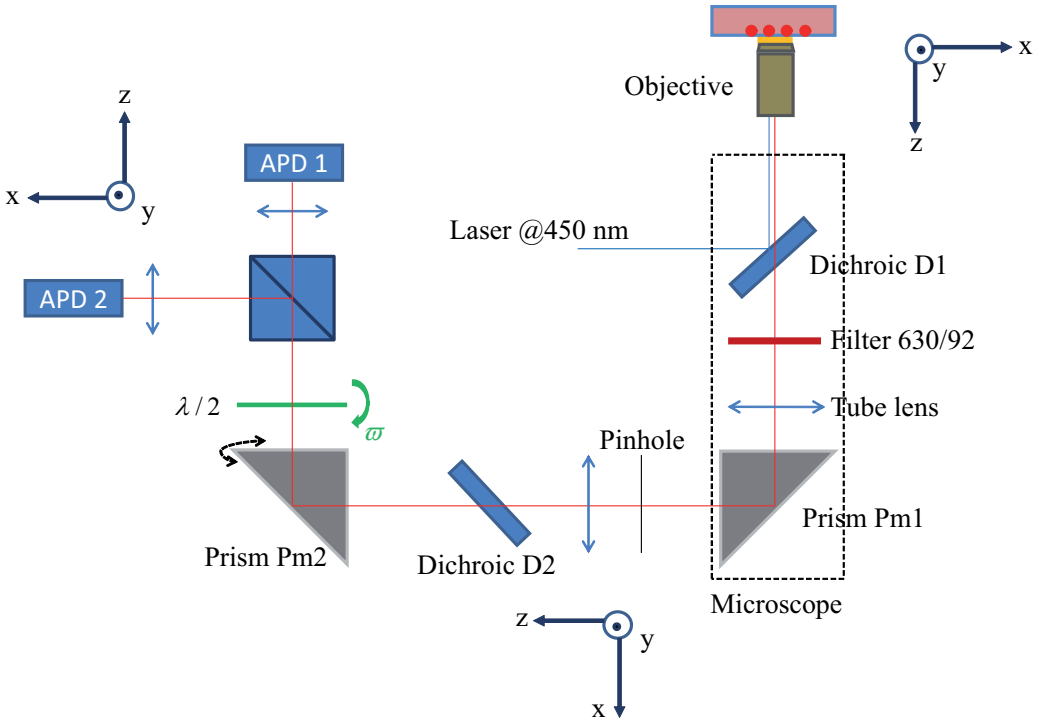

FIGURE 3.21: Schematic configuration of the final developed setup for emission polarization measurement. Noted that the z axis is always oriented in the direction of propagation.

The emission light is finally sent through a polarizing beamsplitter cube (PBS) which splits the signal into two orthogonal polarizations (along x and y directions). These two parts are then recorded by two separate single photo counting avalanche photodiode (APD). At our emission′ wavelength, the photoluminescence′ part arriving to the transmission APD is linearly horizontally polarized (x polarization) while the part reflecting on the cube consists of 95% vertical polarization and 5% horizontal polarization. Therefore, we only perform the polarimetric analysis on the collected data of the transmission APD. In order to remove the

influence of the fluctuations, these signals will be normalized by the total intensity obtained by both photodiodes $I_{norm_1}(\varpi) = \dfrac{I_1(\varpi)}{I_1(\varpi) + I_2(\varpi)}$.

The rotating halfwave plate followed by a polarizing beamsplitter cube works as a polarization anlayser: The halfwave plate is rotated by an angle of ϖ, changing the electric field E direction by 2ϖ while the polarizing beamsplitter cube transmits only the horizontal component of the photoluminescence. The laser, the pinhole, the avalanche photodiode, and the low concentration of the emitters on the sample$'$ surface will ensure that the detected signal is from the selected individual emitter.

3.3.2 The incident emitted light is unpolarized

Figure 3.22(a) displays the normalized intensity of the emission of an isolated molecular ball detected by each photodiode as a function of the rotating angle of the halfwave plate. The blue line is recorded by the transmission APD, while the green one is by the reflection APD. Each signal is normalized by the sum of the intensities collected by both photodiode in order to avoid errors due to fluctuations. The signal rarely changes, resulting in the degree of polarization $\delta = 0$. This result confirmed that **we send an unpolarized incident light through our experimental setup, the setup would not introduce any unexpected polarization effect**.

3.3.3 The incident emitted light is linearly polarized

We now turn our attention to the linearly polarized incident beam. A polarizer film was inserted between the objective and the first dichroic D1 in order to make the emission fully linear polarized (the degree of polarization $\delta_{in} = 1$). The corresponding output signals were presented in Figure 3.22(b), (c), and(d). When the axis of the polarizer film is set along along x and y direction (Figure 3.22(c) and (d) respectively), resulting in an incident linearly polarized light along x and y reference axes, the degree of polarization of the detected light (δ_{out}) still remains 1, which implies that the output light is still fully polarized. The difference between the estimated dipolar azimuthal angle $\Phi_c - \Phi_d$ obtained in two different incident polarization is also kept as 90^o. These two curves are antiphased, as expected. This estimated azimuthal angles gives us the reference angles indicating the horizontal and vertical axis of the setup($\Phi = -74^o$ corresponds to x axis and -164^o corresponds to y axis).

When the input light is polarized along -45^o direction to the reference axes (Figure 3.22b),

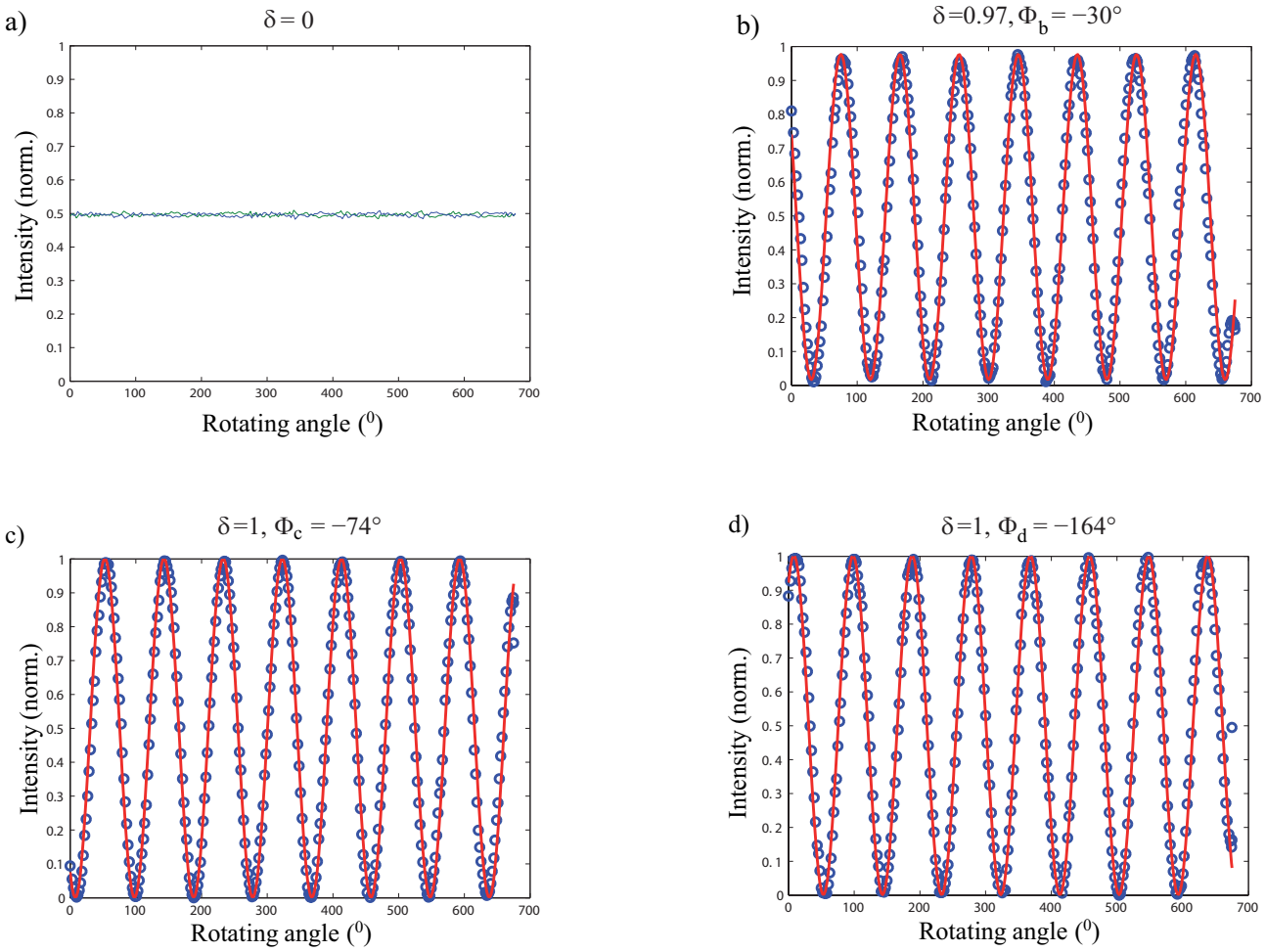

FIGURE 3.22: The normalized intensity as a function of the rotating angle of $\lambda/2$ when the input of the setup is the original emission of an individual microsphere (a), the part linearly polarized in the direction at -45^o to the x axis (b),the part linearly polarized along x axis (c), the part linearly polarized along y axis (d). Blue circles represent the experimental curve and Solid red line is the fitting of this curve with Equation 2.1.

the detected $\delta_{out} = 0.97$ and $\Phi_b = -30^o$. The value of this obtained azimuthal angle is in a good agreement with the reference angles ($\Phi_c - \Phi_b = -45^o$). By equation 2.43, the phase retardation of the setup could be calculated: $\psi = 8^o$, similar to the previous value obtained by the calibrating measurement using the incident collimated laser with a power meter as a detector and a rotating polarizer as an analyzer.

It is noticed in Figure 3.22(b) that the minimum/maximum values of the intensity varies in a periodic way, which has already been discussed when calculating the intensity of the transmitted light with the Jones vector given by Equation 3.16. Figure 3.23(a) zooms in the periodic variation of the minimum values of the output′ intensity plotted in Figure 3.22(b). This tiny periodic change is proven to result from the non-ideal behavior of the halfwave plate at the wavelength of emission ($630 - 650nm$). Comparing this experimental curve with the simulation works shown in Figure 3.20 for a linearly polarized beam entering the setup, we find out the retardation introduced by the setup is about $\psi = 8^o$, as observed in Figure 3.23. This phase retardation is the same with the values estimated from the equation 2.43, ensuring the accuracy of the determination of the setup′s phase retardation ψ.

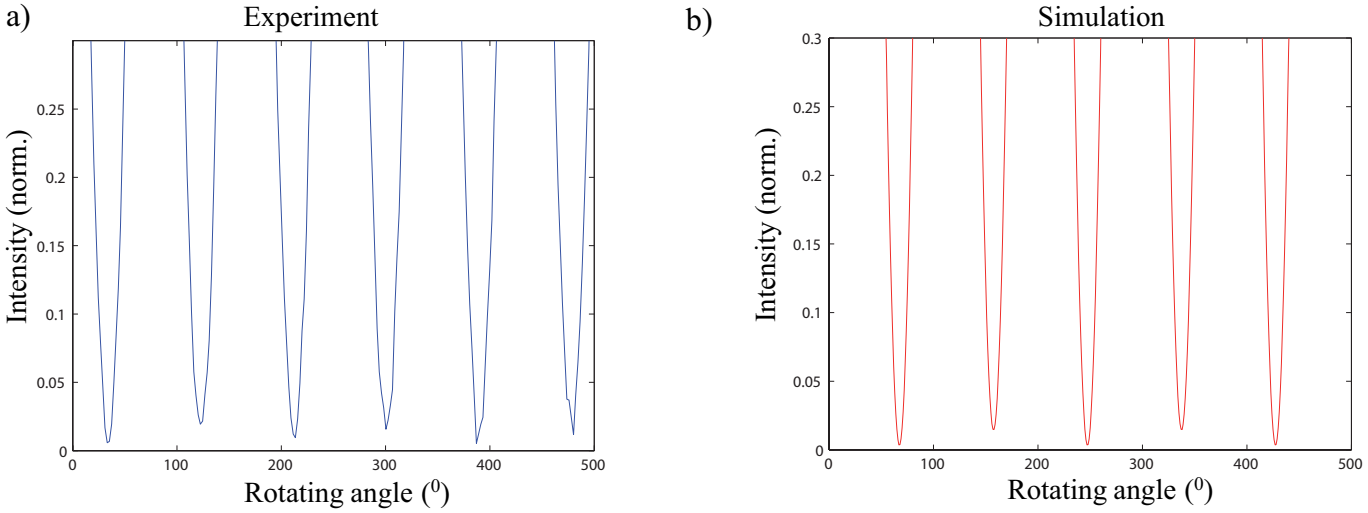

FIGURE 3.23: The normalized intensity of the output as the function of the rotating angle of the $\lambda/2$: the experimental curve (a) and the simulational curve for $\psi = 8^o$ and a retardation of $\varphi_{\lambda/2} = 184^o$ of the halfwave plate (b).

3.3.4 The incident emitted light is circularly polarized

We will continue by considering a circularly polarized light as the incident beam onto the setup. The emission is collected from an individual fluosphere ball, and its polarization state will be modified to be circularly polarized by setting the axis of the polarizer P1 along the x

axis of the setup ($\alpha = 0$) and turning the quarterwave plate′s fast axis 45° to the x axis. The polarization of the input of the setup are analyzed by the linear polarizer P2 inserted right after the quarterwave plate (before the setup) in the setup schematized in Figure 3.9. Then, the linear analyzer P2 is placed after the adding prism Pm2 (after the setup) to characterize the output of the setup.

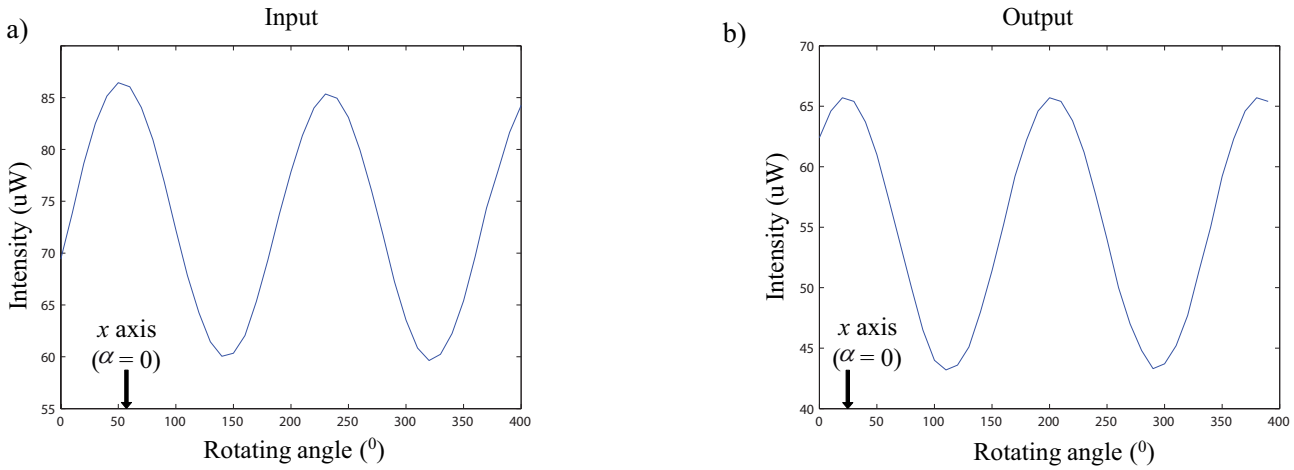

FIGURE 3.24: The intensity of (a) the input (analyzer P2 is inserted right after the quarterwave plate) and (b) the output (analyzer P2 is fixed after the additional prism Pm2) of the setup measured by the power meter in the final calibrating configuration shown in Figure 3.9 when rotating the analyzer. Noted that the rotating angles are just the numbers indicated on the mount of the polarizer analyzer P2: the x reference axis corresponds to 55^o and 25^o for the input and output case, respectively.

Figure 3.24 presents the intensity of the input and output of the setup measured by the power meter following the polarization analyzer P2, as described in Figure 3.9, when rotating the analyzer P2. The polarizer P1 is put at $\alpha = 0$, resulting in a linear horizontally polarized light incident on the quarterwave plate. Since the angle between the axes of the polarizer P1 and the quarterwave plate is 45°, the light entering the setup would theoretically be circularly polarized. However, in Figure 3.24 (a), the experimental result gives $\delta_{in} = 0.2$, reffering to an input of the setup being not perfectly circularly polarized. As discussed in the subsection 3.2.3), it is because the retardation of the quaterwave plate at the wavelength of 630nm is not strictly equal to $\pi/2$.

The output of the setup are therefore not perfectly circularly polarized, which is in agreement with Equation 3.15. The degree of polarization of the output is $\delta_{out} = 0.22$, leading to the retardation by the setup $\psi \approx 10^o$. We observe a good agreement between the experimental (Figure 3.24(a) and (b)) and the theoretical curves (Figure 3.13(b) and 3.14(c)). The degree of polarization is not much affected by the small retardation induced by the setup ($0 < \psi < 10^o$).

Therefore, it confirms the working capability of our final developed setup for analyzing polarization of the emission. To conclude, **the setup schematized in Figure 3.21 is applicable for polarimetric measurements since it introduces a very slight change in the state of polarization**.

Conclusion

We develop in this chapter the emission polarization measurement in order to study the nanoemitters′ dipolar dimensionality and its associated orientation at individual scale. The microscopy setup is checked in term of diattenuation and retardation, respectively. We have systematically analyzed and discussed the polarization effects introduced by the setup. After inserting an additional dichroic and prism, the setup is confirmed to induce a smallest effect on the polarization state of a transmitted beam. It can be concluded that our experimental setup will only modify less than 4% of the emission′s degree of polarization, which does not influence on the resulting determination of the orientation of the nanoemitter′ emitting dipole.

Chapter 4

Emission pattern measurement and analysis

Introduction

The angular intensity distribution, so-called emission pattern, is an important property of the photoluminescence from nanoemitters. The emission pattern depends on not only the nanoemitter′s dipolar dimensionality and its dipolar orientation, but also on the local optical environment around it. Therefore, it is possible to gather information on the orientation of the emitting dipole from emission pattern measurements.

Nowadays, most single molecule experiments are performed in or near planarly layered media. The photons emitted from an invidual emitter can scatter at the interface, resulting in an alteration of its emission pattern. Dipole emission near planar interfaces has gained great interest in many theoretical studies, especially in antenna theory and integrated optics [63, 64, 82–92]. Sommerfeld developed a theory for a vertically oriented dipole in 1909 [83]. In 1911, the horizontal dipole was investigated by Horschelmann [84, 86]. Later, in 1919, Weyl expanded the problem by a superposition of plane and evanescent waves [85]. A lot of other researchers have similarly approached the topic, all based on the Sommerfeld′s lectures [87–89]. The emission patterns were experimentally obtained in 1987 for an ensemble of molecules with their averaged dipolar orientation [93].

The emission pattern provides another method for studying the emission. It allows to estimate the ambiguity in polarimetric measurements. For example, a given value of the degree of polarization δ gives two possible dipolar orientation depending on the 1D or 2D dipolar

dimensionality. This chapter starts by introducing the principles of the emission pattern measurement. After summrizing the main developed theoretical basis of simulating the emission pattern, the experimental setup will be presented. We also discuss the calibrating procedures needed to optimize the setup. Finally, we will explain our way to analyze the measured emission pattern.

4.1 Principles of the measurement

The emission pattern defines the distribution of the power radiated from a dipole as a function of the direction away from it. For example, the 3-dimensional radiation pattern of a dipole oriented along z axis in free space is pictured in Figure 4.1. It has a doughnut type shape, with the axis of the dipole (z axis) passing through the hole at the centre of the doughnut. In the $x-y$ plane (perpendicular to the z axis), the radiation is maximum. The radiation falls to zero along the dipolar axis.

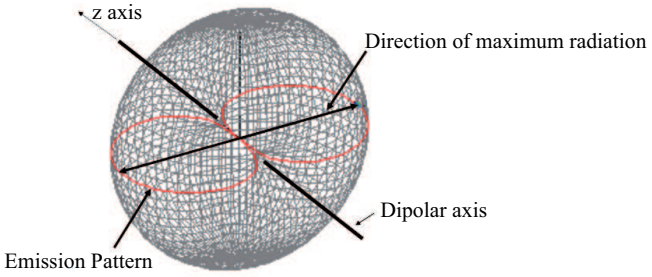

FIGURE 4.1: Theoretical emission pattern for a dipole in free space [94].

Typically, since it is simpler, the radiation patterns are plotted in 2-dimensional plane. In this case, the patterns are given as "slices" through the 3-dimensional diagram. The same pattern in Figure 4.1 is plotted in Figure 4.2(a). It appears like a figure-of-eight with the color corresponds to the magnitude of the power in this direction.

We consider the situation displayed in Figure 4.2 where a dipole with different orientations is in free space and above the glass substrate respectively. When the dipole is in free space, the emission pattern is a familiar figure-of-eight which is symmetric around the axis normal to the dipolar axis. When the distance of the dipole from the surface of the substrate is less than one wavelength, the dipole interacts with the local structure and radiate different form of emission. Consequently, the emission pattern loses its symmetry. There is a clear difference between the case of a dipole oriented along the substrate′s surface and of a dipole with its axis

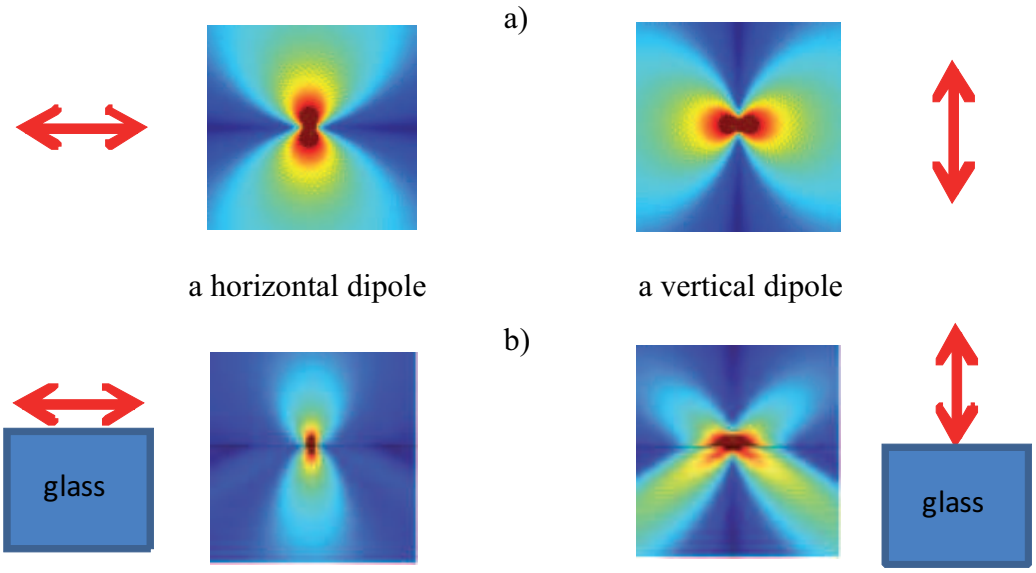

FIGURE 4.2: Field distribution for a horizontal dipole and a vertical dipole when (a) the dipole is in free space and (b) when the dipole is in air at a distance of 50 nm to the glass substrate.

perpendicular to this surface. For a fixed orientation of the emitting dipole at a fixed distance to a given layered substrate, a certain emission pattern could be simulated. By comparing the predicted emission pattern and the measured one, we could determine the orientation of the emitter.

4.2 Method to calculate the emission pattern

As the magnetic field is transverse to the electric field vector in the far field, the time averaged Poynting vector is derived as:

$$\vec{S} = \frac{1}{2}\mathbf{Re}\{\vec{E} \times \vec{H}^*\} = \frac{1}{2}\sqrt{\frac{\varepsilon_0 \varepsilon_j}{\mu_0 \mu_j}}\vec{E} \cdot \vec{E}^* \vec{e_r} \tag{4.1}$$

with $\vec{e_r}$ is the unit vector along the emitting direction. The power of the emission per unit solid angle $d\Omega = sin(\theta)d\theta d\phi$ is given by:

$$dP = P(\Omega)d\Omega = r^2 \vec{S} \cdot \vec{e_r} sin(\theta)d\theta d\phi \tag{4.2}$$

where $P(\Omega) = P(\theta, \phi)$ is defined as the emission pattern [79]. In short, it is a plot describing the relative far field strength $|\ \boldsymbol{E}\ |^2$ versus the angular direction (θ, ϕ) at a fixed distance from a dipole, with θ being the angle to the dipolar axis and ϕ denoting the azimuthal angle around this axis in the Fourier plane.

The existence of a surface in the vicinity of a dipole modifies its emission pattern. We develop the calculation for the angular distribution of the emitted power from a dipole oriented at (Θ, Φ) based on the works done by Lukosz [63, 64]. His calculations are expanded and simplified for the case of only one interface is taken into account. These studies are already published in the thesis and paper of Lethiec [27,52,62]. I will just summarize the main equations.

4.2.1 Reflection configuration

The typical example of the reflection configuration is that the emitter in a medium with higher refractive index, so that its emission is reflected at the interface, as illustrated in Figure 4.3. The objective directly collects the emitting beam at the angle of θ_1 with respect to the optical axis and at $\pi - \theta_1$ for the reflecting beam.

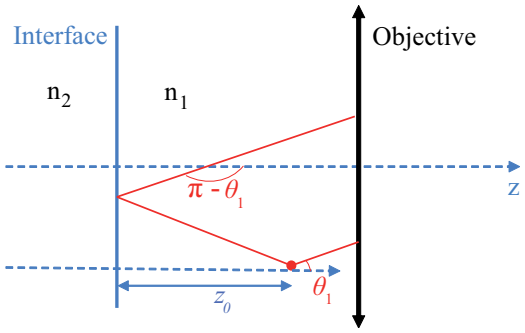

FIGURE 4.3: Schematic of the reflection configuration: an emitter situated in a medium with a refractive index of n_1 at a distance of z_0 to an interface with the other medium having index n_2 when $n_2 < n_1$ [27].

In optics, Fresnel's equations describe the reflection and transmission of electromagnetic waves at an interface. The reflection coefficients for waves perpendicular and parallel to the plane of incidence (s and p polarization respectively) are given by:

$$r_s = \frac{n_1 \cos\theta_1 - n_2 \cos\theta_2}{n_1 \cos\theta_1 + n_2 \cos\theta_2} \tag{4.3}$$

$$r_p = \frac{n_2 \cos\theta_1 - n_1 \cos\theta_2}{n_1 \cos\theta_2 + n_2 \cos\theta_1} \tag{4.4}$$

The emission pattern obtained by the objective will be distributed spatially with $\theta_1 \in [0, \pi/2]$ and $\phi \in [0, 2\,\pi]$ as:

$$P(\theta_1, \phi) = P_s(\theta_1, \phi) + P_p(\theta_1, \phi) \tag{4.5}$$

with P_s and P_p being the emitted power for s and p polarized light given respectively as:

$$P_s(\theta_1, \phi) = \frac{3}{8\pi} \mid \sin\Theta \sin(\Phi - \phi)\,(1 + r_s\, e^{2\,i\,k_z\,z_0})\mid^2 \tag{4.6}$$

$$P_p(\theta_1, \phi) = \frac{3}{8\pi} \mid \cos\Theta \sin\theta_1\,(1 + r_p\, e^{2\,i\,k_z\,z_0}) - \sin\Theta \cos(\Phi - \phi) \cos\theta_1\,(1 - r_p\, e^{2\,i\,k_z\,z_0})\mid^2 \tag{4.7}$$

and $k_z = \dfrac{2\,\pi}{\lambda}\, n_1 \cos\theta_1$ while z_0 denoting the distance between the emitter and the interface.

4.2.2 Transmission configuration

We consider a situation where the photoluminescence observed in a medium with the infractive index of n_2 is emitted by a dipole in a medium with the index of n_1. Therefore, the emission is collected by the objective at the angle of θ_2 with respect to the optical axis of the setup.

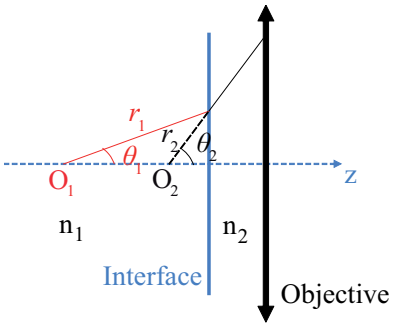

FIGURE 4.4: Schematic of a transmission configuration: an emitter situated in a medium with a refractive index of n_1 near an interface with the collecting medium with index n_2 when $n_2 < n_1$ [27].

i) Case $n_2 < n_1$

The simpler case is when $n_2 < n_1$, as illustrated in Figure 4.4. O_1 presents the position of the dipole emitter, the emission ray propagates along the direction at the angle θ_1 with respect to the z axis normal to the interface. The second medium will bend the incoming ray to the direction at the angle θ_2 to the z axis. The position O_2 corresponds to an imaginary position where the dipole would be located to emit the ray at the same angle θ_2 in the case the interface did not exist. Based on the geometric construction, the following relationship is obtained:

$$\frac{r_2}{r_1} = \frac{\sin\theta_1}{\sin\theta_2} = \frac{n_2}{n_1} \tag{4.8}$$

Thus the angle θ_2 varies from 0 to $\pi/2$ in the collecting medium. The Snell′s law indicates that the angle θ_1 is limited between 0 and $\arcsin \frac{n_2}{n_1}$.

The Fresnel′s transmission coefficients for s and p polarization are written as:

$$t_s = \frac{2\, n_1\, \cos\theta_1}{n_1\, \cos\theta_1 + n_2\, \cos\theta_2} \tag{4.9}$$

$$t_p = \frac{2\, n_1\, \cos\theta_1}{n_1\, \cos\theta_2 + n_2\, \cos\theta_1} \tag{4.10}$$

As discussed by Lukosz in [64] for a dipole with a given orientation of (Θ, Φ), Equation 4.2 will be expanded and simplified to yield the angular normalized power of s polarized light as:

$$P_s(\theta_2, \phi) = \frac{3}{8\pi}(\frac{n_2}{n_1})^3(\frac{\cos\theta_2}{\cos\theta_1})^2(\sin\Theta\, \sin(\Phi - \phi)\, t_s)^2 \tag{4.11}$$

and for p polarized light:

$$P_p(\theta_2, \phi) = \frac{3}{8\pi}(\frac{n_2}{n_1})^3(\frac{\cos\theta_2}{\cos\theta_1})^2(\cos\Theta\, \sin\theta_1\, t_p - \sin\Theta\, \cos(\Phi - \phi)\, \cos\theta_1\, t_p)^2 \tag{4.12}$$

with θ_1 lies between 0 and $\arcsin \frac{n_2}{n_1}$.

The emission pattern is thus written as:

$$P(\theta_2, \phi) = P_s(\theta_2, \phi) + P_p(\theta_2, \phi) \tag{4.13}$$

where θ_2 varies from 0 to $\pi/2$ and ϕ varies from 0 to $2\,\pi$ for the situation in which the emission propagates from the denser medium to another $n_1 > n_2$.

ii) Case $n_1 < n_2$

We move on to the more complex case when the emission travels to the denser medium ($n_1 < n_2$). The propagating waves in the medium 1 are deflected in the medium 2 with an angle of θ_2 which is $0 \leq \theta_2 \leq \theta_c$ where θ_c is the critical angle of the total internal reflection:

$$\theta_c = \arcsin n_1/n_2 \tag{4.14}$$

Some of the evanescent waves in the dipole's near field are refracted at the interface and appear in the collecting medium as plane waves with angles of refraction $\theta_2 > \theta_c$, so that θ_2

ranges from θ_c to $\pi/2$. In this regime we rewrite for the radiation pattern of an electric dipole due to its evanescent component of emission as:

$$P'_s(\theta_2, \phi) = f_s \, (\sin \Theta)^2 \, (\sin(\Phi - \phi))^2 \tag{4.15}$$

with

$$f_s = \frac{3}{2\pi} \, \frac{{n_2}^3}{n_1 \, ({n_2}^2 - {n_1}^2) \, \cos^2 \theta_2 \, e^{-2z_0/\Delta}} \tag{4.16}$$

where z_0 is the distance between the dipole and the interface while Δ is the penetration depth of the evanescent wave generated by the dipole in the medium with index n_1 given by:

$$\Delta = \frac{\lambda}{2\pi} \, ({n_2}^2 \, \sin^2 \theta_2 - {n_2}^2)^{1/2} \tag{4.17}$$

and

$$P'_p(\theta_2, \phi) = f_p \, (\cos^2 \Theta \, \sin^2 \theta_2 (\frac{n_2}{n_1})^2 + \sin^2 \Theta \, \cos^2(\Phi - \phi) \, ((\frac{n_2}{n_1})^2 - 1) \tag{4.18}$$

with

$$f_p = \frac{f_s \, {n_1}^2}{({n_2}^2 + {n_1}^2) \sin^2 \theta_2 - {n_1}^2} \tag{4.19}$$

Therefore, when $z_0 < \Delta$, evanescent component of the dipole$'$ emission in the medium 1 are transmitted to the medium 2 and become propagative. This energy is converted into propagating fields which travel beyond the critical angle θ_c. The angular distribution of the power $P'(\theta_2, \phi)$ when the light passes through the interface from the lower index medium to a higher one ($n_1 < n_2$) is expressed as:

$$P'(\theta_2, \phi) = P_s(\theta_2, \phi) + P_p(\theta_2, \phi) \tag{4.20}$$

where θ_2 varies from 0 to θ_c and

$$P'(\theta_2, \phi) = P'_s(\theta_2, \phi) + P'_p(\theta_2, \phi) \tag{4.21}$$

where θ_2 varies from θ_c to $\pi/2$ while ϕ varies from 0 to $2\,\pi$ for both cases.

For example, the diagram of the isotropic emission from a dipole in air at the air-glass interface is presented in Figure 4.5. In this situation, the medium 1 is air ($n_1 = 1$) while the collecting medium has $n_2 = 1.51$, therefore, the critical angle of the total internal reflection $\theta_c = 41.5^{\text{o}}$. The rays emitting at an angle $\theta_2 \leq 42^{\text{o}}$ correspond to an undercritical angle component of the collected emission (in blue). As the emitter is at the optical interface, some

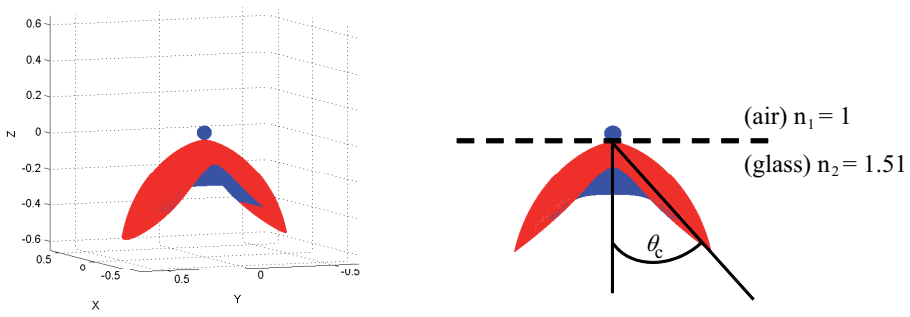

FIGURE 4.5: Simulated emission diagram of an isotropic emitter in air located at the air-glass interface with $\theta_c = 41.5^o$.

deflected rays propagate in the direction beyond the critical angle, corresponding to evanescent component of the emission (in red).

4.3 Method to measure the emission pattern

For a macroscopic sample, such as a LED, the goniometer is a practical device for analyzing the angular dependent distribution of radiation. It allows to change the direction at which a detector (often being an optical fiber) observes the sample. In the experiment, either the sample is moved around the detector at a fixed position or the detector is turned around the stationary sample. In both cases, each output for each rotating angles is detected when rotations from 0^o to 180^o are performed. The emitted intensity from different direction is recorded, and then used to reconstruct the angular intensity distribution of the radiated beam in one plane [79]. Since moving the detector is time and cost consuming, rotating the sample is more popular.

However, when the sample′ size is reduced to microscopic scale, either rotating a microscope′s objective around the emitters or moving the sample holder around the objective is clearly unpractical and unrealistic. In order to study the emission pattern of an nanoemitter, it is more applicable to collect all emission photons with the objective and then to image the intensity distribution in back(rear) focal plane, where the electric field is directly related to the Fourier transform (k-space distribution) of the field in the object plane (before the objective). This technique is thus named Back focal plane imaging [95–97].

In optics, the focal length of a lens is defined as the distance from the lens center to a point on the optical axis where parallel rays are focused (so-called a principal focal point). An imaginary plane perpendicular to the optical axis at this point is termed the focal plane of the

lens. Every lens has two principal focal points for receiving light, one at each side. Therefore, the focal plane in front of the objective is known as the front focal plane while the focal plane behind the objective is called the back/rear focal plane. The actual position of the back focal plane varies with the objective construction, but is generally situated somewhere inside the objective itself for high magnification ones [79].

Rays leaving the object with the same angle will meet in the objective's back focal plane. We start by considering an emitting dipole located in the front focal plane $z = 0$. Following the discussion in [96], the electric field of the dipole can be expressed as a function of Fourier transform $\hat{\vec{E}}$ by

$$\vec{E}(x, y; z = 0) = \iint_{-\infty}^{+\infty} \hat{\vec{E}}(k_x, k_y; z = 0) e^{i[k_x x + k_y y]} dk_x dk_y \tag{4.22}$$

The emission pattern is created by the field emitted along a direction of unit vector $\vec{u}$, at a distance $r \gg \lambda$ (far-field emission). We define the wavevector $\vec{k} = k\vec{u} = \frac{2\pi}{\lambda}\vec{u}$ with $\vec{k_{\|}}$ denoting its component in the cross section (x,y) and k_z denoting z-component.

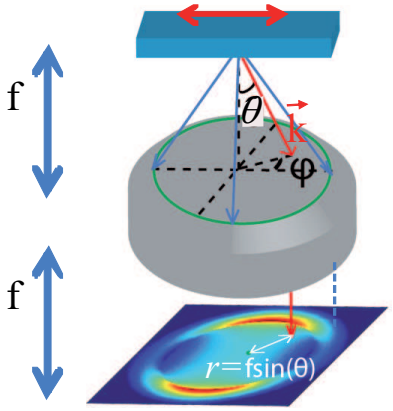

FIGURE 4.6: Coordinate system used where $\vec{k}$ is the wavevector [98].

Each point on the object plane in the front of the objective (x, y) is mapped into its reciprocal (k_x, k_y) on the back focal plane which can be assigned to an collecting angle (θ, ϕ) by:

$$\frac{k_{\|}}{|\vec{k}|} = \frac{\sqrt{{k_x}^2 + {k_y}^2}}{|\vec{k}|} = \sin\theta \tag{4.23}$$

and

$$\frac{k_y}{k_x} = \tan\phi \tag{4.24}$$

where θ is the angle to the optical axis ($\theta = 0$ along the axis) and ϕ is the angle around that

axis, as observed in Figure 4.6.

In addition, as seen in Figure 4.6, the distance between the dipole and the center of the objective is equal to the focal length f of the objective. The ray emitting from the dipole at the angle θ is refracted at the reference sphere of the objective and then directed onto the back focal plane. Thanks to the Abbe sin condition when the objective is considered as an ideal lens with no aberration, the radius coordinate r from the optical axis on the back focal plane is related to the emission angle by:

$$r = f\ \sin\theta \tag{4.25}$$

Therefore,

$$k_x = r\ \cos\phi = f\ \sin\theta\ \cos\phi \tag{4.26}$$

$$k_y = r\ \sin\phi = f\ \sin\theta\ \sin\phi \tag{4.27}$$

The power of the emission per unit solid angle $d\Omega = sin(\theta)d\theta d\phi$ is already given by Equation 4.2 :

$$dP = P(\Omega)d\Omega$$

where $P(\Omega) = P(\theta, \phi)$ is defined as the emission pattern [79]. The distribution of the emitted power on the back focal plane $\wp(k_\parallel)$ is related to the angular power density $P(\theta)$ as:

$$\begin{aligned}\wp(k_\parallel, \phi)\, k_\parallel\, dk_\parallel\, d\phi &= \wp(k_\parallel, \phi)\, (\mid \vec{k} \mid \sin\theta)\, d(\mid \vec{k} \mid \sin\theta)\, d\phi \\ &= \mid \vec{k} \mid^2\ \wp(k_\parallel, \phi)\ \cos\theta\ \sin\theta\, d\theta\, d\phi \\ &= \mid \vec{k} \mid^2\ \wp(k_\parallel, \phi)\ \cos\theta\, d\Omega\end{aligned} \tag{4.28}$$

Hence, we have:

$$P(\theta)\, d\Omega = \mid \vec{k} \mid^2\ \wp(k_\parallel, \phi)\ \cos\theta\, d\Omega \tag{4.29}$$

where Ω is the solid angle.

Therefore, the emission pattern is related to the power per unit solid angle obtained on the back focal plane by:

$$P(\theta) = \mid \vec{k} \mid^2\ \wp(k_x, k_y)\ \cos\theta \tag{4.30}$$

with k_x and k_y taken from Equation 4.26 and 4.27, respectively.

Equation 4.30 ensures that in the back focal plane (corresponding to the Fourier plane), the light intensity distribution contains information on the directions of emission of the dipole. The

cosine factor is an apodization factor which help to conserve the energy along each geometric path [94].

4.4 Experimental setup to measure the emission pattern

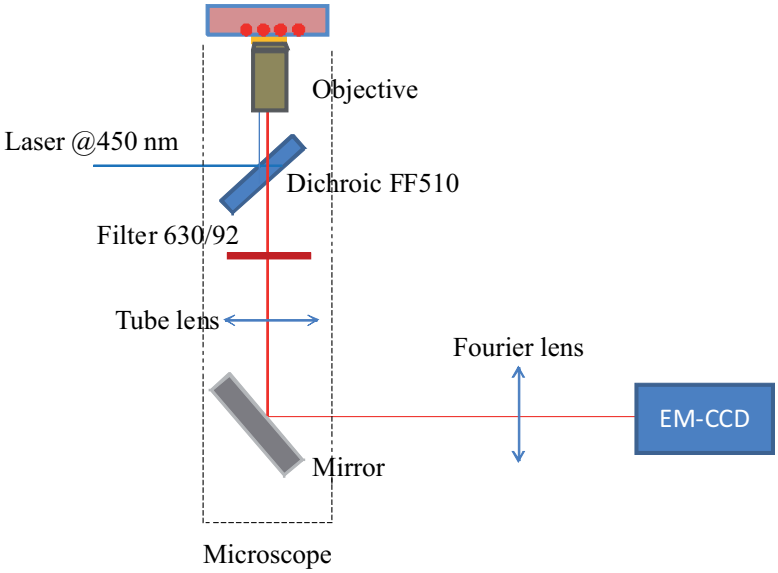

FIGURE 4.7: Schematic configuration of emission pattern measurement.

The emission pattern imaging is performed together with the emission polarization analysis for the same selected individual emitter, therefore, the excitation part of the setup is already described in subsection 2.2.1.

Since the actual position of the back focal plane is generally situated at the back pupil of the objective, in order to measure the emission pattern on this plane, we need to conjugate it to an imaging system. Here, we experimentally perform the emision pattern measurement by inserting a lens (often known as a Fourier lens) at the side port of the microscope. Thanks to the configuration of the tube lens and the Fourier lens, the emission pattern image will be projected onto the detector area of a cooled EM-CCD camera, as shown in Figure 4.7.

EM-CCD stands for Electron Multiplying Charge Coupled Device, a quantitative digital camera technology that is capable of detecting single photon events while maintaining high quantum efficiency, achievable by an unique electron multiplying structure built into the sensor. Unlike a conventional CCD, an EM-CCD is not limited by the readout noise of the output amplifier. Therefore, it brings an significant improvement to the signal to noise ratio, an important parameter when the recorded intensity signals are not high enough as in our case.

Thanks to the Fourier transform properties of the lenses, it is possible for an EM-CCD to map the angular emission pattern in the back focal plane.

In order to maximize the angular range of the measurements, the numerical aperture of the objective should be as large as possible. Thus we employ an oil immersion objective with a numerical aperture of 1.4. In a medium of refractive index n, the numerical aperture is given by :

$$NA = n\, sin\theta_{max} \tag{4.31}$$

where θ_{max} is the maximum collection angle. The numerical aperture is mostly used to describe the capability of gathering light of an objective. The larger it is, the more flux is collected. Since the employed objective uses immersion oil with a refractive index of 1.52, which leads to a maximum collection angle θ of 67°.

The position of the Fourier lens is set with the help of a He-Ne laser. We send the collimated laser into the objective from the sample side along its optical axis, so that the laser will be focused on the back focal plane (Fourier plane). We slightly move the Fourier lens in order to get the laser spot on the EM-CCD detector area as small as possible to validate the conjugation. By adjusting the position of Fourier lens and the EM-CCD, a clear image of the objective′s back aperture plane would be recorded.

4.5 Setup calibrations

In order to confirm that the Fourier plane is well conjugated to the EM-CCD sensor, we profits the situation that the emitter is deposited on a glass surface. Figure 4.8(a) presents the emission pattern on the Fourier plane directly imaged by an EM-CCD camera and an oil immersion objective. The emission radiated from point-like emitters on a glass substrate (coverslip). These emitters are microspheres (about 200μm diameter) containing a high concentration of dye polymer fluorescent molecules at the wavelength of 580-605 nm from ThermoFisher. As these molecules are randomly oriented, the microspheres are believed to emit isotropically with no prefered direction.

The photoluminescence of an emitter into the solid angle collected by the microscope objective appears as a thin ring in the Fourier image, as seen in Figure 4.8(a). The emission in a certain direction is directed to an unique point on the back focal plane of the objective (Fourier plane). Therefore, each point in the Fourier plane represents a unique set of polar and azimuthal angles (θ, ϕ) of the emission, corresponding to one observation direction (θ is

the angle to the optical axis and ϕ is the angle around that axis, as illustrated in Figure 4.6). For example, a spot located at the edge of the Fourier image represents the emission at a large angle, given by the numerical aperture of the objective. The center of the image corresponds to the emission normal to the sample surface.

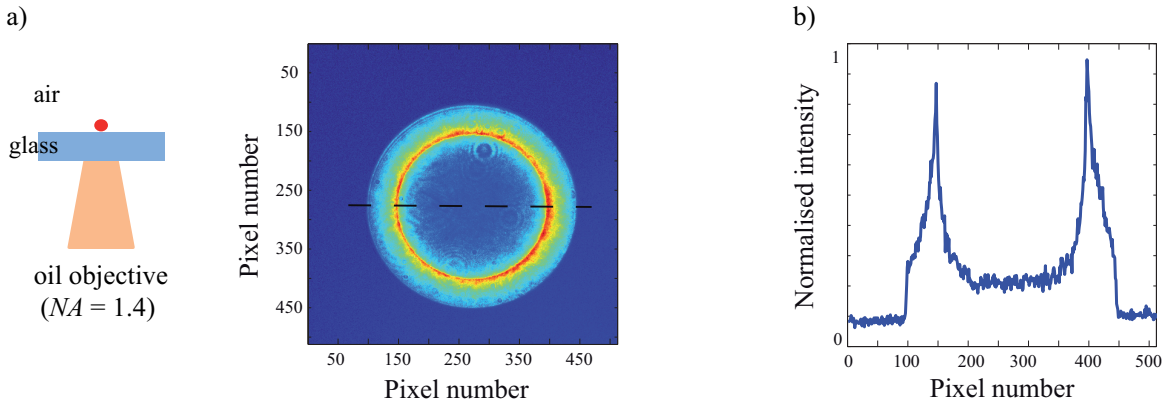

FIGURE 4.8: (a) The Fourier plane image by an EMCCD camera from a point-like emitter on glass surface characterized by an oil immersion objective and (b) its profile along the black dashed line

Since the dipole emitter is positioned above the glass substrate, the emission light travels from a medium with low refractive index n_1 (air) into another with higher index n_2 (glass). As discussed in subsection 4.2.2, the near field radiation is transformed into propagating field in the denser medium ($n_2 > n_1$). This evanescent light can be transmitted through the air-glass interface, propagating in the direction beyond the critical angle ($\theta_c = \arcsin n_1/n_2$). The light at supercritical angles is referred to as forbidden light [93]. It only occurs due to the effect of the substrate in the vicinity of the emitter. For the emitters situated further than the wavelength from the interface, there is virtually no evanescent light transmitted into the glass medium. Therefore, in our experiment, the angle θ of the wavevector is allowed to be larger than the critical one of the interface ($\theta_c = 41.5^o$), as presented in Figure 4.5.

Our obtained angular emission pattern as shown in Figure 4.8(a) coincides with established studies such as in [95] for the case of isotropic emitters near the air-glass interface. The pattern has two characteristic circular borders forming a ring bar on the outer part of the pattern. The outer circle is the limit resulting from the maximum collection angle while the inner one is due to the critical angle at the interface.

To analyze in more details, we plot the profile along the dashed line of this Fourier plane image in Figure 4.8(b) and matched the limits of this image (pixels 100 and 440) to the angles $-\theta_{max}$ and $+\theta_{max}$ (-67^o and 67^o), leading to the linear correspondence between pixels and

$\sin\theta$. More detailed, $(440 - 100)/2 = 170$ pixels is equivalent to 67°. The two peaks on figure 4.8(b) correspond to the coupling of the evanescent field in the low index medium (air) and the propagative field in the high index one (glass) which appears at the critical angle θ_c. Since the two experimental peaks starts at pixels 164 and 376, we have $(376 - 164)/2 = 106$ pixels, referring to the critical angle of 41.8°, which is nearly equal to the theoretical value. Within the ring bar limited by these two borders, the intensity is larger than in the center of the pattern, so the forbidden light is more intense than allowed light, as proven in [99] and as simulated in Figure 4.5. Since the microsphere emits light in all directions, its emission pattern has its intensity distributed in all azimuthal angles ϕ, forming such an uniform distribution of intensity within the ring bar. All these agreements between our recorded pattern and the previously calculations confirm the validation of our emission pattern measurement setup.

4.6 Emission pattern measurement and analysis

As mentioned above, we can extract qualitative information on the orientation of the dipole emitter with respect to the interface by interpreting the recorded emission pattern. We analyze the image recorded by emission pattern measurement in comparison with several simulated patterns corresponding to different dipolar dimensionalities and dipolar orientations.

As the emission pattern is proven to be strongly dependent on the kind of objective, the planar interface, and the distance between the emitter and the interface, we need to find out the proper conditions where we could distinguish the dipoles with different orientations. In most typical cases in which the emitters are well separated on a glass coverslip covered by a layer of PMMA and its emission is observed by an oil-immersion objective with high numerical aperture in contact with the other side of the glass coverslip, the angular pattern are quite similar whether the dipole is either an one or two dimensional one, as depicted in Figure 4.9. Therefore, using this configuration is not possible to discriminate between two dipolar dimensionality.

However, the configuration of an individual emitter sandwiched between a SiO_2 covered gold substrate and a PMMA layer and then characterized by the same oil objective is more promising to distinguish the dipolar dimensionality of the emitting dipole, as presented in Figure 4.10. We recall the definition of the dipolar orientation (Θ, Φ): the polar angle Θ is with respect to the z axis of the set up (the direction of propagation) and the azimuthal angle Φ is with respect to the x reference axis, as shown in Figure 2.1.

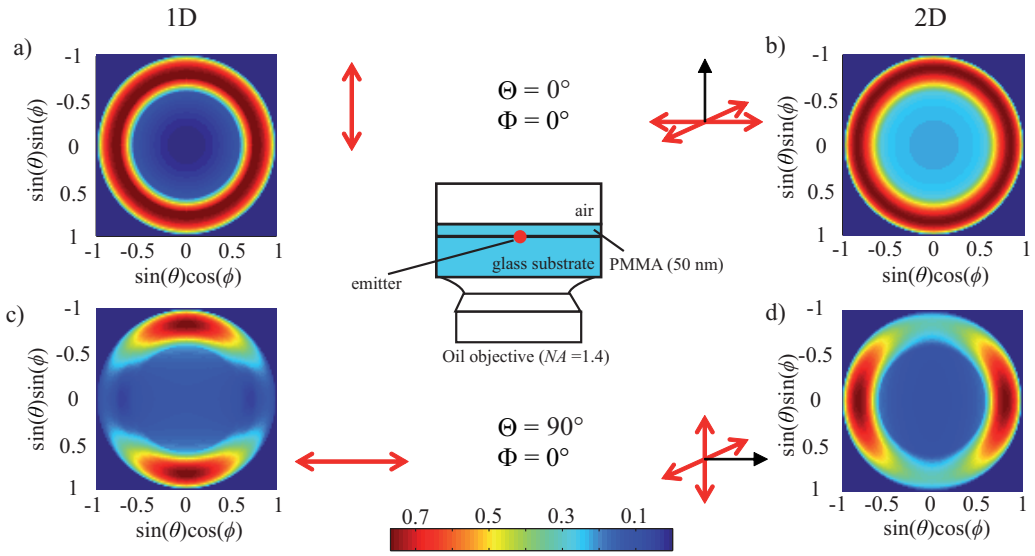

FIGURE 4.9: The theoretical emission patterns for different dipolar dimensionalities and polarizations with the reflection configuration of an individual emitter at a distance of 50 nm to the PMMA-air interface and its emission is collected by an oil immersion objective $NA = 1.4$ in contact with the glass substrate: (a) a vertical one dimensional dipole, (b) a horizontal two dimensional dipole, (c) a horizontal one dimensional dipole, (d) a vertical two dimensional dipole.

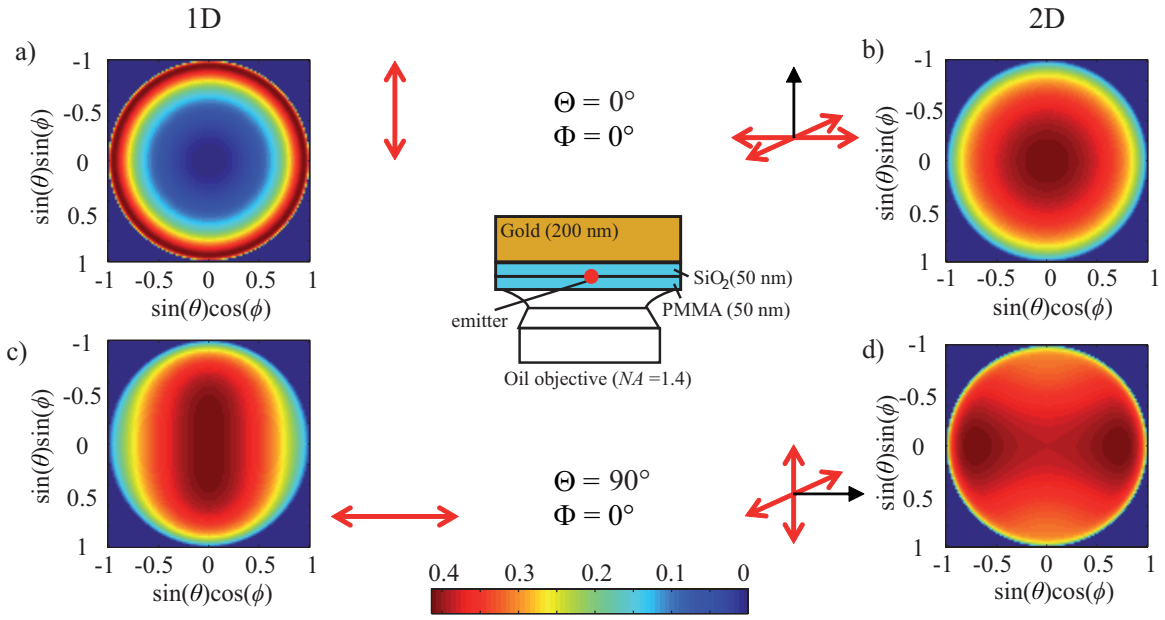

FIGURE 4.10: The theoretical emission patterns for different dipolar dimensionalities and polarizations with the configuration of an individual emitter sandwiched between a 50 nm SiO_2 covered gold substrate and a 50 nm PMMA layer with its emission collected by an oil objective ($NA = 1.4$) in contact with the PMMA: (a) a vertical one dimensional dipole, (b) a horizontal two dimensional dipole, (c) a horizontal one dimensional dipole, (d) a vertical two dimensional dipole.

For both dipolar nature (one or two dimensional one), when the dipolar orientation is along the z axis of the setup ($\Theta = 0$), referring to a vertical one dimensional dipole as Figure 4.10(a) or a horizontal two dimensional dipole as 4.10(b), the emission is distributed symmetrically around the z axis. On the other hand, when the dipolar orientation is normal to the z reference axis ($\Theta = 90^{o}$), referring to an one dimensional dipole in the sample plane as Figure 4.10(c) or a two dimensional dipole perpendicular to this plane as 4.10(d), the emission pattern has an preferred axis with the shape of the centre intensity distribution becomes elongated in different ways. Especially in the case of $\Theta = 0$, two patterns show distinct differences between the one dimensional dipole (isotropic pattern with higher emission intensity for larger angles) and the two dimensional one (higher emission intensity at the center around the dipolar orientation).

In sum, this technique is applicable to estimate the dipolar dimesionality by choosing the appropriated sample-objective configuration. In the following chapter, we will use this procedure for analyzing the Fourier plane images to investigate quantitatively the dipolar dimensionality and orientation of the emitter.

Conclusion

The emission pattern provides another method for studying the emission. It allows to estimate the ambiguity in polarimetric measurements. For example, a given value of the degree of polarization δ gives two possible dipolar orientation depending on the 1D or 2D dipolar dimensionality. The complementary emission pattern analysis helps to solve this ambiguous problem. By choosing a good experimental configuration, we could estimate the dipolar dimensionality, therefore, the orientation of the dipole can be inferred by the polarimetric measurements.

We later will use this emission pattern imaging together with the emission polarization measurement to study a new kind of two dimensional nanostructures called nanoplatelets.

Chapter 5

Determination of a single nanoplatelet dipole

Introduction

From the theoretical modelling and experimental methods developed in the previous chapters, we characterize here several types of nanoplatelets in order to determine the dimensionality and the orientation of their emitting dipole.

The nanoplatelets utilized in this study are classified as one kind of the colloidal semiconductor nanostructures. For more than three decades, the semiconductor nanometerials have been attracting considerable attention due to their outstanding physical and chemical properties that are distinct from bulk materials [100–104]. It is well known that these properties are strongly influenced by the shape, size, composition and structure of nanomaterials [105–108]. While a large number of papers have been published on spherical quantum dots [100, 109] and one dimensional nanostructures such as nanorods [105, 110], studies on two dimensional nano or microstructures have emerged recently due to many developments in chemical synthesis.

Among the different shapes of two dimensional nanostructures such as nanosheets [111], nanoribbons [112], or nanomembranes [113], nanoplatelets are of particular interest thanks to the successful archievements in thickness control [114–116]. In the last decade, more complex core/shell nanoplatelets with type I and type II optical transitions have finally been synthesized [117–119]. This expands the field of potential applications for nanoplatelets, especially in plasmonic/photonic devices as efficient light convertors and lasing with a low amplified spontaneous threshold.

The chapter is organized as follows. In the first section, we introduce general informations on semiconducting nanoplatelets. Secondly, the details of our studying on CdSe/CdS nanoplatelets will be described. After briefly mentioning the preparation of the sample, the details of experimental emission polarimetric measurements and emission pattern imaging are presented. We perform numerical simulations to obtain the correct dipolar orientation of the nanoplatelet for a given geometry and to verify the experimental findings. Finally, we focus on interpretations of the results and address the dipolar dimensionality as well as the dipolar orientation of the investigated nanoplatelets.

5.1 Colloidal semiconductor nanostructures

5.1.1 Bulk semiconductor material

In general, semiconductor materials are grouped into several classes of similar behavior. The classification is based on the position of the material in the periodic table of the elements. An important group of semiconductors is the Group II-VI compounds, which contain two elements, one from the second and the other from the sixth column of the periodic table. It is commonly written as $A^{II}B^{VI}$ where A denotes Cadmium (Cd), Zinc (Zn) and B denotes Selenium (Se), Sulfur (S), and Tellurium (Te). Cadmium selenide (CdSe) is one of the best-known members of the II-VI group and has gained numerous attention due to its potential applications in transistors [120], light emitting devices [121,122], solar cells [123,124] lasers [125].

Crystal structure

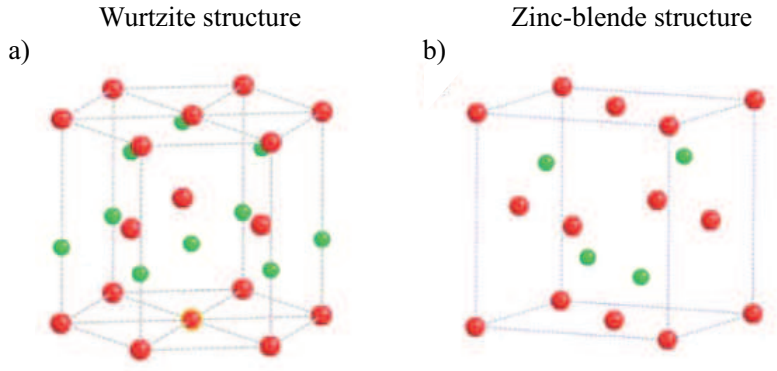

FIGURE 5.1: The two kinds of crystal structures of CdSe: (a) hexagonal (wurtzite) and (b) cubic (zinc-blende). Red and green balls represent Cd and Se atoms, respectively [126].

A crystal structure is composed of a unit cell, a set of atoms arranged in a particular way, which is periodically repeated in three dimensions on a lattice. Crystalline materials are thus distinguished thanks to their unique arrangements. Cadmium selenide (CdSe) is a direct semiconductor having two kinds of structures, namely, the zinc-blende crystal structure and the wurtzite structure. The bulk CdSe crystal is typically in the wurtzite phase but zinc-blende CdSe can also be synthesized. Both these crystal structures are depicted in Figure 5.1.

The wurtzite structure are hexagonal and each atoms are tetrahedrally bonded with 4 neighboring atoms of the other element. The zinc-blende structure is characterized by a face-centered cubic lattice of Se atoms as observed in Figure 5.1(b). Similar to wurtzite structure, the bonds between atoms are tetrahedrally coordinated.

Excitons

Light absorption within a semiconducting material promotes an electron into the conduction band and simultaneously leaves behind a hole in the valence band. Both electron and hole can freely move in the lattice sites. Like all charged particles, since electron and hole possess opposite charges, there is Coulomb interaction between them. The electron and the hole form a bound pair which could be viewed as a quasi-particle, so-called an exciton. It is of interest in a vast range of application such as optical nonlinearities [127], energy transport processes [128], optical bistability [129], light sensitization in color photography [130], and light harvesting units in photosynthetic systems [131].

There is a preferred separation distance between the electron and hole probability distributions in an exciton, and this distance is termed the exciton Bohr radius as expressed by:

$$a_B = a_0 \epsilon_r \frac{m_0}{\mu} \tag{5.1}$$

with a_0 denoting the Bohr radius of a hydrogen atom, m_0 referring to a free electron mass in vacuum and $\mu = \dfrac{m_e m_h}{m_e + m_h}$ being the reduced mass of the exciton. The Bohr radius of the exciton depends on the nature of the material, for example, the values of highly covalent materials such as group IV or III-V semiconductors is about tens of nanometers while more ionic materials such as the II-VI or IV-II semiconductors have exciton distances less than 10 nm. The CdSe bulk exciton Bohr radius is $a_B = 5.6$ nm [132].

5.1.2 Colloidal nanostructures

When a semiconducting system reduces its size from a bulk material to be on the same order as the exciton Bohr radius, quantum confinement effect occurs. The electronic and optical properties become size dependent, resulting in significant development for advanced nanotechnology [133]. For example, quantum confinement changes the continuous energy bands of a bulk material into discrete, atomic-like energy levels in nanomaterials, leading to a discrete absorption/emission spectrum.

In a nanostructure, the electron/hole is confined in one or more dimensions. Thanks to many successful developments in fabrication, it is possible to control the size of the nanostructures in different dimensions. It should be noted that the dimensionality of the material is referred to as its number of degrees of freedom, therefore, it is opposite to the number of confined dimension.

Based on their geometry, nanomaterials can be classified as:

- (i) zero dimensional structures (0D) so called as nanoparticles, nanocrystals, and the most popular name - quantum dots: They are composed of several tens to a few thousand atoms, with all the electrons are localized (3D confinement);

- (ii) one dimensional materials (1D) which are cylinder-like such as nanowires, nanorods, and nanotubes with diameters/cross section in the nanoscale and lengths typically in the micrometer range: The excitons are only free to move along the structure (2D confinement);

- (iii) two dimensional (2D) object, for example, nanosheets, nanoribbons and nanoplatelets with the thickness of the order of a few nanometers: The electrons are restricted in the direction perpendicular to the structure (1D confinement).

These three categories are schematized in Figure 5.2.

5.1.2.1 Quantum dots

In 0D nanostructures like quantum dots the carriers are confined in all the three directions. Since strong confinement is provided, these nanocrystals possess properties that are strongly dependent on their size and morphology. Their absorption and photoluminescence

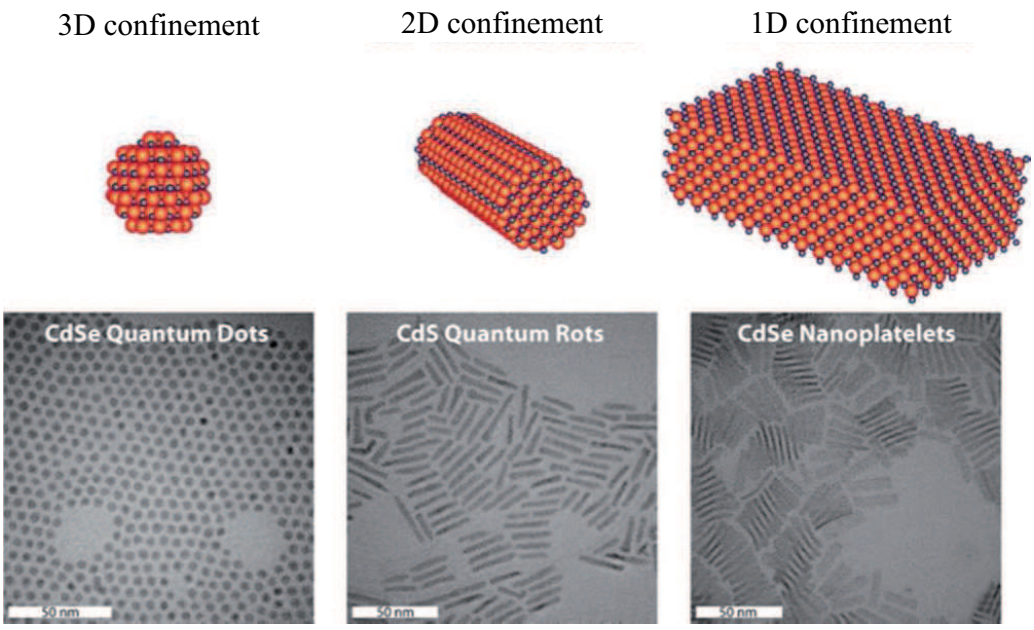

FIGURE 5.2: Schematic representation of three types of quantum confined colloidal nanostructures: quantum dots, nanorods, and nanoplatelets [32].

can be controlled precisely by varying their diameter. Therefore, they have emerged as potential light sources in a variety of practical applications, such as photodetectors [134] and biosensing/bioimaging [135].

Quantum dots are normally made from the II-VI or III-V compounds, for example, CdSe, CdS, ZnO, InP, InAs. They could be synthesized by many methods, such as chemical vapor deposition (CVD) [136], physical vapor deposition (PVD) [137], and solution-based approaches. The wet chemical synthesis has become the most popular because it is simple, low cost, and mass produced. The size and dispersivity of colloidal quantum dots can be well controlled by managing the synthesis conditions, such as reaction time, temperature, and surfactants [138]. These organically passivated quantum dots have suffered from nonradiative surface-related trap states, resulting in low fluorescence quantum yield [139,140]. This could be overcome by growing layers of an other material to form the core/shell structure, which will efficiently passivate the surface trap states [141,142], therefore, give rise to quantum yield [143,144]. Moreover, the shell also acts as a layer protecting the core against the surrounding medium such as environmental changes or photo-oxidation [140]. Synthesis of colloidal core/shell quantum dots is now a very developed field of study with many real life applications [145].

5.1.2.2 Nanorods

One dimensional nanostructures such as rods, wires, and tubes are interesting objects in the fields of nanomaterials. They share many same properties to quantum dots or nanoplatelets, such as quantum confinement effects. However, thanks to their geometry, they possess some characteristics that are difficult to achieve by the other two categories, for example, 1D confined transport of electrons/photons and excellent mechanical properties [146]. Therefore, these cylindrical nanomaterials has been studied and introduced in many fields, such as, batteries [147], solar cells [148], and photoelectrochemical cells [149].

For about twenty years, many researchers have focused on developing one dimensional semiconductor nanostructures [150,151]. They could be fabricated by both physical and chemical approaches, for example, lithography, oxide-assisted growth or solution–liquid–solid growth in organic solvents. In addition, the changeable chemistry of fabricating colloidal core/shell nanorods enables the formation of some new structural semiconductor heterojunctions like CdSe/CdS dot-in-rods. Depending on synthetic methods, the morphology-associated properties and application explorations vary in the vast range. Many oxide II-VI nanomaterials such as ZnO have already been extensively researched and applied in life [152].

5.1.2.3 Nanoplatelets

Nanoplatelets are a new category of two dimensional materials consisting of a thin crystalline slab of inorganic material [28, 153]. They are of great interest for fabricating functional devices due to their high suface to volume ratio, well controlled nanoscale thickness, good optical and photonic properties. Since the thickness of the nanoplatelet is smaller than the exciton Bohr radius, while the lateral dimensions are much larger, they can be considered as an atomic system with high spatial confinement in a single dimension, as shown in Figure 5.2. They have been grown from a wide variety of materials, but those made from semiconductors give very promising optical properties [32, 154, 155].

These nanoplatelets have electronic properties similar to two-dimensional quantum wells formed by molecular beam epitaxy, and their emission spectra could be tuned precisely by their thickness of growth. One of the most common colloidal nanoplatelets are Cadmium based ones. They are direct semiconductors in the visible region, and synthesized in both crystallite structures. In 2006, Hyeon and coworkers reported the synthesis of wurtzite CdSe nanoribbons. Zincblende CdSe nanoplatelets were synthesized in 2008 by Ithurria and Dubertret [116]. The synthesis is based on a variation of the protocol developed by Cao and co-workers for the syn-

thesis of zincblende spherical nanocrystals. In contrast with the wurtzite CdSe 2D structures, the zincblende nanoplatelets have their thickness in the [001] direction.

5.1.3 Core/shell nanoplatelets

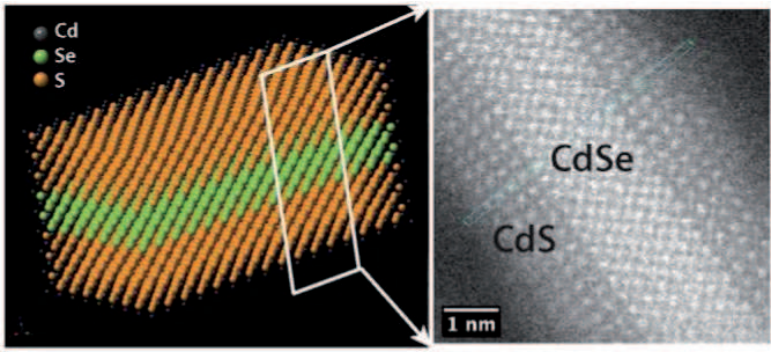

FIGURE 5.3: Schematic representation of a core/shell CdSe/CdS nanoplatelet [32].

In order to reduce the nonradiative processes related to the surface, considerable efforts have been devoted to the optimization of the platelet nanostructures. As already observed in the case of core/shell quantum dots or nanorods, the growth of core/shell nanoplatelets would further enlarge the properties and applications of the materials, especially in the fields which are experimentally limited to epitaxial quantum wells. Therefore, core/shell semiconducting nanoplatelets have been at the center of intense research for last ten years. Such structures are believed to enable researchers to take full advantage of nanoplatelet′s optical properties, resulting in further achievements in photonics, nanoscale lasers and other nonlinear optical devices [156–160].

The core/shell CdSe/CdS nanoplatelets with quantum yield up to 80% is sucessfully synthesized in [117]. The shell deposition induces a strong redshift of both the light hole and heavy hole transitions, as seen in Figure 5.4(b). This shift is stronger than the shift observed when a CdS shell is grown on a CdSe spherical dot of which the emission wavelength is close to the CdSe core nanoplatelet one. It is explained by Tessier et al [117] that in the case of a free electron in vacuum the ground-state energy in a quantum well with a thickness d is identical to the ground-state energy in a spherical quantum dot with a diameter $2d$. The shell deposition also helps to reduce the fluorescence intermittency (blinking) at the single particle level. The third effect of the shell growth is that the lifetime increases compared to the core-only-nanoplatelet, as seen in Figure 5.4(d). The CdSe/CdS nanoplatelets are characterized as quantum well structure due to energy gap difference between the core CdSe and the shell CdS,

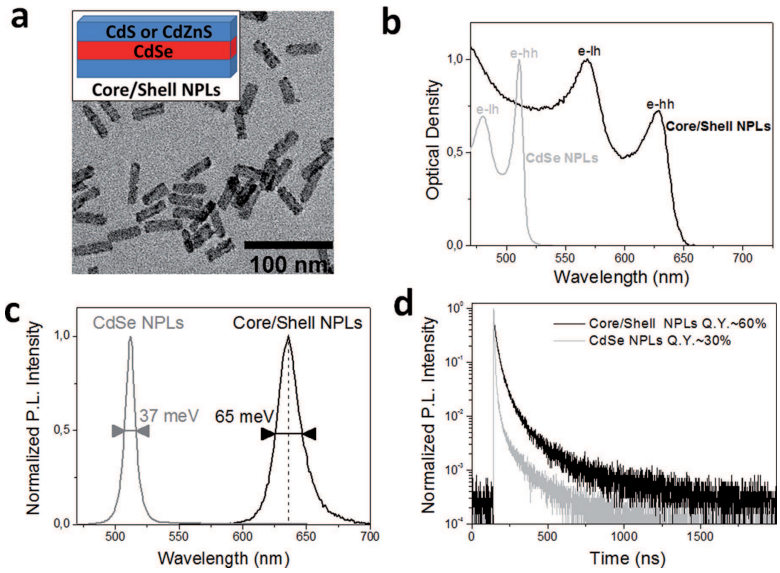

FIGURE 5.4: (a) TEM image of core/shell CdSe/CdZnS nanoplatelets and their schematics. (b) Absorption spectra of solutions of core CdSe nanoplatelets (gray) and CdSe/CdZnS nanoplatelets (black). (c) Photoluminescence spectra of solutions of core CdSe nanoplatelets (gray) and CdSe/CdZnS nanoplatelets (black). (d) Intensity decay of solutions of core CdSe nanoplatelets (gray) and CdSe/CdZnS nanoplatelets (black). All measurements were done at room temperature [117].

however, their optical characteristics and further enhancement of the emission in nanodevices remains to be investigated.

5.2 CdSe/CdS nanoplatelets

5.2.1 Characterizations of nanostructure and morphology

Among the enormous variety of nanoscale semiconductor materials, the nanostructures chosen for this study are the core/shell CdSe/CdS nanoplatelets. They are chemically synthesized by the research team of Benoit Dubertret, at ESPCI. These nanoplatelets consist of a CdSe core between two CdS shell layers, with different structural shapes as schematized in Figure 5.5.

The CdSe core nanoplatelets were prepared following the protocol as published in [116]. In brief, cadmium myristate is mixed with selenium powder in octadecene and heated to 240°C. When the temperature reaches 180°C, an acetate salt is injected into the solution and CdSe nanoplatelets are formed. The thickness of these platelets is only several atomic layers and can

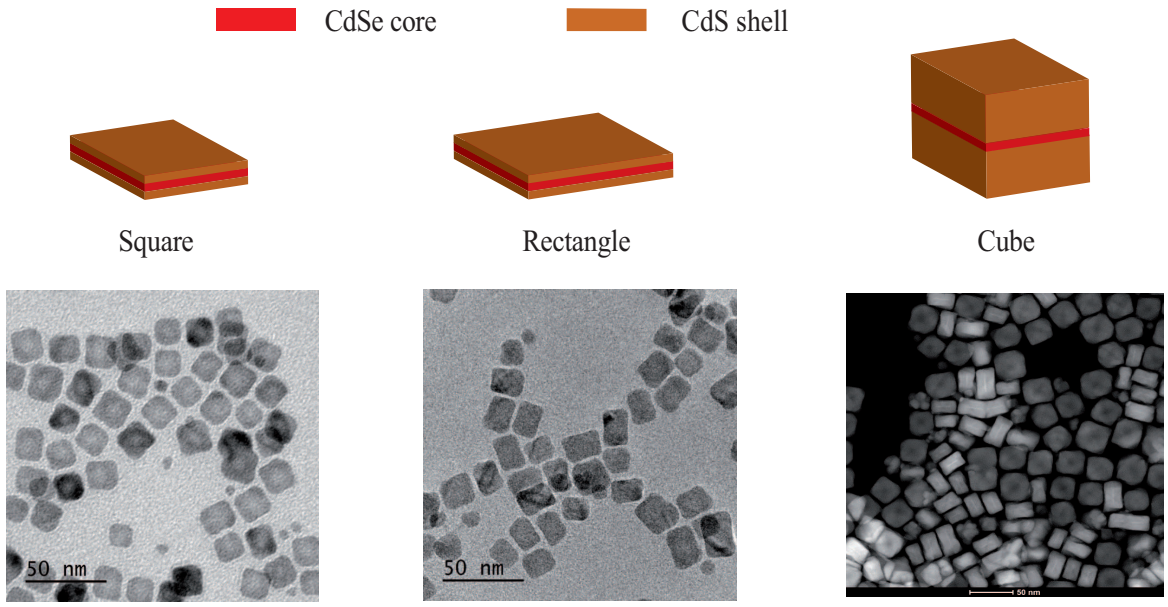

FIGURE 5.5: Schematic representations and TEM images of the square, rectangular, and cubic nanoplatelets, respectively. All the TEM measurements were performed by Benoit Dubertret's team.

be accurately controlled. They grow in the zinc blende phase, along a [001] axis. The exposed [001] surface is atomically flat, while the other [100] and [010] directions can extend to roughly 100 nm, depending on the reaction time [161]. The shell growth is accomplished by an one-pot method [117, 162]. This approach is based on the in situ generation of hydrogen sulfide by the reaction of thioacetamide with octylamine [163]. By adding cadmium source continuously, the reaction is kept performing for a few hours until nanoplatelets with a desired thickness and lateral sizes are obtained. The transmission electron microscope (TEM) images of the square, rectangular, and cubic structures are also presented in the figure 5.5.

TEM samples are prepared by drop-casting diluted nanoplatelet solutions onto carbon coated copper grids. The diluted concentration is chosen ($\sim 10^{-8}M$) in order to prevent the gathering of nanoplatelets. From these TEM images, three dimensions of the square nanoplatelet is approximately estimated about (16 $\pm$ 2 nm) long x (16 $\pm$ 2 nm) wide x 2 nm thick. The rectangular nanoplatelets have the same width and thickness but they measure longer length of 20 $\pm$ 3 nm. The cubic nanoplatelets have the same length and width as the square one, but with much thicker CdS shell layers; therefore, their total thickness are briefly from 10 to 15 nm.

We assume that their two dimensions (width and length) equal to:

$$l_1 = l_0(1 - \Delta l) \tag{5.2}$$

$$l_2 = l_0(1 + \Delta l) \tag{5.3}$$

The size factor is thus defined as:

$$\Delta l = \frac{l_2 - l_1}{l_1 + l_2} \tag{5.4}$$

which ranges from 0 (square nanoplatelets $l_1 = l_2$) to 1 (very elongated rectangles $l_1 \ll l_2$).

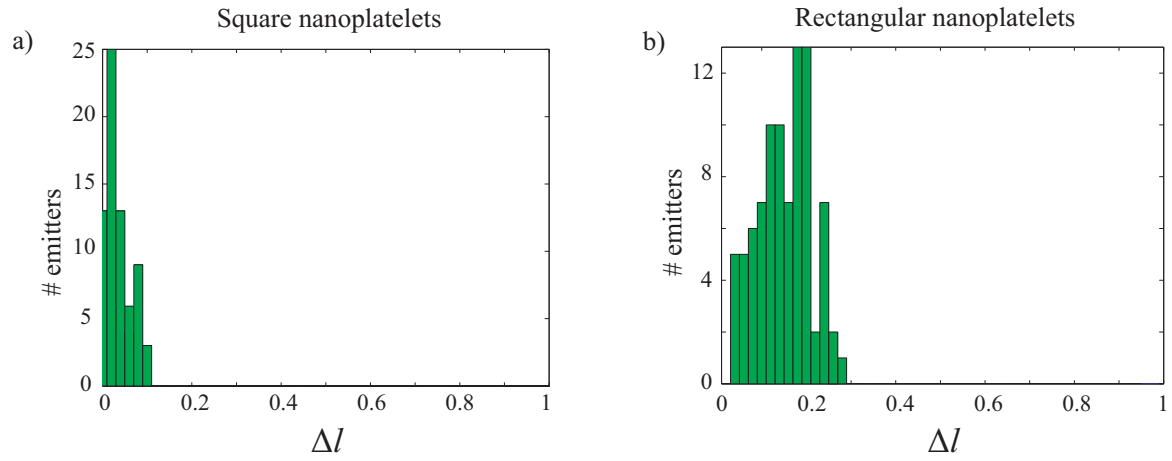

FIGURE 5.6: Histogram of the size ratio Δl measured for (a) 69 square nanoplatelets and for (b) 88 rectangular platelets.

From the values of the width and the length of the platelets obtained from the TEM images, the size factor Δl of 69 square nanoplatelets and 88 rectangular ones are calculated and then histogrammed in Figure 5.6 (a) and (b), respectively. For the square nanoplatelets, the Δl factor ranges from 0 to 0.08, referring to a slightly structural elongation. On the other hand, in the case of rectanglar nanoplatelets, the deviation of Δl is much larger (between 0.02 and 0.24), affirming their rectangular shape.

5.2.2 Optical properties of the colloidal nanoplatelets

Figure 5.7 presents the normalized absorption and photoluminescent spectra of two different types of colloidal nanoplatelets at room temperature. Our excitation laser at 450nm is in the good range of nanoplatelet′s absorption. The emission wavelength is centered at about 650-660 nm for all types of nanoplatelets.

In both cases of square and rectangular nanoplatelets, the photoluminescent spectrum is sharp and narrow: its emission bandwidth is less than 20 nm, smaller than the typical value obtained for the spherical core/shell CdSe/CdS quantum dots (25-30 nm). It refers to minimal surface trapping, as expected in these atomically flat core/shell nanoplatelets. These narrow

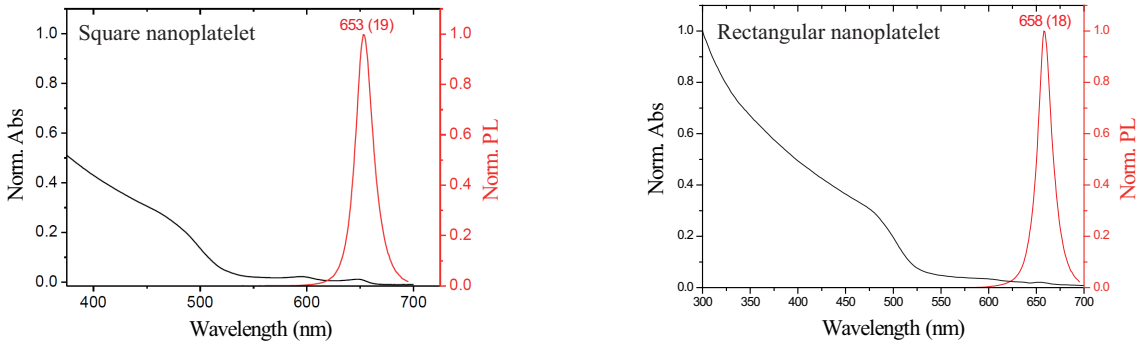

FIGURE 5.7: Room temperature normalized absorption and photoluminescent spectra of the colloidal square and rectangular nanoplatelets. All these measurements were performed by Benoit Dubertret's team.

spectra with very low inhomogenous broadening also confirm that the chemical synthesis is so accurately controlled that the nanoplatelets form with no much difference in thickness.

5.2.3 Optical properties of a single nanoplatelet

We perform photoluminescence intensity and photoluminescence decay profile measurements for some individual square nanoplatelets deposited on the glass substrate when the oil objective is in contact with the other side of the substrate without emitters, as schematized in Figure 5.8(a). These nanoplatelets are excited by a pulsed laser at the wavelength of 450 nm and the repetition rate of 25 MHz.

Figure 5.8(b) describes the photoluminescent intensity of some square individual nanoplatelets under the constant lasing excitation energy. Their fluctuation, or blinking, confirms that the emitters are single and well isolated. Different from the typical core/shell CdSe/CdS quantum dots, the emission of the square nanoplatelets is not really stable as a dark state (no emission state) is clearly observed.

The photoluminescent decay profiles of these mentioned square nanoplatelets are shown in Figure 5.8(c). These curves fit to a biexponential function $f(t) = A\,e^{-t/\tau_1} + B\,e^{-t/\tau_2} + C$ with time constant τ_1 about 9-12 ns and τ_2 about 37-40 ns. It brings up a question why we have a biexponential fitting. Since the photoluminescent decay profile reflects the contribution of non-radiative and radiative emission, there could be two hypotheses.

In the first one, the quick decay is due to non-radiative channels which accelerate the decay rate. It may result from charges or surface defects. Then the long lifetime corresponds to

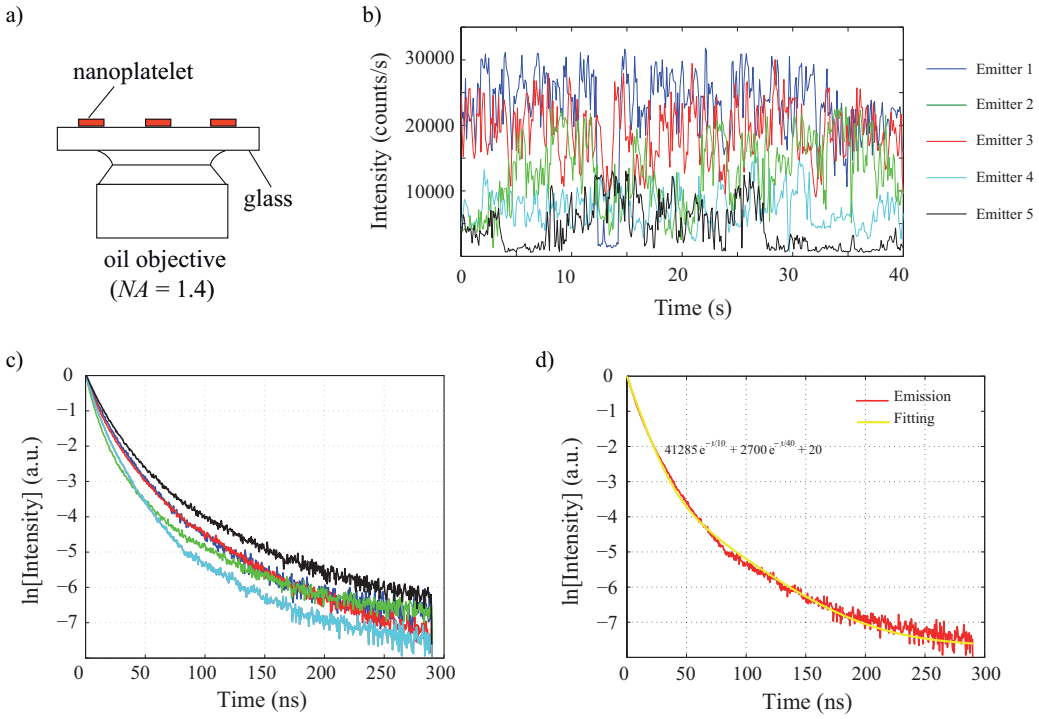

FIGURE 5.8: (a) Schematic of experimental configuration. (b) Detected photoluminescent intensity as a function of time 5 individual square nanoplatelets on a glass substrate with the same excitation energy. (c) Their corresponding photoluminescent decay profiles in semilog scale. (d) The decay profile of emitter numbered 3 is fitted with the biexponential function $f(t) = A\,e^{-t/\tau_1} + B\,e^{-t/\tau_2} + C$.

the exciton emission. The other hypothesis developed in [164] is that the surface traps induce the localization of the hole wave function, resulting in a longer emission lifetime. In this case, the bandgap emission corresponds to the short decay.

5.3 Preparation of samples

We will characterize all three types of nanoplatelets with the same experimental setup which has mentioned in the previous chapter. The photoluminescence of an individual nanoplatelet was analyzed both in terms of polarization characterization and emission pattern, as observed in Figure 5.9(a).

The sample consisted of well separated emitters on a clean SiO_2 covered gold substrate. This substrate was made of a silicon wafer covered by 200 nm of gold (thermal evaporation) and 50 nm of SiO_2 (ion-assisted deposition), respectively. The nanoplatelets were spin coated onto the SiO_2 surface with a density of around 1 emitter per 3 μm^2 and then covered by 50 nm of polymethylmetacrylate (PMMA) for protection. The oil objective was introduced directly in contact with the PMMA layer. As the reflective indices of oil, silica and PMMA are all close to 1.5, it could be considered that the emitters are in a dielectric semi-infinite medium with the index of 1.5 and at a distance of 50 nm from the PMMA-gold interface, corresponding to objective-sample confuguration (ii). It should be noted that this very low concentration of the emitters on the substrate is important to ensure the independence of single emitter analysis.

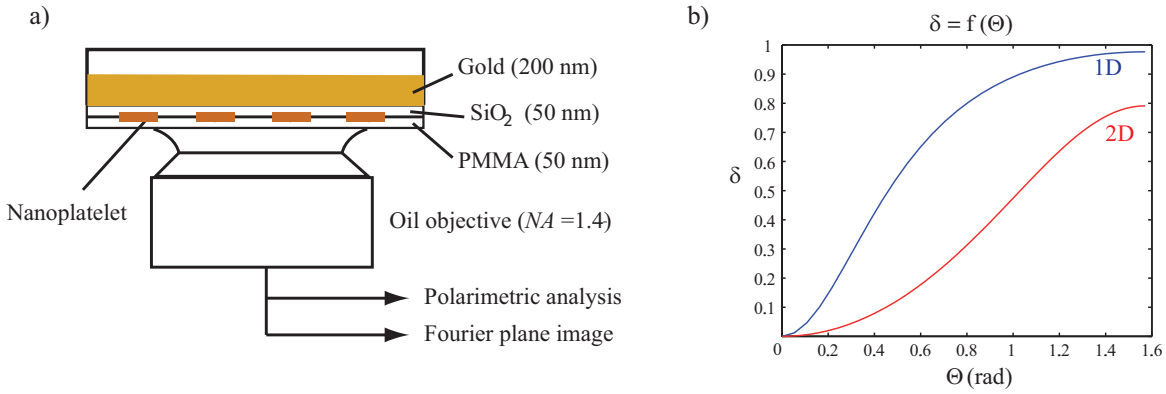

FIGURE 5.9: (a) Schematic of the experimental sample structure and (b) Theoretical values of the degree of polarization δ as a function of the dipolar angle Θ (dipolar orientation) for an one dimensional dipole (blue line) or a two dimensional dipole (red line), calculated in the objective-sample configuration (ii) when nanoplatelets is at a distance of 50 nm to the PMMA-gold interface and their emission is collected by an oil objective $NA = 1.4$).

Figure 5.9(b) shows the theoretical values of the degree of polarization δ as a function of

the polar angle Θ for an one or two dimensional dipole in the case of reflection configuration which has schematized in Figure 5.9(a). We recall that the dipolar azimuthal angle Φ could be derived from the polarization analysis angle β by fitting the normalized polarimetric curves with the following equation:

$$I(\beta) = I_{min} + (I_{max} - I_{min}) \cos^2(\Phi' - \beta) \tag{5.5}$$

with $\Phi' = \Phi$ for an one dimensional dipole whereas $\Phi' = \Phi + \pi/2$ for a two dimensional dipole.

After the polarimetric analysis on the photoluminescence is presented, the emitting dipolar orientation (Θ, Φ) of a single nanoplatelet is extracted by using the theoretical framework discussed in Chapter 3 and 4.

5.4 Square and rectangular nanoplatelets

We consider the nanoplatelets with their thickness of 2 nm which is smaller than the exiton Bohn radius, corresponding to an one dimensional confined nanostructure. There are two investigating shape: square (16 x 16 nm^2) and rectangle (15 x 20 nm^2).

5.4.1 Square nanoplatelets

We firstly performed the polarization measurement and the emission pattern measurement for several individual square nanoplatelets, respectively. Figure 5.10 presents the normalized polarimetric curves (a) and the corresponding emission patterns (b) of four well isolated square nanoplatelets deposited on the SiO_2 covered gold substrate with PMMA protection layer. The polarimetric results gives similar very weak polarizations while all the emission patterns are the most intense at the center.

Figure 5.10(a) presents the photoluminescence polarization analysis of typical square nanoplatelets. The detected intensity after being normalized by the total intensity is plotted as a function of the halfwave plate′s rotating angle ϖ which is half of the angle of polarization analysis β ($\varpi = \beta/2$). This curve is well described by Equation 5.5 (red line), and we find a degree of polarization $\delta = \dfrac{I_{max} - I_{min}}{I_{max} + I_{min}}$ of 0.02 to 0.04. The values of the azimuthal angle Φ (extracting from the phase of the polarimetric curves) are randomly distributed as expected from the spin-coating deposition.

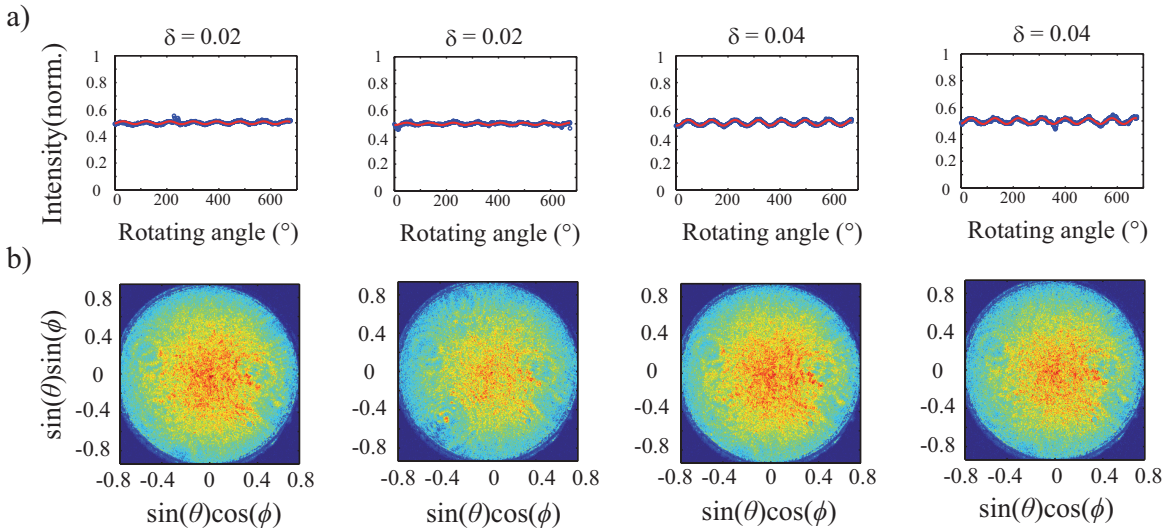

FIGURE 5.10: Square nanoplatelets: (a) Blue circles: normalized intensity as a function of the rotating angle ϖ of the halfwave plate; solid red line: fitting of the experimental curve with Equation 5.5 and (b) Their corresponding recorded emission patterns. The objective-sample configuration is schematized in Figure 5.9(a).

We continue this polarimetric measurement for a collection of square nanoplatelets then plot a histogram of the obtained values of the degree of polarization δ as displayed in Figure 5.11(a). The values of δ is less than 0.1 for all characterized emitters, with a very low dispersion, corresponding to the polar angle $\Theta \approx 0$ as given by the theoretical curve in Figure 5.9(b).

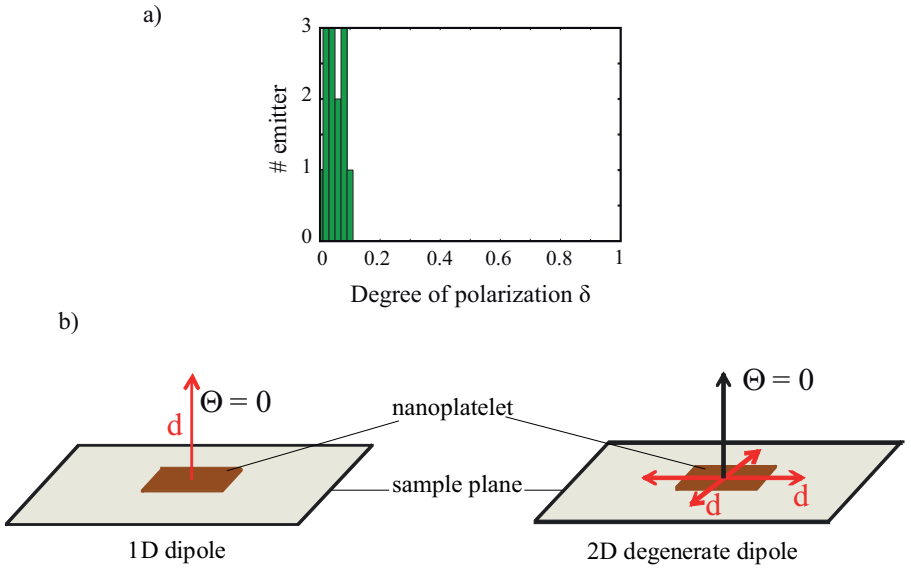

FIGURE 5.11: Square nanoplatelets: (a) Histogram of the degree of polarization δ measured for 13 emitters and (b) Proposed schematics of a emitter's dipole.

The photoluminescence is thus, for each nanoplatelet, nearly unpolarized. From the polarimetric model, the result $\Theta \approx 0$ leads to two possible interpretations. As the square nanoplatelet

is atomically flat, we can describe each platelet as lying on the sample plane with either an one dimensional dipole along the z direction (perpendicular to the sample plane) or a two dimensional dipole in the (x, y) sample plane, as schematized in Figure 5.11(b). We now turn to the emission pattern measurement in order to discriminate between these two ambiguous interpreting cases.

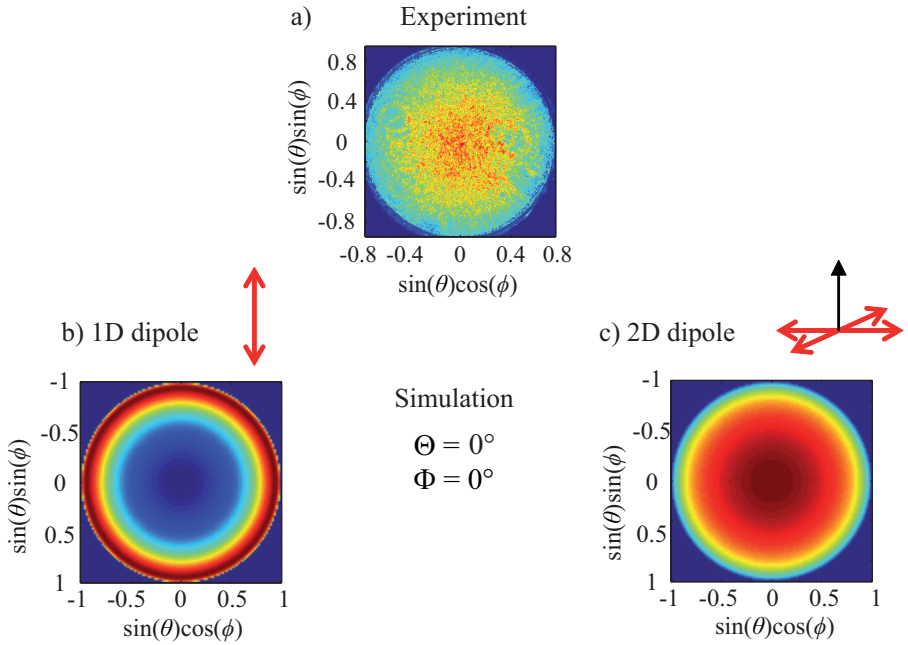

FIGURE 5.12: In the configuration of an individual emitter sandwiched between a 50 nm SiO_2 covered gold substrate and a 50 nm PMMA layer with its emission collected by an oil objective ($NA = 1.4$) in contact with the PMMA: (a) the experimental Fourier image, (b) the emission pattern simulated for an one dimensional dipole along z direction, and (c) the pattern simulated for a two dimensional dipole in the (x, y) sample plane.

As discussed in the last section of the previous chapter, the Fourier plane imaging provides a practical mean to distinguish clearly between one and two dimensional dipoles. In the experimental Fourier plane images shown in Figure 5.10(b), the high intensive emission are centered along the optical axis of the emitters, and the intensity decreases toward the outer side of the pattern isotropically. Figure 5.12 shows the comparison between the experimental image (a) and the simulated pattern for two types of dipole (b) and (c). The captured pattern completely disagrees with the simulated pattern for a case of one dimensional dipole (Figure 5.12(b)) but quite similar to the simulation of a two dimensional one (Figure 5.12(c)), referring to a 2D dipolar dimensionality.

More detailed analysis has been employed in order to compare the experimental Fourier plane images with the theoretical emission pattern of a two dimensional dipole with the dipolar orientation $\Theta = 0$. Figure 5.13(a) presents the comparison between the emission dia-

gram $dP/d\Omega$ as the function of the observation direction (θ, ϕ) measured for a given square nanoplatelet and simulated for a horizontal two dimensional dipole (the polar angle to the z axis of the setup $\Theta = 0$).

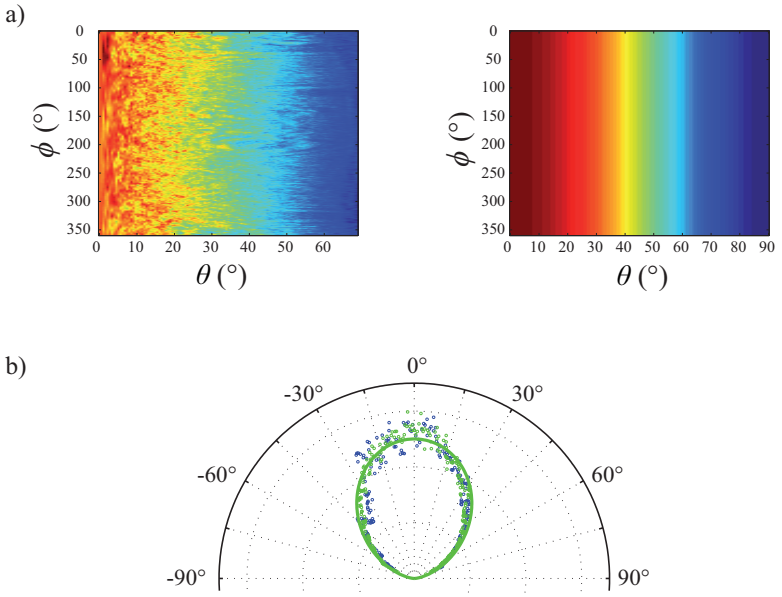

FIGURE 5.13: a) Measured (left) and simulated (right) emission diagram as a function of the emission directions (θ, ϕ); b) Measured angular emission intensity distribution (green circles for $\phi = 0$ while blue circles for $\phi = 90^o$) and simulated emission pattern along any in-plane direction ϕ (green solid line) as a function of the emitting angle θ. Noted that the measurements are performed on square nanoplatelets in the PMMA half-space at a distance of 50 nm to the PMMA-gold interface (Figure 5.9(a)) and the simulation are calculated for a horizontal two dimensional dipole ($\Theta = 0$) in the same interface configuation.

It should be noted that in the measured emission diagram, the angular coordinates (θ, ϕ) are calculated by interpolating from the (x, y) coordinates of the Fourier plane into the (k_x, k_y) coordinates of the EM-CCD detecting plane ($k_x = r\cos\phi = f\sin\theta\cos\phi$ and $k_y = r\sin\phi = f\sin\theta\sin\phi$). Therefore, the data with small θ is averaged over less pixels of the camera than the data with higher θ, resulting in the presence of more noises at small θ in the measured image than the calculated one as observed in Figure 5.13(a). Moreover, we observe a contant emission flux with respect to ϕ in the range of imaging noise. On the contrary, the emission intensity decreases while the angle θ increases. The result clearly confirms that the intensity is the most intense at the center of the measured emission pattern. It also agrees well with the theoretical data calculated for a two dimensional dipole with $\Theta = 0$.

Since the emission is isotropic around the axis of the emitter, we could plot the measured angular pattern profile along any in-plane direction ϕ, for example, 0 and 90° presented as green and blue circles respectively in Figure 5.13(b). As the theoretical pattern is not dependent on

the in-plane direction ϕ, its profile is demonstrated by a green solid line corresponding to any value of ϕ. The good fitting between the theoretical profile and these experimental data indicates that the nanoplatelets photoluminescence originates from a two dimensional dipole oriented perpendicularly to the sample plane.

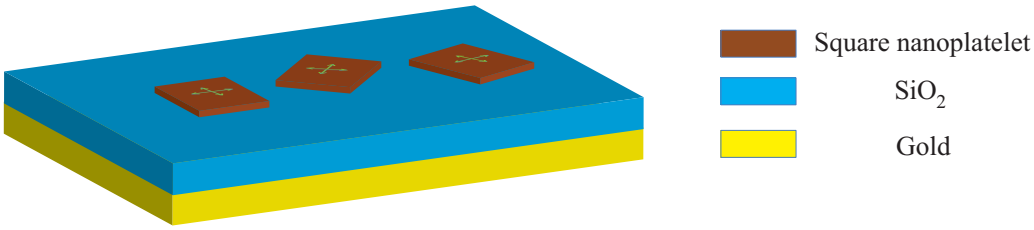

FIGURE 5.14: The schematic representations of ultrathin nanoplatelets and their two dimentional emitting dipole on the substrate.

Thanks to the 2 dimensional structural geometry of nanoplatelets, all these ultrathin emitters definitely lie on the substrate as observed in TEM images in Figure 5.5(b), so their two dimensional dipoles are in the plane of the nanoplatelets themselves. Therefore, the orientation of their emitting dipole is the same for all ultrathin nanoplatelets, as schematized in Figure 5.14.

5.4.2 Rectangular nanoplatelets

5.4.2.1 Polarized emission

Since the emission from some square nanoplatelets is found to be slightly polarized (less than 10%), it can be assumed that such a weak polarization may due to a slightly rectangular shape of the platelets, as observed in Figure 5.6. The emission polarization and emission pattern measurements have been then repeated with the second kind of nanoplatelets - the rectangular ones. The original idea is to understand if the shape of the nanoplatelet could have any influence on the polarization state of its emission.

Figure 5.15(c) shows a histogram of the obtained values of the degree of polarization δ of 18 individual rectangular nanoplatelets. The value of δ varies from 10% to 30%, higher than of the square nanoplatelets. This result suggests that the emission polarization is related mainly to the geometric aspect ratio of the nanoplatelet. The large variation of the histogram of the measured degree of polarization leads us to two hypotheses.

The first interpretation for this polarized emission is that the dipolar orientation of the two dimensional emitting dipole may be tilted ($\Theta \neq 0$), which seems to be abnormal since

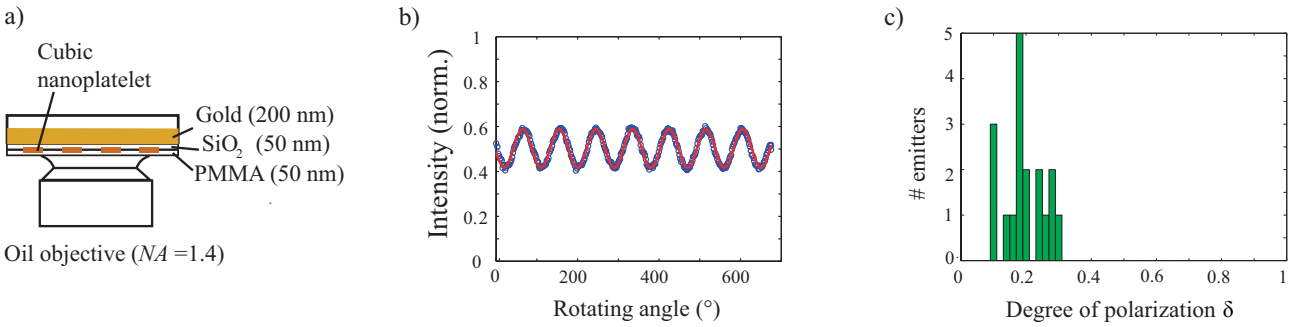

FIGURE 5.15: Rectangular nanoplatelets: (a) Schematic of the objective-sample configuration. (b) Measured polarimetric emission analysis with blue circles presenting normalized intensity as a function of the rotating angle ϖ of the halfwave plate and a solid red line for the fitting of the experimental curve with Equation 5.5. (c) Histogram of degree of polarization δ measured for 18 nanoplatelets.

the nanoplatelet is supposed to lie on the substrate due to its morphological characteristics. However, as the emitters are chemically synthesized, it may either result from defects in the crystalline structure or just because the platelet imperfectly horizontally lies on the substrate, as illustrated in Figure 5.16(a).

Another explanation of the polarized emission we propose, is that the two dimensional dipole can not be modelled by a sum of two degenerate orthogonal one dimensional dipoles ($d_1 = d_2 = d$), but by non-degenerate dipoles with $d_1 \neq d_2$ (corresponds to $\frac{d_0}{2}\sqrt{1+\eta}$ and $\frac{d_0}{2}\sqrt{1-\eta}$ in relative units), as described in 5.16(b). The possible values of the dipolar asymmetric factor η is from -1 to 1 as it is not necessary to know exactly which component dipole is oscillated more strongly.

5.4.2.2 Relevant hypotheses raised by emission pattern analysis

The present experimental configuration does not enable us to distinguish between these two hypotheses because their corresponding simulated emission patterns are quite similar. However, the difference between these two ambiguous interpretations is clearly observed when we consider an other objective-sample configuration. Figure 5.16(c) illustrates the new interface configuration: The emitters are well spin-coated on the glass substrate and their emission is collected by an oil objective with the numerical aperture of 1.4 in contact with the side without emitters of the substrate. Since the refractive indices of glass and oil are very close to each other, it is considered as the nanoplatelets are at the air half-space of the air-glass interface. The simulated Fourier plane images of a tilted two dimensional dipole with $\Theta = 30^o$ and a non-degenerate dipole by a dipolar asymmetric factor η of 0.2 are described in Figure 5.16(d)

and (e) respectively.

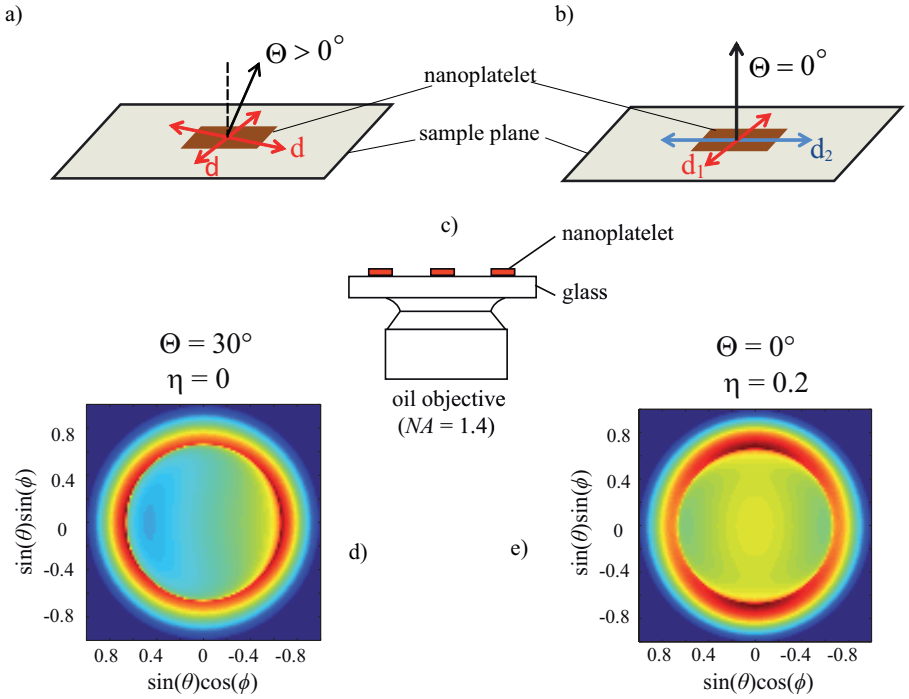

FIGURE 5.16: The schematic representations of two interpretations for the nanoplatelet's emitting dipoles (a,b) and their corresponding simulation of Fourier plane images (d,e) in the case of emitters directly positioned on glass substrate with an oil objective (NA - 1.4) in contact with the other side of the substrate as schematized in (c).

Both calculated images Figure 5.16(d) and (e) present a clear ring at the critical angle θ_c corresponding to the total internal reflection at the air-glass interface. However, there is a qualitative difference between these two images. In the pattern of a degenerate dipole oriented at $\Theta = 30^o$ with respect to the z reference axis, the emission part inside this ring is asymmetric. On the other hand, if the emitting dipole does not present the same energy along two different orthorgonal directions (a non-degenerate dipole), the emission part inside the ring has an axial symmetry while the ring itself no longer remains isotropic. Therefore, we perform the emission pattern measurements with the configuration described in Figure 5.16(c).

The measured Fourier plane image as presented in Figure 5.17 concides with the second hypothesis, indicating that the luminescence from rectangular nanoplatelets can be modelled as originating from a horizontal two dimensional dipole consisting of two non-degenerate one dimensional dipoles ($d_1 \neq d_2$).

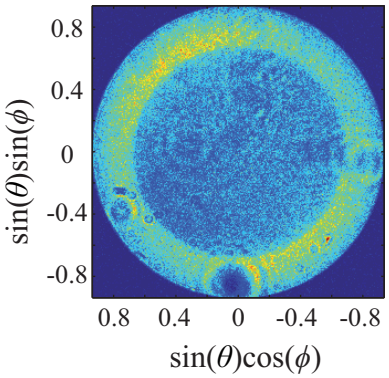

FIGURE 5.17: Emission pattern image measured from a rectangular nanoplatelet positioned on the glass substrate in contact with an oil objective as shematized in Figure 5.16(c).

5.4.2.3 Emission polarization analysis

Let us consider 2 linear dipoles d_1 and d_2 lying in the (x, y) plane, both of them have $\Theta_1 = \Theta_2 = \Theta = 90^o$; moreover, we assume that d_1 has $\Phi'_1 = \Phi + \pi/2$ then for the case of d_2, $\Phi'_2 = \Phi + \pi$, so that they are orthogonal.

As mentioned in the theoretical modelling, we could adjust the emitted photoluminescence signal as a function of the rotating polarization analyzing angle β as the followings:

$$P(\beta) = P_{min} + (P_{max} - P_{min}) \cos^2(\Phi' - \beta) \tag{5.6}$$

with an one dimensional dipole

$$P_{min} = A \sin^2 \Theta + B \cos^2 \Theta \tag{5.7}$$

$$P_{max} - P_{min} = C \sin^2 \Theta \tag{5.8}$$

where P_{min} and P_{max} stand for the minimum and maximum detected signals, and A, B, C could be calculated from the Fresnel reflective index (which is different in different cases of the interface configuration between the sample and the objective) and the numerical aperture of the objective.

In the case of an one dimensional dipole, $\Phi' = \Phi$, the detected intensity is maximum when the axis of polarization β is aligned with the axis of the dipole ($\beta = \Phi$). Since $\Theta = 90^o$, we could simplify $P(\beta) = A + C \cos^2(\Phi - \beta)$. Therefore, the total emitting power of the linear

dipole d_1 and d_2 respectively:

$$P_1(\beta) = \frac{1+ \mid \eta \mid}{2}\Big(A + C\ \sin^2(\Phi - \beta)\Big) \tag{5.9}$$

$$P_2(\beta) = \frac{1- \mid \eta \mid}{2}\Big(A + C\ \cos^2(\Phi - \beta)\Big) \tag{5.10}$$

where η denoting the dipolar asymmetric factor corresponding to the difference between two component dipoles d_1 and d_2.

Finally, the total signal detected from a two dimensional dipole consisting of two non-degenerate one dimensional dipoles:

$$\begin{aligned}\sum P &= P_1(\beta) + P_2(\beta) \\ &= \frac{1+ \mid \eta \mid}{2}[A + C\ \sin^2(\Phi - \beta)] + \frac{1- \mid \eta \mid}{2}[A + C\ \cos^2(\Phi - \beta)] \\ &= A + \frac{C}{2} - \frac{C \mid \eta \mid}{2}\cos[2(\Phi - \beta)]\end{aligned} \tag{5.11}$$

As $-1 \leq \cos[2(\Phi - \beta)] \leq 1$ and $0 \leq \mid \eta \mid$ we have:

$$P_{min} = A + \frac{C}{2} - \frac{C \mid \eta \mid}{2} \tag{5.12}$$

$$P_{max} = A + \frac{C}{2} + \frac{C \mid \eta \mid}{2} \tag{5.13}$$

The degree of the linear polarization is defined as:

$$\delta = \frac{P_{max} - P_{min}}{P_{max} + P_{min}} = \frac{C}{2A + C} \mid \eta \mid \tag{5.14}$$

This linear theoretical relation between the degree of polarization of the emission δ and the dipolar asymmetric factor η of the emitting dipole is plotted in Figure 5.18(b). For example, in the case of a rectangular nanoplatelet placed on the glass substrate in contact with an oil objective as schematized in Figure 5.18(a), we obtain the degree of polarization of its emission $\delta = 0.15$ from the polarimetric curve presented in Figure 5.18(c). Since $\dfrac{C}{2A + C} \approx 0.75$ for the air-glass interface, it implies that the factor $\eta = 0.2$.

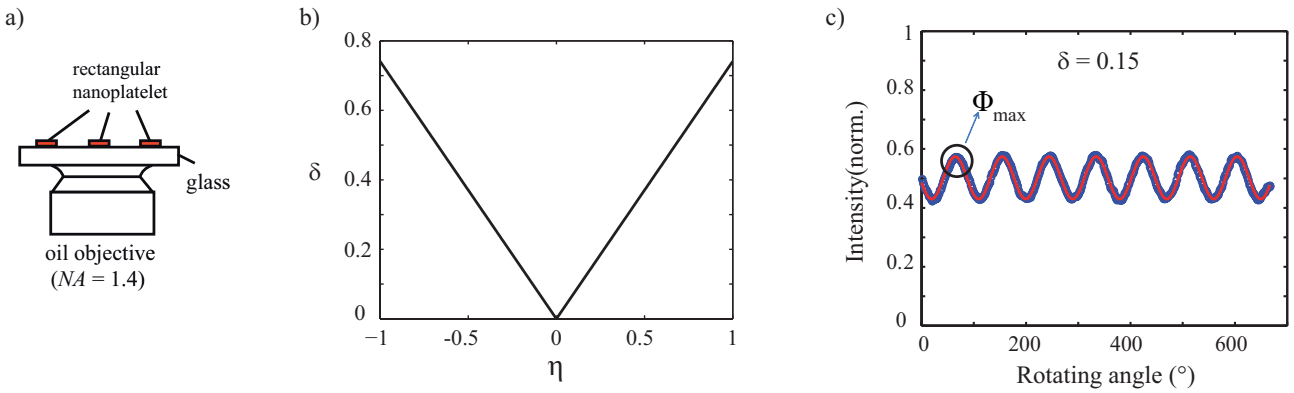

FIGURE 5.18: (a) Schematic of the investigated objective-sample configuration. (b) Theoretical relation between the emission degree of polarization δ and the dipolar asymmetric factor η calculated for the air-glass interface. (c) Emission polarimetric curve measured from a rectangular nanoplatelet at air-glass interface.

5.4.2.4 Comparison between Emission polarization analysis and Emission pattern analysis

Futhermore, it is possible to determine the dipolar asymmetric factor η from the emission pattern measurement. Characterizing an individual rectangular nanoplatelet at the air-glass interface as illustrated in Figure 5.18(a), we plot the experimental emission pattern (circles) and then compare with the data simulated with different values of η (solid lines) for a horizontal two dimensional dipole with in-plane orientation Φ_{max} (green) and $\Phi_{max} + 90^o$ (blue) in Figure 5.19 with Φ_{max} is estimated from the polarimetric curve shown in Figure 5.18(c).

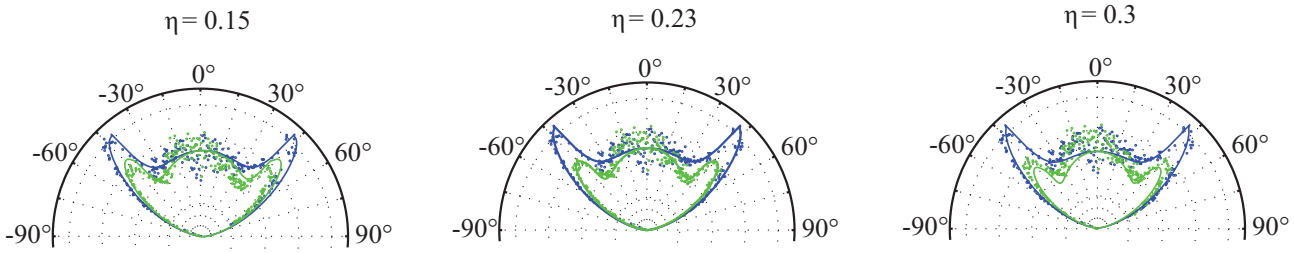

FIGURE 5.19: Comparison of the measured emission pattern (cirles) from a rectangular nanoplatelet and the calculated emission pattern (solid lines) with a two dimensional dipole oriented at $\Theta = 0$ and $\Phi = \Phi_{max}$ (extracted from the emission polarimetric curve of the same emitter) having the component strength ratio η along the direction of Φ_{max} (green) and $\Phi_{max} + 90^o$ (blue). The chosen configuration is the air-glass interface as illustrated in Figure 5.18(a).

The captured emission pattern is fitted the best when $\eta = 0.23$. This agreement confirms that the hyphothesis of the rectangular nanoplatelets being a sum of two orthorgonal component

dipoles with different osillator strengths fits quantitatively with the experimental data. And when $\eta < 0.15$ or $\eta > 0.3$, the fitting obiviously gets worse. The factor η for this emitter is then determined to be between 0.15 and 0.3. Thus, this fitting analysis could estimate a factor η with a uncertainty of ± 0.08. The accuracy is principally limited by the signal-to-noise ratio for the emission at small angles.

On the other hand, the factor η can also be determined by emission polarization measurements with the uncertanity of:

$$d\eta = \frac{2A + C}{C} d\delta(\Theta) \tag{5.15}$$

Since the uncertainty of the polarimetric measurements is $d\delta(\Theta) = 0.04$, we have $d\eta = 0.05$.

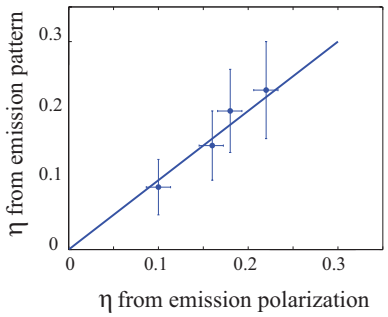

FIGURE 5.20: Comparison of the dipolar asymmetric factor η extracted from emission pattern measurement and from emission polarization measurement for 4 different rectangular nanoplatelets.

Figure 5.20 pictures the correspondance between the values of the dipolar asymmetric factor η extracted from emission polarization measurements (η is calculated from the experimental degree of polarization δ by Equation 5.22) and the values estimated by fitting analysis of the emission pattern for 4 different rectangular nanoplatelets. The linear function between two values confirms the correlation between two approaching ways in order to determine the dipolar orientation: emission polarimetric and emission pattern analysis.

5.4.3 Origin of the emission polarization

Further studies on a collection of rectangular nanoplatelets with different aspect ratios would give a more detailed idea of the mechanism by which the rectangular shape of the emitter influences on its emission polarization.

The value of the dipolar asymmetric factor η of 13 characterizing square emitters is calculated from their degree of polarization (Figure 5.11(a)) with $\frac{C}{2A + C} \approx 0.98$ for the PMMA-gold

interface as schematized in Figure 5.21(a). All the data obtained are smaller than 0.1. Their histogram is then prensented in Figure 5.21(b). We performed the same study with 18 rectangular nanoplatelets (Figure 5.15). The factor η in the case of rectangular nanoplatelets varies between 0.1 and 0.3, larger and wider comparing to square ones ($\eta < 0.1$), as shown in Figure 5.21(b) and (c).

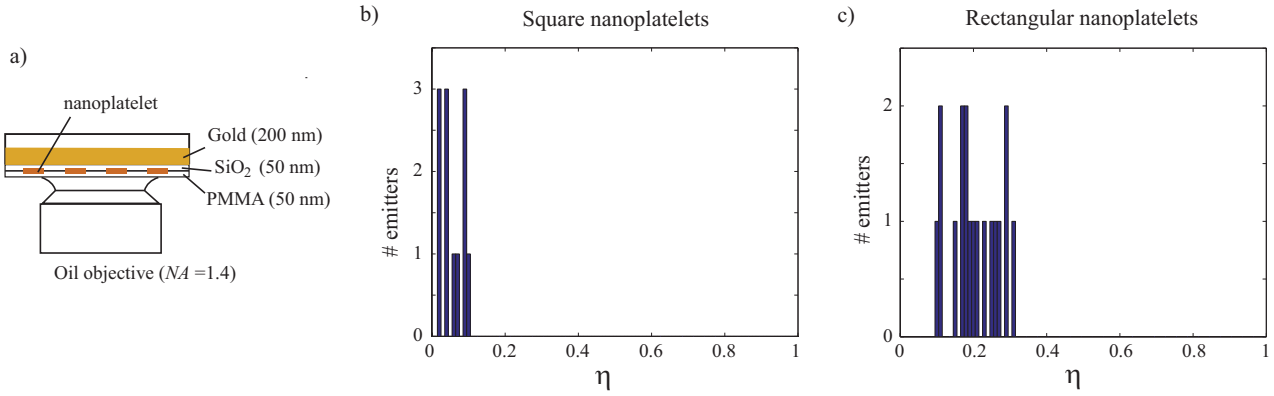

FIGURE 5.21: (a) Schematic of the investigated objective-sample configuration. Histogram of the dipolar asymmetric factor η measured for (b) 13 square platelets and (c) for 18 rectangular platelets.

When studying the square nanoplatelets, we obtain the dipolar asymmetric factor η in the range between 0 and 0.08, similarly to their size factor Δl histogrammed in Figure 5.6 (a). For the rectangular nanoplatelets, η varies from 0.1 to 0.3. These results are in a quantitative agreement with the corresponding histograms of the size factor Δl observed in Figure 5.6 (b). It should be noted that the group of investigated nanoplatelets are different in η and Δl histograms. Information on the size and morphology of the nanoplatelets provided by TEM images together with emission polarization measurements confirms the relation between the polarization state of the emission and the nanoplatelet′s shape. For square nanoplatelets, the emission is unpolarized and their emission pattern is symmetric while in the case of rectangles, there are polarized emision and asymmetric emission pattern.

However, since the thickness of both kinds of nanoplatelets are smaller than the exciton Bohr radius, the electron-hole pairs are confined in this dimension, so that the two other dimensions should not affect the emission (the electron-hole transition). Therefore, we have to understand the origin of the emission asymmetry (polarization and emission pattern). Our hypothesis is that the emitting dipole is modified by an optical effect. The fact that the nanoplatelet could be considered as a dielectric antenna brings an explanation about the origin of polarized emission of rectangular nanoplatelets: because of the large difference in indices between the nanostructure and the surrounding medium, the antenna effect would enhance the

emission along a given direction, resulting in changing the emission polarization and emission pattern. In the following lines, we will analyze and discuss this hypothesis.

Let us consider a point-like dipole emitter inside a dielectric structure of which three dimensions are the same as the nanoplatelet and its index of 2.59 (the index of CdSe bulk). We compare the emission pattern of two cases: an asymmetric two dimensional dipole ($\eta = 0.2$) inside a square nanoplatelet (15 x 15 x 2 nm^3) and a symmetric two dimensional dipole ($\eta = 0$) inside a rectangular nanoplatelet (20 x 15 x 2 nm^3), as shown in Figure 5.22. It should be noted that on the contrary to the former simulation of the emission pattern, our simulations here are done with a finite element numerical method which takes into account the dielectric difference between the nanoplatelet and its surrounding medium.

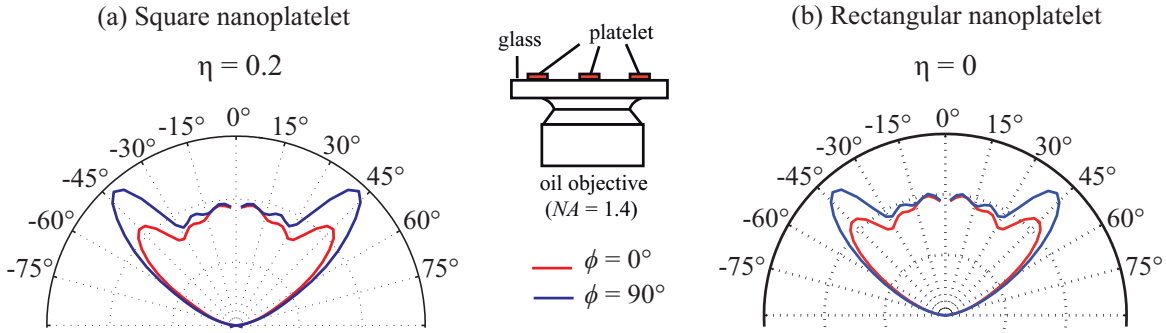

FIGURE 5.22: Comparison between calculated emission patterns (emitting along the direction of $\phi = 0^o$ lined in red while along $\phi = 90^o$ direction lined in blue) in the case of (a) square nanoplatelets (asymmetric two dimensional dipole $\eta = 0.2$) and (b) rectangular nanoplatelets (symmetric two dimensional dipole $\eta = 0$). We set the index of the nanoplatelets equal to 2.59 and perform simulations with the air-glass interface configuration as presented in Figure 5.16(c).

The chosen simulating configuration is the air-glass interface as schematized in Figure 5.16(c) where the emission is collected in the glass half-space. In the case of the asymmetric dipole inside the square nanoplatelet, there is stronger emission along the direction of $\phi = 90^o$ (the y reference axis), as observed in Figure 5.22(a). On the other hand, for the symmetric dipole in the rectangular nanoplatelet having the elongated shape along the x axis, the induced dielectric antenna effect is more confinement in the y dimension. The emission is thus enhanced along the y direction in far field.

The same asymmetric emssion observed in two considering cases addresses the conclusion that a rectangular nanoplatelet can be modelled as an asymmetric two dimensional dipole ($d_x \neq d_y$) without considering the surrounding medium or as a symmetric two dimensional dipole within a rectangular nanostructure of finite sizes. However, since the lateral size of

the nanoplatelets is much smaller than their exciton Bohr radius, the emitting dipole should not be sensitive to the size of nanoplatelets and then could be considered as a symmetric two dimensional dipole. Therefore, the polarized emission results from the dielectric antenna effect induced by the elongated shape of the rectangular nanoplatelets.

Moreover, the two dipolar dimensionality is in agreement with expected behaviors of an ideal thin quantum well. Since the thickness is much smaller than their exciton Bohr radius, the quantum confinement strongly happens along this direction, resulting in the separation between the heavy holes and light holes, therefore, emission only results from the recombination of electrons and heavy holes [28]. The electron-heavy holes has either ± 1 or ± 2 angular momentum [165], but only the degenerate ± 1 transitions are optically allowed so that it could contribute to the emission [166]. A two dimensional dipole can thus be described as a sum of two orthogonal linear dipoles which is equivalent to an incoherent sum of ± 1 transitions.

5.5 Cubic nanoplatelets

5.5.1 The emission polarization of the nanoplatelet dipole

The sample is prepared with the configuration as schematized in Figure 5.25(a): emitters are in PMMA half-space and at a distance of 50 nm to the PMMA-gold interface. The emission from an isolated cubic nanoplatelet is characterized in term of polarization analysis and emission pattern imaging, respectively. Since the nanoplatelet has cubic shape, the emitter lies randomly on the substrate either by its flat surface or its side face, as observed in TEM image in Figure 5.23(a). The average size of the cubic nanoplatelet is 16 x 16 x 10 nm^3, therefore, when it lies on its flat surface, it appears as a square in the TEM image. On the contrary, the one standing on its side face is presented as a rectangle with a thin string at the symmetric axis corresponding to the core nanoplatelet. These two positioning cases of the cubic nanoplatelets on the substrate induce two different polarization in the collected emission. Most nanoplatelets emit light which is much less polarized while there are some platelets giving highly polarized emission. Figure 5.24 shows the histogram of the the size ratio $\Delta\, l$ of their flat surfaces measured for 36 lying nanoplatelets. This distribution is similar with the data we obtain in the case of square nanoplatelets.

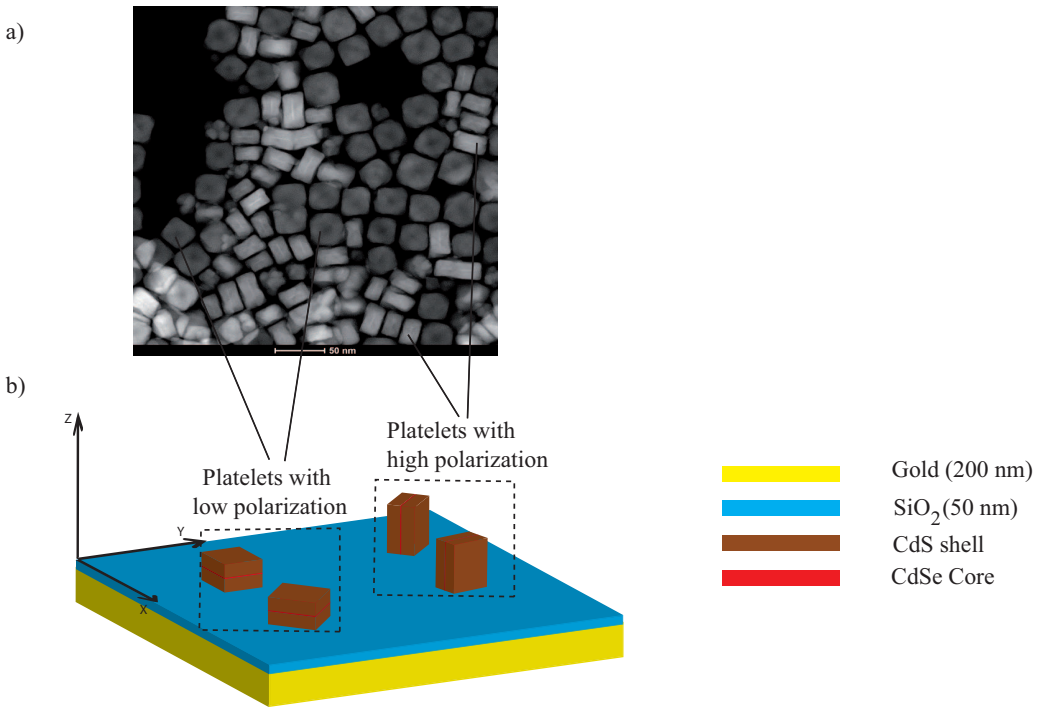

FIGURE 5.23: Cubic nanoplatelets: (a) TEM image and (b) the corresponding schematic representation of dipole positioning on the substrate. For the nanoplatelet lying on its flat surface, its emitting dipole is in the plane parallel to the substrate, appearing as a square in the TEM image and its emission is less polarized; while the nanoplatelet standing on its side face presents the core nanoplatelet perpendicular to the substrate, depicted as a rectangle in the TEM image with a thin string at the symmetric axis corresponding to the core nanoplatelet. It should be noted that the reference (x, y) plane is the substrate's plane.

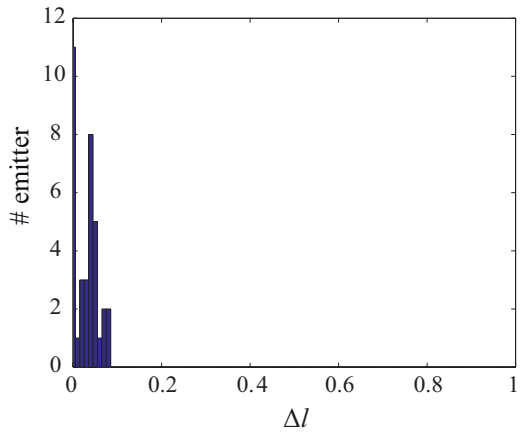

FIGURE 5.24: Histogram of the size ratio Δl of the flat surfaces measured for 36 lying cubic nanoplatelets in Figure 5.23(a).

5.5.2 Emission polarization analysis

5.5.2.1 Qualitative discussion

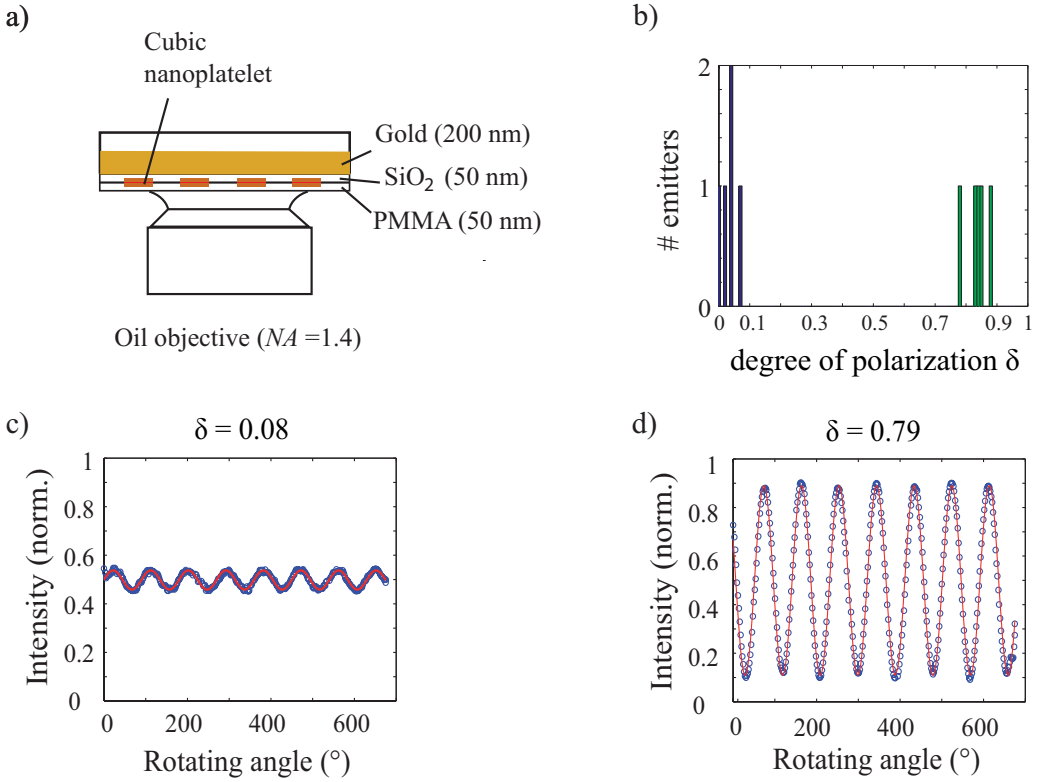

FIGURE 5.25: (a) Sechematic of the cubic nanoplatelets' configuration. (b) Histograms of the values of degree of polarization δ measured for 10 investigated nanoplatelets which either lie horizontally on the substrate (blue) or stand vertically on its side face (green). Polarimetric comparison of two emitters with very different emission polarization: (c) $\delta = 0.08$ and (d) $\delta = 0.79$.

For most investigated cubic nanoplatelets, their polarimetric curve, as displayed in Figure 5.25(c), are similar to the results of square platelets. Their degree of polarization (blue histogram bars in Figure 5.25(b)) vary from 0 to 0.08, referring to nearly unpolarized emission. It bring us to the idea that these emitters are horizontal two dimensional dipoles ($\Theta = 0$) and they lie by their flat surface on the substrate, like the square nanoplatelets.

On the other hand, there are some nanoplatelets of which the emission are much more polarized, with a degree of polarization δ in the range from 0.79 to 0.88, as displayed by green histogram bars in Figure 5.25(b). As discussed in Figure 5.9(c), when δ reaches its possible theoretical maximum value, the out-plane orientation Θ also gets close to its maximum

($\Theta \sim 90^o$). It indicates that the dipolar orientation is such that the two dimensional dipole would be composed of one linear dipole along the (x, y) plane and the other component dipole is oriented vertically to the (x, y) plane. Thus, the nanoplatelets stand by its side face as schematized in Figure 5.23(b). The in-plane orientation Φ_{max}, the direction along which the emission is polarized the most, randomly distributes in all directions. It should be noted that in the histogram of degree of polarization of cubic nanoplatelets presented in Figure 5.25(b), two cases of emitters with different positionings are chosen to be investigated, therefore, the proportion between two positioning cases is not representative for their distribution on the substrate. The lying nanoplatelets are far more probable than the standing one (about 90% of the emitters lying on the substrate).

5.5.2.2 Quatitative discussion

As shown in the TEM image in Figure 5.23(a) and its corresponding histogram in Figure 5.24, the lateral shape of the cubic nanoplatelets is not perfectly square but close to be rectangular ($0 \leq \Delta\, l \leq 0.08$). We have observed similar size distribution with the so-called 'square' nanoplatelets which present slightly elongated direction like rectangular one, as shown in Figure 5.6. In the case of rectangular emitters, we have developed a model for discussing the emission polarization by using 2 dipolar components $d_1 \neq d_2$ with $d_1 = \frac{d_0}{2}\sqrt{1+\eta}$ and $d_2 = \frac{d_0}{2}\sqrt{1-\eta}$ where η denoting the dipolar asymmetric factor ($-1 \leq \eta \leq 1$).

For the lying nanoplatelets, similar to the rectangular ones, we obtain the following equation (see subsection 5.4.2.3):

$$\delta_h = \frac{P_{max} - P_{min}}{P_{max} + P_{min}} = \frac{C}{2A + C} \mid \eta \mid \tag{5.16}$$

Similarly, we could consider in the case of standing platelets, their emitting dipole consists of d_1 lying in the (x, y) plane ($\Theta_1 = \pi/2$ and $\Phi'_1 = 0$) and d_2 normal to (x, y) plane ($\Theta_2 = 0$ and $\Phi'_2 = 0$).

Therefore, the total emitting power of the linear dipole d_1 and d_2 respectively:

$$P'_1(\beta) = \frac{1+\eta}{2}\left(A + C\,\cos^2(\beta)\right) \tag{5.17}$$

$$P'_2(\beta) = \frac{1-\eta}{2}\,B \tag{5.18}$$

Finally, the total signal detected from a two dimensional dipole consisting of two non-

degenerate one dimensional dipoles:

$$\begin{aligned}\sum P' &= P'_1(\beta) + P'_2(\beta) \\ &= \frac{1+\eta}{2}[A + C\,\cos^2(\beta)] + \frac{1-\eta}{2}B \\ &= \frac{1+\eta}{2}\,A + \frac{1-\eta}{2}\,B + \frac{C(1+\eta)}{2}\cos^2(\beta)\end{aligned} \tag{5.19}$$

As $0 \leq \cos^2(\Phi - \beta) \leq 1$, we have:

$$P'_{min} = \frac{1+\eta}{2}\,A + \frac{1-\eta}{2}\,B \tag{5.20}$$

$$P'_{max} = \frac{1+\eta}{2}\,A + \frac{1-\eta}{2}\,B + \frac{C(1+\eta)}{2} \tag{5.21}$$

The degree of the linear polarization is defined as:

$$\delta_v = \frac{P'_{max} - P'_{min}}{P'_{max} + P'_{min}} = \frac{C(1+\eta)}{(2A + 2B + C) + \eta(2A - 2B + C)} \tag{5.22}$$

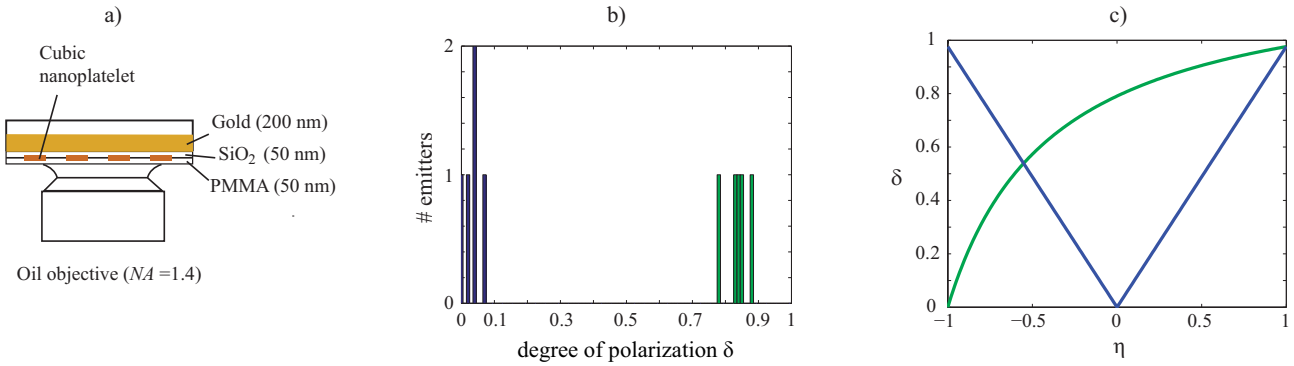

FIGURE 5.26: (a) Schematic of the investigated objective-sample configuration. (b) Histograms of the experimental values of degree of polarization δ measured for 10 investigated nanoplatelets which either lie horizontally on the substrate (blue) or stand vertically on its side face (green). (c) Theoretical relation between δ and the dipolar asymmetric factor η calculated for nanoplatelets at the distance of 50 nm to the PMMA-gold interface in two corresponding ways of positioning: lying (blue) and standing (green).

This linear theoretical relation between the emission′s degree of polarization of the cubic nanoplatelets δ_v and the corresponding dipolar asymmetric factor η of the emitting dipole is presented in Figure 5.26(c). As shown in Figure 5.26(a), the nanoplatelets are at the distance of 50 nm to the PMMA-gold interface ($n_1 = 1.5$ and $n_2 = 0.15 + 3.62i$), therefore, $A = 0.12$,

$B = 1.18$, and $C = 9.83$.

We now analyze the polarimetric results. For the lying nanoplatelets (blue), the experimentally obtained degree of polarization δ_h ranges from 0 to 0.08, referring to $0 \leq \mid \eta \mid \leq 0.08$. In the case of platelets standing on their side faces (green), we have the value of δ_v varies between 0.79 and 0.88. If the two dipolar components are the same $d_1 = d_2$ (corresponding to $\eta = 0$), we get $\delta_v = 0.79$. The result $\delta_v = 0.88$ leads to the factor $\eta = 0.36$. By taking into account the 5% of the uncertainty in the experimental measurement of δ, the factor η gets to 0.16. For the square nanoplatelets, the values of η is found to be between 0 and 0.1 while in the case of rectangular emitters, $0 \leq \eta \leq 0.3$. This distribution of η values is in agreement with the distribution of η we found for the lying cubic nanoplatelets, which have been approved by the similarity between the lateral shape distribution Figure 5.24 between the square nanoplatelets and the lying cubic ones.

We could wonder why we did not find less polarized nanoplatelets ($\delta < 0.79$) which corresponds to $d_2 > d_1$. This would imply that the nanoplatelets stand more on the short dimension than on the long one, which is a little bit more unlikely. Moreover, when $\eta > 0$, the degree of polarization δ varies much quickly with η than when $\eta < 0$. Therefore, a negative value of the dipolar asymetry (dipole standing on the short dimension) η would have a smaller effect on the degree of polarisation than when it is standing on the long one ($\eta > 0$) . This is another argument why the distribution of degree of polarisation is after 0.79. However, the statistic is very low to make a strong conclusion in this discussion.

5.5.3 Emission pattern analysis

For the first case of emission polarization as shown in Figure 5.27(c), the corresponding angular intensity distribution is isotropic with the most intense emission being at the center, which agrees well with the simulated emission pattern of the horizontal two dimensional diple. In the Fourier plane image captured for the other high polarized case (Figure 5.27(d)), two lobes located symetrically centered by the Φ_{max} direction. Therefore, this vertically positioning of cube nanoplatelets would give us an emission pattern with a preferred axis corresponding to a certain Φ_{max} direction which is straightforwardly estimated from the corresponding polarimetric curve (Figure 5.27(b)).

The comparison are performed between the recorded angular emission intensity distribution (plotted as cirles) of a cubic nanoplatelet dipole and the theoretical emission pattern (illustrated as solid lines) calculated for a two dimensional dipole oriented at (Θ, Φ_{max}) along

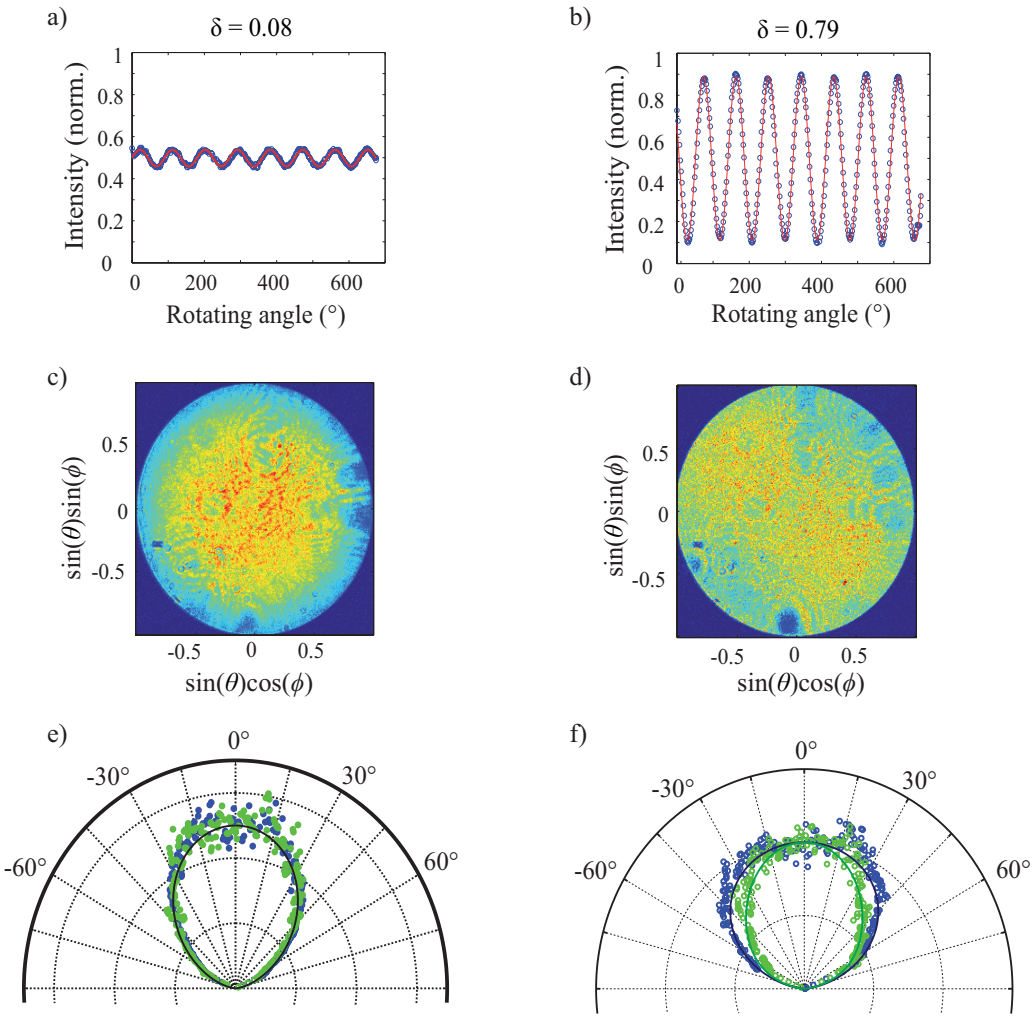

FIGURE 5.27: Comparison of two emitter with very different emission polarization in term of: (a) and (b) Polarimetric emission analysis, (c) and (d) Fourier plane image, (e) and (f) experimental (circles) and theoretical (solid lines) angular emission patterns along the in-plane orientation of Φ_{max} (green) and $\Phi_{max} + 90^o$ (blue).

plane of Φ_{max} (green) and $\Phi_{max} + 90°$(blue) with $\Theta = 0$ (the platelet′s flat surface is parallel to the sample plane) in Figure 5.25(e) and $\Theta = 90°$ (the platelet stands by its side: the core platelet is normal to the substrate) in Figure 5.25(f). The good agreements between the experimental and theoretical values confirm our interpretation of the cubic nanoplatelet′s positioning.

5.5.4 Further study of the dipolar dimensionality

5.5.4.1 Is there any third dipole involved in the emission?

For nanocrystals and nanoplatelets, the emission is generally modelized to be an one dimensional dipole or a two dimensional dipole which consists of two orthogonal linear dipolar components. However, some researchs state that a third dipole orthogonal to the plane of the two dimensional dipole could play a role in the emission [167, 168]. The geometry of the cubic nanoplatelets gives specific orientations to their emitting dipoles. Then the emission will be generated from a three dimensional dipole which would be a sum of two dipoles in the platelet plane and a linear dipole normal to the platelet plane. We could consider these two first dipolar components having the same oscillator strength. In the case of the platelets which stands on their side (their core plane is perpendicular to the substrate, as schematized in Figure 5.23), one of those dipoles is along z reference axis and the other is along the (x, y) plane. We assume that a third dipolar contribution exists with relative oscillator strength η_3 $(0 \leq \eta_3 \leq 1)$, oriented perpendicularly to the plane of the other two component dipoles (the core plane), thus it is also along the (x, y) plane, as presented in Figure 5.28. Moreover, as $d_3 = \eta_3 \, d_1$, when $\eta_3 = 1$ this third dipolar component is equivalent to the others while $\eta_3 = 0$ means there is no third dipole.

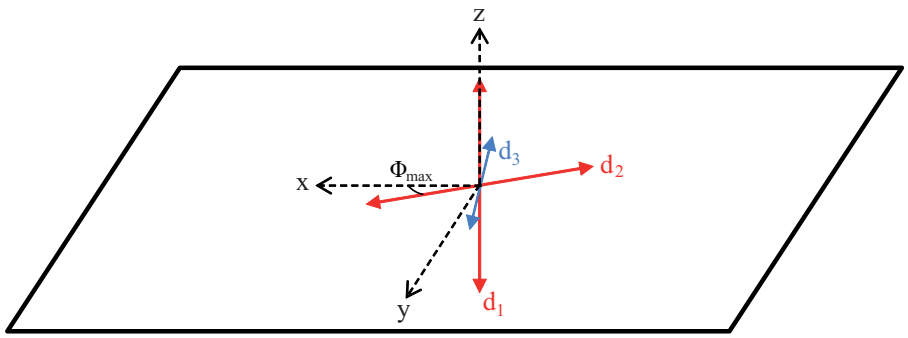

FIGURE 5.28: Schematic of the emitting dipole of a nanoplatelet standing by its side face.

5.5.4.2 Emission pattern analysis

We first analyze the data from the lying nanoplatelets in order to see if we could detect the presence of the third dipolar component. Figure 5.29(b) depicts theoretical emission pattern calculated for a symmetric horizontal two dimensional dipole. We compare it with the pattern simulated for a three dimensional dipole with $\eta_3 = 1$ as presented in Figure 5.29(c). In both cases, the emitter is at the distance of 50 nm to the PMMA-gold interface and its emission is collected in the PMMA half-space by an oil objective NA =1.4 , as schematized in Figure 5.29(a). These angular distributions are very similar to each other, so that lying cubic nanoplatelet do not help us to conclude about the presence of the third component of the emitting dipole.

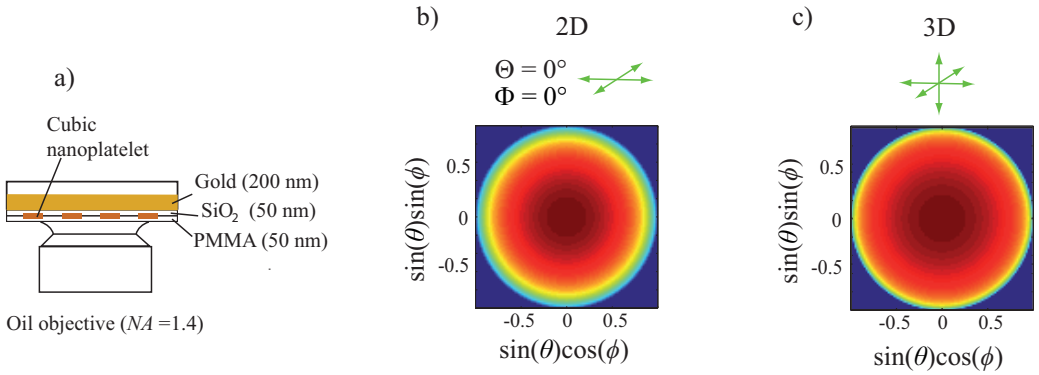

FIGURE 5.29: (a) Schematic of the investigated configuration. Simulated emission pattern of (b) a horizontal symmetric horizontal two dimensional dipole and (c) a three dimentional dipole with $\eta_3 = 1$.

We continue performing the emission pattern analysis on the data of the standing cubic nanoplatetets in the PMMA half-space 50 nm to the PMMA-gold interface (5.30(a)). We calculate the emission pattern of a three dimensional dipole with different values of η_3 and plot their profiles along the in-plane orientation $\Phi_{max} + 90^o$ (blue) and its orthorgonal axis Φ_{max} (green), as depicted in Figure 5.30(c). The experimental values are extracted from the recorded emission pattern presented in Figure 5.30(b). When $\eta_3 > 0.1$, there is a quantitative disagreement between the experimental and simulation data. We can conclude that the contribution of the third dipolar component, if it exists, is less than 10 % of the other dipoles.

5.5.4.3 Emission polarization analysis

Moreover, we could analyze the emission′ polarimetric curves which contains more quantitative details. We will consider now the experimental results. As stated for $d_1 = d_2$, the

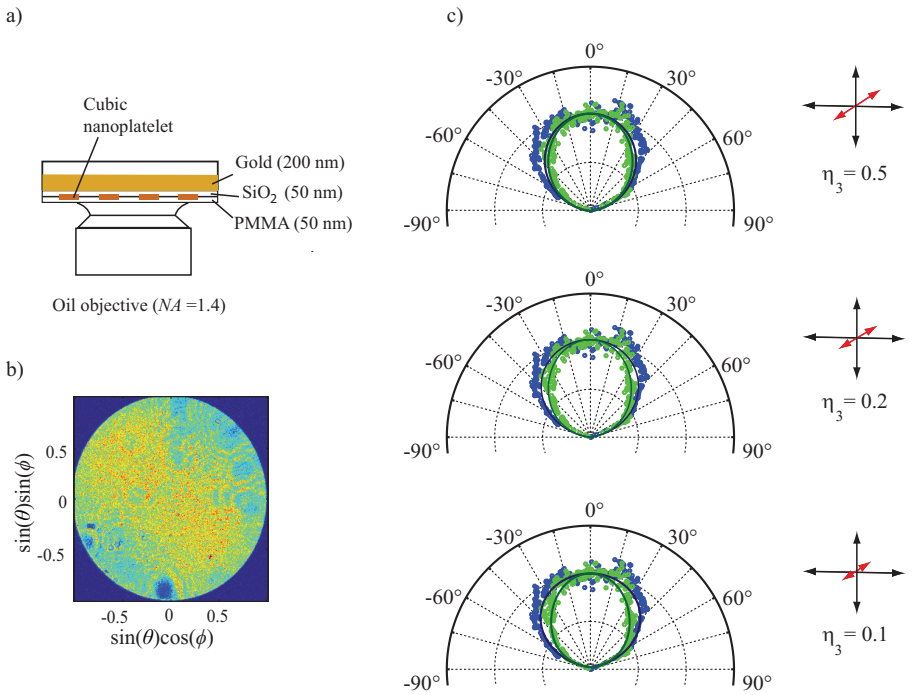

FIGURE 5.30: (a) Sechematic of the investigated configuration. (b) Experimental emission pattern of a cubic nanoplatelet having its core plane normal to the substrate (c) Comparison of emission patterns along the $\Phi_{max} + 90^o$ (blue) and Φ_{max} (green) directions: experimental values (dots) and simulated values (lines) with the amplitude of third dipolar component η_3 is 0.1, 0.2, and 0.5 respectively.

expected degree of polarization is 0.79. In our data, for one nanoplatelet we obtained $\delta = 0.79$. This is the one which has been discussed in the former emission pattern analysis.

As presented in Figure 5.28, this three dimensional dipole is considered as a combination of a two dimensional dipole of orientation $(\Theta = \pi/2, \Phi = \pi/2)$ which is a sum of two linear dipoles with the same amplitude, one along $(\Theta_1 = 0, \Phi_1 = 0)$ and the other oriented at $(\Theta_2 = \pi/2, \Phi_2 = \pi/2)$, and a third one dimensional dipole along $(\Theta_3 = \pi/2, \Phi = 0)$ of amplitude η_3 with respect to the 2 others. Thanks to Equation 5.6, we have P_1'', P_2'' and P_3'' being the total emitting power contributed by each dipolar components respectively:

$$P_1'' = B \tag{5.23}$$

$$P_2'' = A + C\ \sin^2(\beta) \tag{5.24}$$

$$P_3'' = \eta_3(A + C\ \cos^2(\beta)) \tag{5.25}$$

The total emission from the three dimensional dipole is thus:

$$\begin{aligned} \sum P'' &= P_1'' + P_2'' + P_3'' \\ &= B + A + C\sin^2(\beta) + \eta_3(A + C\ \cos^2(\beta)) \\ &= A(\eta_3 + 1) + B + C\eta_3 + C(1 - \eta_3)\sin^2(\beta) \end{aligned} \tag{5.26}$$

As $0 \leq \sin^2(\beta) \leq 1$ and $\eta_3 \leq 1$, we have:

$$P''_{min} = A(\eta_3 + 1) + B + C\eta_3 \tag{5.27}$$

$$P''_{max} = A(\eta_3 + 1) + B + C \tag{5.28}$$

The degree of polarization is defined as:

$$\delta = \frac{P''_{max} - P''_{min}}{P''_{max} + P''_{min}} = \frac{C(1 - \eta_3)}{2A(\eta_3 + 1) + 2B + C(\eta_3 + 1)} \tag{5.29}$$

Therefore,

$$d\delta = -\frac{d\eta_3}{1 - \eta_3} - \frac{(2A + C)d\eta_3}{2A(\eta_3 + 1) + 2B + C(\eta_3 + 1)} \tag{5.30}$$

The emitter with $\delta = 0.79$ $(d_1 = d_2)$ refers to $\eta_3 = 0$. But we need to take into account the uncertainty of δ measurement. Since $\eta_3 \approx 0$, we have:

$$d\delta = -d\eta_3 \frac{4A + 2B + 2C}{2A + 2B + C} \tag{5.31}$$

From the data of standing nanoplatelets, we have $d\delta = 0.05$, leading to $d\eta_3$ of 0.03. The polarimetric measurement allows us to detect the d_3 contribution up to $\eta_3 \geq 0.03$. It is thus concluded that the third dipole if any is less than 3% of the other dipoles.

Conclusion

We have studied the emission of an individual colloidal CdSe/CdS core/shell nanoplatelet. There are three types of geometric structure: square, rectangle and cube. The ultrathin nanoplatelets have two different shapes: square (16 x 16 x 2 nm^3) and rectangle (15 x 20 x 2 nm^3). The last type of investigated nanoplatelets are cubic (16 x 16 x 10 nm^3). In this chapter, we have applied our polarimetric method combined with emission pattern analysis to determine the emitting dipole of an individual nanoplatelet.

The square nanoplatelets are spincoated on SiO_2 covered gold subtrate then protected by PMMA layer and their emission is charaterized by an oil objective in contact with PMMA. For 13 studied square nanoplatelets, the emission polarization analysis confirms their unpolarized emission, resulting in two possible dipolar orientation depending on the one or two dipolar dimensionality of the emitting dipole. By comparing the calculating emission patterns obtained by our analytical model with the experimental images for these emitters, we have concluded that the emitting dipole of the nanoplatelets is a two dimensional dipole with its orientation along the z reference axis.

Analysis on the emission polarization of the rectangular nanoplatelets provides further insight into the emission of these platelets. We found much broader histogram of the degree of polarization which brought to us two different hypotheses for the dipolar orientation: a tilted dipole composed by two degenerate dipoles or a horizontal dipole composed by two non-degenerate dipoles. Using the configuration with only nanoplatelets on glass substrate and the oil objective introduced to the other side of the substrate, the measured Fourier plane image is possible to confirm the latter hypotheses.

The higher degree of polarization obtained by the emission polarization measurement is believed to relate to the elongated shape of these nanoplatelets. The good agreement on extracting the dipolar asymmetric factor from two experimental data set measured by two

different ways (emission polarization characterization and emission pattern imaging) confirm the correlation between two approaching ways. However, since the length of the nanoplatelets is much larger than their exciton Bohr radius, the emitting dipole should not be sensitive to the lateral sizes of nanoplatelets and then could be considered as a symmetric two dimensional dipole. In this case, the polarized emission will be explained by the dielectric antenna effect. The similarity between emission patterns simulated for an asymmetric two dimensional dipole inside a square nanoplatelet and for a symmetric two dimensional dipole inside a rectangular nanoplatelet confirms the antenna hypothesis.

For cubic nanoplatelets, the same two dipolar dimensionality was found. Most platelets were deposited horizontally on the substrate with their two dipolar components as well horizontal, similar to thin shell covered square nanoplatelets. However, in few cases when the nanoplatelets staying on its side face (the core platelet normal to the substrate), their two dimensional emitting dipole could be considered as having one component horizontal and the other vertical. We consider the possibility of a third dipolar component by analyzing the emission polarization and emission pattern in the case of high polarized emission. Since its contribution is absent or very small, we could conclude that the emitting dipole of these nanoplatelets is just two dimensional.

Chapter 6

Conclusion

In the stream of various studies to get an efficient source of single-photons, determination of the dipolar orientation of light from a nanoemitter is considered to be very important. Contribution of my thesis in the field is the development of a polarimetric method aiming at the analysis of a nanoemitter′s emitting dipole and its orientation. My work includes (i) proposing an analytical model, (ii) building-in the experiment setup and (iii) applying to determine the nanoemitter′s emitting dipole.

The model describes the emission of a dipole close to a plane interface in a wide range of realistic experimental conditions, including a very common case in plasmonics with a nanoemitter lying on gold film, the situation for which the more standard defocused imaging method is not sufficiently sensitive to provide reliable quantitative information on the emitting dipole′s orientation. With the same model, I did a computation on the emission diagram corresponding to the dipolar emission in far field for all the experimental conditions. By analyzing the emission′s polarization together with the emission pattern, I could accurately determine the three-dimensional orientation of an emitting dipole.

To build-in the experiment setup following the proposed model, I did firstly replacement of the sample by a well-determined polarized laser light, checking the optical function of necessary components such as the dichroic, the halfwave plate, the prism, etc. in the whole system to get the best and most facile conditions for measurement. The remarkable result obtained is that I could determine the dipolar orientation of a nanoemitter within 5% uncertainty. On the other hand, we succeed in conjugating the back focal plane onto the EM-CCD camera in order to image the emission pattern. By analyzing the emission pattern of the nanoemitter, we have a complementary method to estimate the dipolar dimensionality. Then the orientation of the

emitting dipole can be inferred by the polarimetric measurements.

Finally, I applied this combining method to investigate the semiconductor CdSe/CdS nanoplatelets with different geometric structures: thin square platelets, thin rectangular platelets, and cubic platelets. The agreement between the experimental data and the calculated simulation confirms the relevance of the method. I also established a relationship between the geometric structures of the platelets and the dipolar dimensionality and orientation of their associated emitting dipoles. For cubic CdSe/CdS nanoplatelets, we observed two different kinds of the dipolar orientation, parallel and perpendicular to the surface of the substrate. This is a good and promising case to develop the efficient combination of nanoemitter with nanoantennas.

For future works, the more kinds of geometric structures would be utilized to complete our theoretical explanation. Moreover, unlike the spherical CdSe nanocrystal which is weakly polarized and lack of defined orientation when locating on a substrate, the cubic nanoplatelets stayed on its side face with an emitting dipole oriented vertical to the substrate could be an interesting topic for the efficient coupling with next generation nanoantennas.

Appendix A

The polarization effect of the retardation induced by the setup

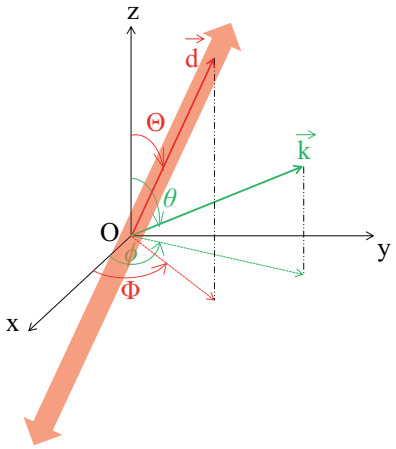

FIGURE A.1: Schemetic of an one dimensitional dipole with its orientation along $\vec{d}$ which is defined as (Θ, Φ) and the propagation vector $\vec{k}$ which is described by (θ_1, ϕ) in xyz reference coordinates.

In the xyz reference coordinates, we will consider an one dimensitional emitting dipole (Figure A.1) which is oriented with an out-plane angle Θ relative to the z axis (the polar angle) and an in-plane Φ relative to the x axis (the azimuthal angle) with the unit vector $\vec{u_s}$ and $\vec{u_p}$ along two orgothonal direction of polarization, respectively. These two unit vectors are perpendicular to the propagation vector $\vec{k}$ defined by a polar angle θ_1 and an azimuthal angle

ϕ in the xyz coordinates. We have:

$$\vec{u_s} = \begin{pmatrix} -sin\phi \\ cos\phi \\ 0 \end{pmatrix} \qquad \vec{u_p} = \begin{pmatrix} cos\theta_1\, cos\phi \\ cos\theta_1\, sin\phi \\ -sin\theta_1 \end{pmatrix}$$

The corresponding unit vectors $\vec{v_s}$ and $\vec{v_p}$ of the transmitted beam after passing through the setup (the output) will be thus defined as:

$$\vec{v_s} = \vec{u_s} \qquad \vec{v_p} = \begin{pmatrix} cos\phi \\ sin\phi \\ 0 \end{pmatrix}$$

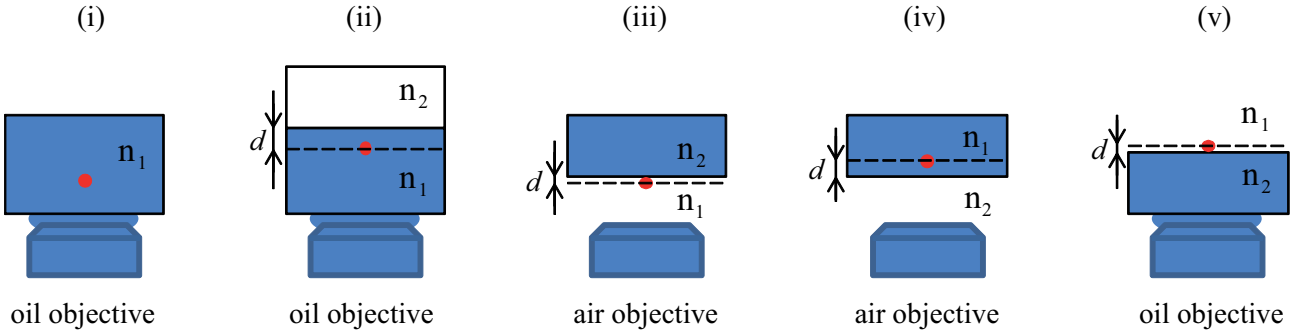

FIGURE A.2: (a) Schematic of the five cases corresponding to different experimental configurations between the sample and the objective, numbered from (i) to (v) with d being the distance from an emitter to the medium interface, n_1 denoting the index of the medium containing the emitter, and n_2 for the index of the other medium: (i) emitters in an homogeneous medium of n_1; (ii) emitters on a planar substrate of index n_1 and covered by a polymer layer with a thickness d of the same index while the upper medium of index $n_2 < n_1$; (iii) emitters at a distance d (with d tending towards 0) from a substrate with an index n_2 without any protecting layer while $n_1 = 1$ and (iv) emitters on a planar substrate with a polymer protecting layer of index n_1 while $n_2 = 1$; (v) emitters in the medium of index n_1 (as deposited at a distance d (with d tending towards 0) from a planar surface without the covering layer), observed by an oil objective of index $n_2 > n_1$ [27].

The expression of the electrical field of the beam exiting the setup is extracted from the thesis of Clotile Lethiec [27] for reflection configuration (ii) and (iii) schematized in Figure A.2

as the followings:

$$\boldsymbol{E} = \frac{D}{f}\sqrt{\frac{n_1}{cos\,\theta_1}}\Big[E_s(\theta_1,\phi)(1+r_s\,e^{i\Delta})\vec{v_s} + \Big(E_{p_a}(\theta_1,\phi)(1+r_p\,e^{i\Delta}) + E_{p_b}(\theta_1,\phi)(1-r_p\,e^{i\Delta})\Big)\vec{v_p}\Big] \tag{A.1}$$

with

$$E_s(\theta_1,\phi) = sin\Theta\,sin(\Phi-\phi) \tag{A.2}$$

$$E_{p_a}(\theta_1,\phi) = -sin\theta_1\,cos\Theta \tag{A.3}$$

$$E_{p_b}(\theta_1,\phi) = cos\theta_1\,sin\Theta\,cos(\Phi-\phi) \tag{A.4}$$

The emitting power collected after placing a polarizer with a rotating angle of β after the microscopy is also taken as:

$$P(\beta) = \int_{\theta_1=0}^{\theta_{1max}} D^2\,n_1\,sin\theta_1\,d\theta_1\int_{\phi=0}^{2\pi}\Big|E_s(\theta_1,\phi)(1+r_s\,e^{i\Delta})\vec{v_s}.\vec{u_\beta} + \Big(E_{p_a}(\theta_1,\phi)(1+r_p\,e^{i\Delta}) + E_{p_b}(\theta_1,\phi)(1-r_p\,e^{i\Delta})\Big)\vec{v_p}.\vec{u_\beta}\Big|^2 d\phi \tag{A.5}$$

where $\vec{u_\beta} = \begin{pmatrix} cos\beta \\ e^{i\psi}\,sin\beta \end{pmatrix}$ with ψ denoting the retardation induced by the setup.

We have:

$$\begin{aligned} E_s(\theta_1,\phi)(1+r_s\,e^{i\Delta})\vec{v_s}.\vec{u_\beta} &= sin\Theta\,sin(\Phi-\phi)\,(1+r_s\,e^{i\Delta})\,(-sin\phi\,cos\beta + e^{i\psi}\,cos\phi\,sin\beta) \\ &= \frac{sin\Theta}{2}\,(1+r_s\,e^{i\Delta})\,(-cos\beta(cos(\Phi-2\phi)-cos\Phi) + e^{i\psi}\,sin\beta(sin(\Phi-2\phi)+sin\Phi)) \end{aligned} \tag{A.6}$$

$$E_{p_a}(\theta_1,\phi)(1+r_p\,e^{i\Delta})\vec{v_p}.\vec{u_\beta} = -cos\Theta\,sin\theta_1\,(1+r_p\,e^{i\Delta})\,(-cos\beta\,cos\phi + e^{i\psi}\,sin\beta\,sin\phi) \tag{A.7}$$

$$E_{p_b}(\theta_1,\phi)(1-r_p\,e^{i\Delta})\vec{v_p}.\vec{u_\beta} = cos\theta_1\,sin\Theta\,cos(\Phi-\phi)\,(1-r_p\,e^{i\Delta})\,(-cos\beta\,cos\phi+e^{i\psi}\,sin\beta\,sin\phi)$$
$$= \frac{sin\Theta}{2}\,cos\theta_1\,(1-r_p\,e^{i\Delta})\,(cos\beta(cos(\Phi-2\phi)+cos\Phi)+e^{i\psi}\,sin\beta(-sin(\Phi-2\phi)+sin\Phi)) \tag{A.8}$$

Hence:

$$\begin{aligned} P(\beta) &= A\,sin^2\Theta + B\,cos^2\Theta + C\,sin^2\Theta|cos\beta\,cos\Phi + e^{i\psi}sin\beta\,sin\Phi|^2 \\ &= A\,sin^2\Theta + B\,cos^2\Theta + \frac{C}{2}\,sin^2\Theta(1+cos2\beta\,cos2\Phi + sin2\beta\,sin2\Phi\,cos\psi) \end{aligned} \tag{A.9}$$

with

$$A = \int_{\theta_1=0}^{\theta_{1max}} D^2\,\frac{\pi}{4}\,n_1\,|(1+r_s\,e^{i\Delta}) - cos\theta_1(1-r_p\,e^{i\Delta})|^2\,sin\theta_1\,d\theta_1 \tag{A.10}$$

$$B = \int_{\theta_1=0}^{\theta_{1max}} D^2\,\pi\,n_1\,|1+r_p\,e^{i\Delta})|^2\,sin^3\theta_1\,d\theta_1 \tag{A.11}$$

$$C = \int_{\theta_1=0}^{\theta_{1max}} D^2\,\frac{\pi}{2}\,n_1\,|1+r_s\,e^{i\Delta} + cos\theta_1(1-r_p\,e^{i\Delta})|^2\,sin\theta_1\,d\theta_1 \tag{A.12}$$

We define the measured value Φ_{mes} as:

$$tan2\Phi_{mes} = tan2\Phi\,cos\psi \tag{A.13}$$

Therefore, Equation A.9 becomes

$$P(\beta) = A\,sin^2\Theta + B\,cos^2\Theta + \frac{C}{2}\,sin^2\Theta(1+\frac{cos2\Phi}{cos2\Phi_{mes}}cos(2(\beta-\Phi_{mes})) \tag{A.14}$$

The degree of polarization is thus written as:

$$\delta_{mes} = \frac{P_{max}-P_{min}}{P_{max}+P_{min}} = \frac{Csin^2(\Theta)}{(2A-2B+C)sin^2(\Theta)+2B}\,\frac{cos2\Phi}{cos2\Phi_{mes}} \tag{A.15}$$

Finally, we conclude the relationship between δ_{mes} (the degree of polarization measured from the experiments by the realistic setup with a retardation of ψ) and $\delta(\Theta)$ (the actual degree of polarization of the emission from the dipole (the actual value we would obtain with a setup

without any retardation effect):

$$\delta_{mes} = \delta(\Theta)\frac{cos2\Phi}{cos2\Phi_{mes}} \tag{A.16}$$

These calculations could be applicable for the configuration (iv). The configuration (v) is more complicated and will not be treated here. The relation A.13 and A.16 can be as well straightforwardly applied to the case of a two dimensional dipole.

Bibliography

[1] C. J. Chunnilall, I. P. Degiovanni, S. Kuck, I. Muller, and A. G. Sinclair. Metrology of single-photon sources and detectors: a review. *Optical Engineering*, 53(8):081910, 2014.

[2] A. Kuhn and D. Ljunggren. Cavity-based single-photon sources. *Contemp. Phys.*, 51:289–313, 2010.

[3] T. E. Northup and R. Blatt. Quantum information transfer using photons. *Nat. Photon.*, 8:356–363, 2014.

[4] A. F. Koenderink, A. Alu, and A. Polman. Nanophotonics: shrinking light-based technology. *Science*, 348(6234):516–521, 2015.

[5] Z. H. Peng, S. E. de Graaf, J. S. Tsai, and O. V. Astafiev. Tuneable on-demand single-photon source in the microwave range. *Nat. Commun.*, 7:12588, 2016.

[6] I. Aharonovich, D. Englund, and M. Toth. Solid-state single-photon emitters. *Nat. Photon.*, 10(10):631–641, 2016.

[7] T. Grange, G. Hornecker, D. Hunger, J. P. Poizat, J. M. Gérard, P. Senellart, and A. Auffeves. Cavity-funneled generation of indistinguishable single photons from strongly dissipative quantum emitters. *Phys. Rev. Lett.*, 114(19):193601–193606, 2015.

[8] A. G. Curto, G. Volpe, T. H. Taminiau, M. P. Kreuzer, R. Quidant, and N. F. van Hulst. Unidirectional emission of a quantum dot coupled to a nanoantenna. *Science*, 329(5994):930–933, 2010.

[9] W. H. P. Pernice, C. Schuck, O. Minaeva, M. Li, G.N. Goltsman, A.V. Sergienko, and H.X. Tang. High-speed and high-efficiency travelling wave single-photon detectors embedded in nanophotonic circuits. *Nat. Commun.*, 3:1325, 2012.

[10] Y. M. He, Y. He, Y. J. Wei, D. Wu, M. Atature, C. Schneider, S. Hofling, M. Kamp, C. Y. Lu, and J. W. Pan. On-demand semiconductor single-photon source with near-unity indistinguishability. *Nat. Nano.*, 8(3):213–217, 2013.

[11] T. B. Hoang, G. M. Akselrod, and M. H. Mikkelsen. Ultrafast room-temperature single photon emission from quantum dots coupled to plasmonic nanocavities. *Nano Lett.*, 16(1):270–275, 2016.

[12] M. K. Akhlaghi, E. Schelew, and J. F. Young. Waveguide integrated superconducting single-photon detectors implemented as near-perfect absorbers of coherent radiation. *Nat. Commun*, 6:8233, 2015.

[13] M. Gaio, M. Moffa, M. Castro-Lopez, D. Pisignano, A. Camposeo, and R. Sapienza. Modal coupling of single photon emitters within nanofiber waveguides. *ACS Nano*, 10(6):6125–6130, 2016.

[14] , K. Słowik, J. Straubel, F. Lederer, R. Filter and Carsten Rockstuhl. Nanoantennas for ultrabright single photon sources. *Opt. Lett.*, 39(5):1246–1249, 2014.

[15] J. Straubel, R. Filter, C. Rockstuhl, and K. Słowik. Plasmonic nanoantenna based triggered single-photon source. *Phys. Rev. B.*, 93(19):195412–195423, 2016.

[16] C. Belacel, B. Habert, F. Bigourdan, F. Marquier, J. P. Hugonin, S. Michaelis de Vasconcellos, X. Lafosse, L. Coolen, C. Schwob, C. Javaux, B. Dubertret, J. J. Greffet, P. Senellart, and A. Maitre. Controlling spontaneous emission with plasmonic optical patch antennas. *Nano Lett.*, 13(4):1516–1521, 2013.

[17] L. Novotny and N. van Hulst. Antennas for light. *Nat. Photon.*, 5(2):83–90, 2011.

[18] F. Bigourdan, J. Paul. Hugonin, F. Marquier, C. Sauvan, and J. J. Greffet. Nanoantenna for electrical generation of surface plasmon polaritons. *Phys. Rev. Lett.*, 116(10):106803–106808, 2016.

[19] L. Lin and Y. Zheng. Optimizing plasmonic nanoantennas via coordinated multiple coupling. *Scientific Reports*, 5:14788, 2015.

[20] D. Vercruysse, Y. Sonnefraud, N. Verellen, F. B. Fuchs, G. Di Martino, L. Lagae, V. V. Moshchalkov, S. A. Maier, and P. Van Dorpe. Unidirectional side scattering of light by a single-element nanoantenna. *Nano Lett.*, 13(8):3843–3849, 2013.

[21] N. Liu, M. L. Tang, M. Hentschel, H. Giessen, and A. P. Alivisatos. Nanoantenna-enhanced gas sensing in a single tailored nanofocus. *Nat. Mater.*, 10(8):631–636, 2011.

[22] Y. Kim, C. Ippen, T. Greco, M. S. Oh, C. J. Han, J. Lee, A. Wedel, and J. Kim. Semitransparent quantum dot light-emitting diodes by cadmium-free colloidal quantum dots. *J. Nanosci. Nanotechnol.*, 14(11):8636–8640, 2014.

[23] J. Q. Grim, L. Mannaab, and I. Moreels. A sustainable future for photonic colloidal nanocrystals. *Chem. Soc. Rev.*, 44:5897–5914, 2015.

[24] M. Holzinger, A. Le Goff, and S. Cosnier. Nanomaterials for biosensing applications: a review. *Front. Chem.*, 2:63, 2014.

[25] S. Roy and Z. Gao. Nanostructure-based electrical biosensors. *Nanotoday*, 4(4):318–334, 2009.

[26] A. Dousse, L. Lanco, J. Suffczynski, E. Semenova, A. Miard, A. Lemaitre, I. Sagnes, C. Roblin, J. Bloch, and P. Senellart. Controlled light-matter coupling for a single quantum dot embedded in a pillar microcavity using far-field optical lithography. *Phys. Rev. Lett.*, 101(26):267404, 2008.

[27] C. Lethiec. Emission polarisee de nanoemetteurs; excitation de plasmons sur une surface metallique. *PhD Thesis of Pierre and Marie Curie University (University of Paris VI).*, 2014.

[28] S. Ithurria, M. D. Tessier, B. Mahler, R. P. S. M. Lobo, B. Dubertret, and A. L. Efros. Colloidal nanoplatelets with two-dimensional electronic structure. *Nat. Mater.*, 10:936–941, 2011.

[29] Z. Li, H. Qin, D. Guzun, M. Benamara, G. Salamo, and X. Peng. Uniform thickness and colloidal-stable cds quantum disks with tunable thickness: Synthesis and properties. *Nano Research*, 5(5):337–351, 2012.

[30] J. S. Son, K. Park, S. G. Kwon, J. Yang, M. K. Choi, J. Kim, J. H. Yu, J. Joo, and T. Hyeon. Dimension-controlled synthesis of cds nanocrystals: from 0d quantum dots to 2d nanoplates. *Small*, 8(15):2394–2402, 2012.

[31] R. Benchamekh, N. A. Gippius, J. Even, M. O. Nestoklon, J. M. Jancu, S. Ithurria, B. Dubertret, A. L. Efros, and P. Voisin. Tight-binding calculations of image-charge effects in colloidal nanoscale platelets of cdse. *Phys. Rev. B.*, 89(3):035307–035314, 2014.

[32] C. Bouet, M. D. Tessier, S. Ithurria, B. Mahler, B. Nadal, and B. Dubertret. Flat colloidal semiconductor nanoplatelets. *Chem. Matter.*, 25(8):1262–1271, 2013.

[33] Marvin Minsky. Memoir on inventing the confocal scanning microscope. *Scanning*, 10(4):128–138, 1988.

[34] C.A. Gehring, D. A. Williams, S. H. Cody, and R. W. Parish. Phototropism and geotropism in maize coleoptiles are spatially correlated with increases in cytosolic free calcium. *Nature*, 345(6275):528–530, 1990.

[35] T. R. Corle and G. S. Kino. Confocal scanning optical microscopy and related imaging systems. *New York: Academic Press*, 1996.

[36] H. Bach, A. Renn, and U. P. Wild. Spectral imaging of single molecules. *Single Mol.*, 1(1):73–77, 2000.

[37] E. J. G. Peterman, H. Sosa, and W. E. Moerner. Single-molecule fluorescence spectroscopy and microscopy of biomolecular motors. *Ann. Rev. Phys. Chem.*, 55:79–96, 2004.

[38] P. Bharadwaj, B. Deutsch, and L. Novotny. Optical antennas. *Adv. Opt. Photonics*, 1(3):438–483, 1996.

[39] T. V. Raziman and O. J. F. Martin. Orientation dependence of plasmonically enhanced spontaneous emission. *J. Phys. Chem. C*, 120(37):21037–21046, 2016.

[40] X. Brokmann, M. V. Ehrensperger, J. P. Hermier, A. Triller, and M. Dahan. Orientational imaging and tracking of single cdse nanocrystals by defocused microscopy. *Chem. Phys. Lett.*, 406(1-3):210–214, 2005.

[41] J. J. Macklin, J. K. Trautman, T. D. Harris, and L. E. Brus. Imaging and time-resolved spectroscopy of single molecules at an interface. *Science*, 272(5259):255–258, 1996.

[42] C. Vion, P. Spinicelli, L. Coolen, C. Barthou, J.M. Frigerio, J.P. Hermier, and A. Maitre. Controlled modification of single colloidal cdse/zns quantum dots fluorescence through interactions with gold surface plasmons. *Opt. Express*, 18(7):7440–7455, 2010.

[43] A. Badolato, K. Hennessy, M. Atature, J. Dreiser, E. Hu, P. M. Petroff, and A. Imamoglu. Deterministic coupling of single quantum dots to single nanocavity modes. *Science*, 308(5725):1158–1161, 2005.

[44] O. Gazzanov, S. Michaelis de Vasconcellos, K. Gauthron, C. Symonds, J. Bloch, P. Voisin, J. Bellessa, A. Lemaitre, and P. Senellart. Evidence for confined tamm plasmon modes under metallic microdisks and application to the control of spontaneous optical emission. *Phys. Rev. Lett.*, 107(24):247402–247407, 2011.

[45] K. Hennessy, C. Hoogerle, E. Hu, A. Badolato, and A. Imamoglu. Tuning photonic nanocavities by atomic force microscope nano-oxidation. *Appl. Phys. Lett.*, 89(4):041118–041121, 2006.

[46] F. Pagliano, Y. J. Cho, T. Xia, F. van Otten, R. Johne, and A. Fiore. Dynamically controlling the emission of single excitons in photonic crystal cavities. *Nature Communications*, 5:5786/1–6, 2014.

[47] X. Brokmann, M. V. Ehrensperger, J. P. Hermier, A. Triller, and M. Dahan. Orientational imaging and tracking of single cdse nanocrystals by defocused microscopy. *Chem. Phys. Lett.*, 406(1-3):210–214, 2005.

[48] E. Toprak, J. Enderlein, S. Syed, S. A. McKinney, R. G. Petschek, T. Ha, Y. E. Goldman, and P. R. Selvin. Defocused orientation and position imaging (dopi) of myosin v. *Proc. Natl. Acad. Sci. U.S.A.*, 103(17):6495–6499, 2006.

[49] A. P. Bartko and R. M. Dickson. Imaging three-dimensional single molecule orientations. *J. Phys. Chem. B*, 103(51):11237–11241, 1999.

[50] S. A. Empedocles, R. Neuhauser, and M. G. Bawendi. Three-dimensional orientation measurements of symmetric single chromophores using polarization microscopy. *Nature*, 399:126–130, 1999.

[51] J. T. Fourkas. Rapid determination of the three-dimensional orientation of single molecules. *Opt. Lett.*, 26(4):211–213, 2001.

[52] C. Lethiec, J. Laverdant, H. Vallon, C. Javaux, B. Dubertret, J. M. Frigerio, C. Schwob, L. Coolen, and A. Maitre. Measurement of three-dimensional dipole orientation of a single fluorescent nanoemitter by emission polarization analysis. *Phys. Rev. X*, 4(2):021037–021049, 2014.

[53] T. Ha, Th. Enderle, D. S. Chemla, P. R. Selvin, and S. Weisss. Single molecule dynamics studied by polarization modulation. *Phys. Rev. Lett.*, 77(19):3979–3982, 1996.

[54] D. Goorskey, M. Xiao, Z. A. Peng, X. Chen, A. Nazzal, and X. Pengi. Polarization spectroscopy of single cdse quantum rods. *Phys. Rev. B*, 64(24):245304–245308, 2001.

[55] P. Spinicelli, A. Fiore, J. P. Hermier, L. Manna, R. Cingolani, E. Giacobino, M. De Vittorio, F. Pisanello, L. Martiradonna, and A. Bramati. Dots-in-rods as polarized single photon sources. *Superlattices and Microstructures*, 47(1):165–169, 2010.

[56] G. Menagen A. Sitt, A. Salant, and U. Banin. Highly emissive nano rod-in-rod heterostructures with strong linear polarization. *Nano Lett.*, 11(6):2054–2060, 2011.

[57] A. Sitt, A. Faust, I. Hadar, G. B. Hitin, and U. Banin. Polarization properties of semiconductor nanorod heterostructures: from single particles to the ensemble. *J. Phys. Chem. Lett.*, 4(3):502–507, 2013.

[58] I. Chung, K. T. Shimizu, and M. G. Bawendi. Room temperature measurements of the 3d orientation of single cdse quantum dots using polarization microscopy. *Proc. Natl. Acad. Sci. U.S.A.*, 100(2):405–407, 2003.

[59] X. Brokmann, L. Coolen, M. Dahan, and J. P. Hermier. Measurement of the radiative and nonradiative decay rates of single cdse nanocrystals through a controlled modification of their spontaneous emission. *Phys. Rev. Lett.*, 93(10):107403–107407, 2004.

[60] R. Pariser. Theory of the electronic spectra and structure of the polyacenes and of alternant hydrocarbons. *J. Chem. Phys.*, 24(2):250–268, 1956.

[61] R. J. Epstein, F. M. Mendoza, Y. K. Kato, and D. D. Awschalom. Anisotropic interactions of a single spin and dark-spin spectroscopy in diamond. *Nat. Phys.*, 1:94–98, 2005.

[62] C. Lethiec, F. Pisanello, L. Carbone, A. Bramati, L. Coolen, and A. Maitre. Polarimetry-based analysis of dipolar transitions of single colloidal cdse/cds dot-in-rods. *New J. Phys.*, 16(9):093014–021033, 2014.

[63] R. T. Holm, S. W. McKnight, E. D. Palik, and W. Lukosz. Interference effects in luminescence studies of thin films. *Appl. Opt.*, 21(14):2512–2519, 1982.

[64] W. Lukosz. Light emission by multipole sources in thin layers. i. radiation patterns of electric and magnetic dipoles. *J. Opt. Soc. Am.*, 71(6):744–755, 1981.

[65] R. M. A. Azzam and N. M. Bashara. Ellipsometry and polarized light. *North-Holland, Amsterdam*, 1979.

[66] W. A. Shurcliff. Polarized light. *Harvard U. Press, Cambridge*, 1962.

[67] S. Y. Lu and R. Chipman. Interpretation of the mueller matrices based on polar decomposition. *J. Opt. Soc. Am. A*, 13(5):1106–1113, 1996.

[68] S. Y. Lu and R. Chipman. Homogeneous and inhomogeneous jones matrices. *J. Opt. Soc. Am. A*, 11(2):766–773, 1994.

[69] S. N Savenko, O. I. Sydoruk, and R. S. Muttiah. Conditions for polarization elements to be dichroic and birefringent. *J. Opt. Soc. Am. A*, 22(7):1447–1452, 2005.

[70] R. Caputo, I. Trebisacce, L. De Sio, and C. Umeton. Jones matrix analysis of dichroic phase retarders realized in soft matter composite materials. *Opt. Express*, 18(6):5776–5784, 2010.

[71] R. C. Jones. A new calculus for the treatment of optical systems. i. description and discussion of the calculus. *J. Opt. Soc. Am.*, 31:488–493, 1941.

[72] H. Hurwitz and R. C. Jones. A new calculus for the treatment of optical systems. ii. proof of three general equivalence theorems. *J. Opt. Soc. Am.*, 31:493–495, 1941.

[73] R. C. Jones. A new calculus for the treatment of optical systems. iii. the sohncke theory of optical activity. *J. Opt. Soc. Am.*, 31:500–503, 1941.

[74] R. C. Jones. A new calculus for the treatment of optical systems. iv. *J. Opt. Soc. Am.*, 32:486–493, 1942.

[75] R. C. Jones. A new calculus for the treatment of optical systems. v. a more general formulation, and description of another calculus. *J. Opt. Soc. Am.*, 37:107–110, 1947.

[76] R. C. Jones. A new calculus for the treatment of optical systems. vi. experimental determination of the matrix. *J. Opt. Soc. Am.*, 37:110–112, 1947.

[77] R. C. Jones. A new calculus for the treatment of optical systems. vii. properties of the n-matrices. *J. Opt. Soc. Am.*, 38:671–683, 1948.

[78] R. C. Jones. A new calculus for the treatment of optical systems. viii. electromagnetic theory. *J. Opt. Soc. Am.*, 46:126–131, 1956.

[79] D. H. Goldstein. Polarized light. *CRC Press*, third ed., 2011.

[80] Specification of the achromatic waveplates. *Thorlab homepage.*

[81] Specification of the dichroic beamsplitter ff510-di01. *Semrock homepage.*

[82] J. Zenneck. Fortpflanzung ebener elektromagnetischer wellen langs einer ebenen leiterflache. *Ann. d. Physik.*, 23:846–866, 1907.

[83] A. Sommerfeld. Uber die ausbreitung der wellen in der drahtlosen telegraphie. *Ann. d. Physik.*, 28:665–736, 1909.

[84] H. v. Horschelmann. Uber die wirkungsweise des geknickten marconischen senders in der drahtlosen telegraphie. *Jb. drahtl. Telegr. u. Teleph.*, 5:14–34 and 188–211, 1911.

[85] H. Weyl. Ausbreitung elektromagnetischer wellen ¨uber einem ebenen leiter. *Ann. d. Physik.*, 60:481–500, 1919.

[86] A. Sommerfeld. Uber die ausbreitung der wellen in der drahtlosen telegraphie. *Ann. d. Physik.*, 81:1135–1153, 1926.

[87] M. J. O. Strutt. Strahlung von antennen unter dem einfluss der erdbodeneigenschaften. *Ann. d. Physik.*, 1:721–772, 1929.

[88] B. V. der Pol and K. F. Niessen. Uber die ausbreitung elektromagnetischer wellen uber einer ebenen erde. *Ann. d. Physik.*, 6:273–294, 1930.

[89] A. Sommerfeld. Partial differential equations in physics. *New York: Academic Press.*, (5th ed.), 1967.

[90] G. S. Agarwal. Quantum electrodynamics in the presence of dielectrics and conductors. i. electrodynamic-field response functions and black-body fluctuations in finite geometries. *Phys. Rev. A*, 11(1):230–242, 1975.

[91] W. Lukosz and R. E. Kunz. Light emission by magnetic and electric dipoles close to a plane interface. i. total radiated power. *J. Opt. Soc. Am.*, 67(12):1607–1615, 1977.

[92] W. Lukosz. Light emission by magnetic and electric dipoles close to a plane dielectric interface. iii. radiation patterns of dipoles with arbitrary orientation. *J. Opt. Soc. Am.*, 69(11):1495–1503, 1979.

[93] E. H. Hellen and D. Axelrod. Fluorescence emission at dielectric and metal-film interfaces. *J. Opt. Soc. Am. B*, 4(3):337–350, 1987.

[94] L. Novotny and B. Hecht. Principles of nano-optics. *Cambridge University Press*, 2006.

[95] M. A. Lieb, J. M. Zavislan, and L. Novotny. Single-molecule orientations determined by direct emission pattern imaging. *J. Opt. Soc. Am. B*, 21(6):1210–1215, 2004.

[96] M. R. Foreman, C. M. Romero, and P. Torok. Determination of the three-dimensional orientation of single molecules. *Optic Letters*, 33(9):1020–1022, 2008.

[97] D. Zhang, R. Badugu, Y. Chen, S. Yu, P. Yao, P. Wang, H. Ming, and J.R. Lakowicz. Back focal plane imaging of directional emission from dye molecules coupled to one-dimensional photonic crystals. *Nanotechnology*, 25(14):145202–154212, 2014.

[98] F. Feng. Coupling between optical tamm states and fluorescent nanocrystals; determination of the dipole nature of single colloidal nanoplatelets. *PhD Thesis of Pierre and Marie Curie University (University of Paris VI).*, 2016.

[99] L. Novotny. Allowed and forbidden light in near-field optics. i. a single dipolar light source. *J. Opt. Soc. Am. A*, 14(1):191–104, 1997.

[100] C. B. Murray, D. J. Norris , and M. G. Bawendi. Synthesis and characterization of nearly monodisperse cde (e = sulfur, selenium, tellurium) semiconductor nanocrystallites. *J. Am. Chem. Soc.*, 115(19):8706–8715, 1993.

[101] Andrey Rogach. Quantum dots still shining strong 30 years on. *ACS Nano*, 8(7):6511–6512, 2014.

[102] D. V. Talapin, J. S. Lee, M. V. Kovalenko, and E. V. Shevchenko. Prospects of colloidal nanocrystals for electronic and optoelectronic applications. *Chem. Rev.*, 501(3-5):75–221, 2011.

[103] R. Krahne, G. Morello, A. Figuerola,C. George, S. Deka, and L. Manna. Physical properties of elongated inorganic nanoparticles. *Phys. Rep.*, 1996.

[104] M. A. Boles, D. Ling, T. Hyeon, and D.V. Talapin. The surface science of nanocrystals. *Nat. Mater.*, 15:141–153, 2016.

[105] X. G. Peng, L. Manna, W. D. Yang, J. Wickham, E. Scher, A. Kadavanich, and A. P. Alivisators. Shape control of cdse nanocrystals. *Nature*, 404(6773):59–61, 2000.

[106] J. J. Ning, K. K. Men, G. J. Xiao, L. Wang, Q. Q. Dai, B. Zou, B. B. Liu, and G. T. Zou. Facile synthesis of iv-vi sns nanocrystals with shape and size control: Nanoparticles, nanoflowers and amorphous nanosheets. *Nanoscale*, 2(9):1699–1703, 2010.

[107] G. J. Xiao, Y. Zeng, Y. Y. Jiang, J. J. Ning, W. T. Zheng, B. B. Liu, X. D. Chen, G. T. Zou, and B. Zou. Controlled synthesis of hollow $cu_{2-x}te$ nanocrystals based on the kirkendall effect and their enhanced co gas-sensing properties. *small*, 9(5):793–799, 2013.

[108] G. J. Xiao, Y. N. Wang, J. J. Ning, Y. J. Wei, B. B. Liu, W. W. Yu, G. T. Zou, and B. Zou. Recent advances in iv-vi semiconductor nanocrystals: synthesis, mechanism, and applications. *RSC Adv.*, 3(22):8104–8130, 2013.

[109] K. S. Jeong and P. Guyot-Sionnest. Mid-infrared photoluminescence of cds and cdse colloidal quantum dots. *ACS Nano*, 10(2):2225–2231, 2016.

[110] X. J. Wu, J. Chen, C. Tan, Y. Zhu, Y. Han, and H. Zhang. Controlled modification of single colloidal cdse/zns quantum dots fluorescence through interactions with gold surface plasmons. *Nat. Chem.*, 8:470–475, 2016.

[111] D. D. Vaughn II, R. J. Patel, M. A. Hickner, and R. E. Schaak. Single-crystal colloidal nanosheets of ges and gese. *J. Am. Chem. Soc.*, 132(43):15170–15172, 2010.

[112] J. Joo, J. S. Son, S. G. Kwon, J. H. Yu, and T. Hyeon. Low-temperature solution-phase synthesis of quantum well structured cdse nanoribbons. *J. Am. Chem. Soc.*, 128(17):5632–5633, 2006.

[113] J. A. Rogers, M. G. Lagally, and R. G. Nuzzo. Synthesis, assembly and applications of semiconductor nanomembranes. *Nature*, 477(7362):45–53, 2011.

[114] A. Nieto,, D. Lahiri,, and A. Agarwal. Synthesis and properties of bulk graphene nanoplatelets consolidated by spark plasma sintering. *Carbon*, 50(11):4068–4077, 2012.

[115] P. Tyagi, S. M. Arveson, and W. A. Tisdale. Colloidal organohalide perovskite nanoplatelets exhibiting quantum confinement. *J. Phys. Chem. Lett.*, 6(10):1911–1916, 2015.

[116] S. Ithurria and B. Dubertret. Quasi 2d colloidal cdse platelets with thicknesses controlled at the atomic level. *J. Am. Chem. Soc.*, 130(49):16504–16505, 2008.

[117] M. D. Tessier, B. Mahler, B. Nadal, H. Heuclin, S. Pedetti, and B. Dubertret. Spectroscopy of colloidal semiconductor core/shell nanoplatelets with high quantum yield. *Nano Lett.*, 13(7):3321–3326, 2013.

[118] C. Boet, D. Laufer, B. Mahler, B. Nadal, H. Heuclin, S. Pedetti, G. Patriarche, and B. Dubertret. Synthesis of zinc and lead chalcogenide core and core/shell nanoplatelets using sequential cation exchange reactions. *Chem. Mater.*, 26(9):3002–3008, 2014.

[119] J. R. Murphy, S. Delikanli, T. Scrace, P. Zhang, T. Norden, T. Thomay, A. N. Cartwright1, H. V. Demir, and A. Petrou. Three-dimensional orientation measurements of symmetric single chromophores using polarization microscopy. *App. Phys. Lett.*, 108(26):242406, 2016.

[120] D. K. Kim, Y. Lai, B. T. Diroll, C. B. Murray, and C. R. Kagan. Flexible and low-voltage integrated circuits constructed from high-performance nanocrystal transistors. *Nat. Commun.*, 3:1216, 2012.

[121] Y.J. Doh, K. N. Maher, L. Ouyang, C. L. Yu, H. Park, and J. Park. Electrically driven light emission from individual cdse nanowires. *Nano Lett.*, 8(12):4552–4556, 2008.

[122] T. Ayvazian, W. E. van der Veer, W. Xing, W. Yan, and R. M. Penner. Electroluminescent, polycrystalline cadmium selenide nanowire arrays. *ACS Nano*, 7(10):9569–9479, 2013.

[123] I. Gur, N. A. Fromer, M. L. Geier, and A. P. Alivisatos. Air-stable all-inorganic nanocrystal solar cells processed from solution. *Science*, 310(5747):462–465, 2005.

[124] W. U. Huynh, J. J. Dittmer, and A. P. Alivisatos. Hybrid nanorod-polymer solar cells. *Science*, 295(5564):2425–2427, 2002.

[125] J. Li, C. Meng, Y. Liu, X. Wu, Y. Lu, Y. Ye, L. Dai, L. Tong, X. Liu, and Q. Yang. Wavelength tunable cdse nanowire lasers based on the absorption-emission-absorption process. *Adv. Mater.*, 25(6):833–837, 2013.

[126] J. Yang, H. Tang, Y. Zhao, Y. Zhang, J. Li, Z. Ni, Y. Chena, and D. Xu. Thermal conductivity of zinc blende and wurtzite cdse nanostructures. *Nanoscale*, 7(38):16071–16078, 2015.

[127] B. I. Greene, J. Ornstein, and S. Schmitt-Rink. All-optical nonlinearities in organics. *Science*, 247(4943):679–687, 1990.

[128] V. M. Agranovich and G. F. Bassani. Electronic excitations in organic based nanostructures. *Elsevier*, 1st ed., 2003.

[129] H. M. Gibbs. Optical bistability: Controling light with light. *Academic Press*, New York, 1985.

[130] T. Tani. Photographic sensitivity. *Oxford University Press*, Oxford, 1995.

[131] H. van Amerongen, L. Valkunas, and R. van Grondelle. Photosynthetic excitons. *World Scientific*, Singapore, 2000.

[132] D. J. Norris, A. Sacra, C. B. Murray, and M. G. Bawendi. Measurement of the size dependent hole spectrum in cdse quantum dots. *Phys. Rev. Lett.*, 72(16):2612–2615, 1994.

[133] A. P. Alivisatos. Perspectives on the physical chemistry of semiconductor nanocrystals. *J. Phys. Chem.*, 100(31):13226–13239, 1996.

[134] D. C. Oertel, M. G. Bawendi, A. C. Arango, and V. Bulovic. Photodetectors based on treated cdse quantum-dot films. *Appl. Phys. Lett .*, 87(21):213505, 2005.

[135] Y. Wang, R. Hu, G. Lin, I. Roy, and K. T. Yong. Functionalized quantum dots for biosensing and bioimaging and concerns on toxicity. *ACS Appl. Mater. Interfaces*, 5(8):2786–2799, 2013.

[136] K. Huang, W. Lu, X. Yu, C. Jin, and D. Yang. Highly pure and luminescent graphene quantum dots on silicon directly grown by chemical vapor deposition. *Part. Part. Syst. Charact.*, 33(1):8–14, 2016.

[137] S. Dhawan, T. Dhawan, and A. G. Vedeshwar. Growth of nb_2o_5 quantum dots by physical vapor deposition. *Materials letters*, 126(1):32–35, 2014.

[138] Y. Yin and A. P. Alivisatos. Colloidal nanocrystal synthesis and the organic-inorganic interface. *Nature*, 437(7059):664–670, 2005.

[139] M. Nirmal, B. O. Dabbousi, M. G. Bawendi, J. J Macklin, J. K. Trautman, T. D. Harris, and L. E. Brus. Fluorescence intermittency in single cadmium selenide nanocrystals. *Nature*, 282:802–804, 1996.

[140] P. Reiss, M. Protiere, and L. Li. Core/shell semiconductor nanocrystals. *Small*, 5(2):154–168, 2009.

[141] H. Htoon, A. V. Malko, D. Bussian, J. Vela, Y. Chen, J. A. Hollingsworth, and V. I. Klimov. Highly emissive multiexcitons in steady-state photoluminescence of individual "giant" cdse/cds core/shell nanocrystals. *Nano Letters*, 10(7):2401–2407, 2010.

[142] C. Javaux, B. Mahler, B. Dubertret, A. Shabaev, A. V. Rodina, A. L. Efros, D. R. Yakovlev, F. Liu, M. Bayer, G. Camps, L. Biadala, S. Buil, X. Quelin, and J. P. Hermier. Thermal activation of non-radiative auger recombination in charged colloidal nanocrystals. *Nature Nanotechnology*, 8(3):206–212, 2013.

[143] Y. S. Park, A. V. Malko, J. Vela, Y. Chen, Y. Ghosh, F. Garcia-Santamarı, J. A. Hollingsworth, V. I. Klimov, and H. Htoon. Near-unity quantum yields of biexciton emission from cdse/cds nanocrystals measured using single-particle spectroscopy. *Phys. Rev. Lett.*, 106(18):187401, 2011.

[144] O. Chen, J. Zhao, V. P. Chauhan, J. Cui, C. Wong, D. K. Harris, H. Wei, H. S. Han , D. Fukumura, R. K. Jain, and M. G. Bawendi. Compact high-quality cdse-cds core-shell nanocrystals with narrow emission linewidths and suppressed blinking. *Nature Materials*, 12(5):445–451, 2013.

[145] D. Vasudevan, R. R. Gaddam, A. Trinchi, and I. Cole. Core-shell quantum dots: Properties and applications. *Journal of Alloys and Compounds*, 636:395–404, 2015.

[146] X. Wang, Z. Li, J. Shi, and Y. Yu. One-dimensional titanium dioxide nanomaterials: Nanowires, nanorods, and nanobelts. *Chem. Rev.*, 114(19):9346–9384, 2014.

[147] C. K. Chan, H. Peng, G. Liu, K. McIlwrath, X. F. Zhang, R. A. Huggins, and Y. Cui. High-performance lithium battery anodes using silicon nanowires. *Nature Nanotechnology*, 3(1):31–35, 2008.

[148] M. Law, L. E. Greene, J. C. Johnson, R. Saykally, and P. Yang. Nanowire dye-sensitized solar cells. *Nature Materials*, 4(6):455–459, 2005.

[149] S. W. Boettcher, J. M. Spurgeon, M. C. Putnam, E. L. Warren, D. B. Turner-Evans, M. D. Kelzenberg, J. R. Maiolo, H. A. Atwater, and N. S. Lewis. Energy-conversion properties of vapor-liquid-solid-grown silicon wire-array photocathodes. *Science*, 327(5962):185–187, 2010.

[150] Y. Xia, P. Yang, Y. Sun, Y. Wu, B. Mayers, B. Gates, Y. Yin, F. Kim, and H. Yan. One-dimensional nanostructures: Synthesis,characterization, and applications. *Adv. Mater.*, 15(5):353–389, 2003.

[151] J. Jiea, W. Zhang, I. Belloa, C. S. Leea, S. T. Lee. One-dimensional ii–vi nanostructures: Synthesis, properties and optoelectronic applications. *Nano Today*, 5(4):313–336, 2010.

[152] G. C. Yi, C. Wang, and W. I. Park. Zno nanorods: Synthesis, characterization and applications. *Semicond. Sci. Technol.*, 20:S22–S34, 2005.

[153] M. D. Tessier, C. Javaux, I. Maksimovic, V. Loriette, and B. Dubertret. Spectroscopy of single cdse nanoplatelets. *ACS Nano*, 6(8):6751–6758, 2012.

[154] C. She, I. Fedin, D. S. Dolzhnikov, P. D. Dahlberg, G. S. Engel, R. D. Schaller, and D. V. Talapin. Red, yellow, green and blue amplified spontaneous emission and lasing using colloidal cdse nanoplatelets. *ACS Nano*, 9(10):9475–9485, 2015.

[155] E. Lhuillier, J.-F. Dayen, D. O. Thomas, A. Robin, B. Doudin, and B. Dubertret. Nanoplatelets bridging a nanotrench : a new architecture for photodetectors with increased sensitivity. *Nano Lett.*, 15(3):1736–1742, 2015.

[156] B. Guzelturk, Y. Kelestemur, M. Olutas, S. Delikanli, and H. V. Demir. Amplified spontaneous emission and lasing in colloidal nanoplatelets. *ACS Nano*, 8(7):6599–6605, 2014.

[157] W. Cheng, G. Zeng, and M. Niederberger. Design of vanadium oxide core-shell nanoplatelets for lithium ion storage. *J. Mater. Chem. A*, 3(6):2861–2868, 2015.

[158] M. Li, M. Zhi, H. Zhu, W. Y. Wu, Q. H. Xu, M. H. Jhon, and Y. Chan. Ultralow-threshold multiphoton-pumped lasing from colloidal nanoplatelets in solution. *Nature Communications*, 6:1–8, 2015.

[159] S. Dong, J. Lian, M. H. Jhon, Y. Chan, and Z. H. Loh. Pump-power dependence of coherent acoustic phonon frequencies in colloidal cdse/cds core/shell nanoplatelets. *Nano Lett.*, 17(5):3312–3319, 2017.

[160] A. Polovitsyn, Z. Dang, J. L. Movilla, B. Martin-Garcia, A. H. Khan, G. H. V. Bertrand, R. Brescia, and I. Moreels. Synthesis of air-stable cdse/zns core/shell nanoplatelets with tunable emission wavelength. *Chem. Mater.*, 29(13):5671–5680, 2017.

[161] R. S. Koster, C. Fang, A. van Blaaderen, M. Dijkstraa, and M. A. van Huis. Acetate ligands determine the crystal structure of cdse nanoplatelets – a density functional theory study. *Phys. Chem. Chem. Phys.*, 18(32):22021–22024, 2016.

[162] E. Lhuillier, S. Pedetti, S. Ithurria, B. Nadal, H. Heuclin, and B. Dubertret. Two-dimensional colloidal metal chalcogenides semiconductors: Synthesis, spectroscopy, and applications. *Acc. Chem. Res.*, 48(1):22–30, 2015.

[163] J. W. Thomson, K. Nagashima, P. M. Macdonald, and G. A. Ozin. From sulfur-amine solutions to metal sulfide nanocrystals: Peering into the oleylamine-sulfur black box. *J. Am. Chem. Soc.*, 133(13):5036–5041, 2011.

[164] S. Pedetti. Synthesis and optical properties of ii-iv colloidal two dimensional nanocrystals: homo- and hetero-structures. *PhD Thesis of Pierre and Marie Curie University (University of Paris VI).*, 2016.

[165] A. L. Chuang. Physics of photonic devices. *Wiley*, 2012.

[166] L. Biadala, F. Liu, M. D. Tessier, D. R. Yakovlev, B. Dubertret, and M. Bayer. Recombination dynamics of band edge excitons in quasi-two-dimensional cdse nanoplatelets. *Nano Lett.*, 14(3):1134–1139, 2014.

[167] A. Cyphersmith, K. Early, A. Maksov, J. Graham, Y. Wang and M. Barnes. Nanoplatelets bridging a nanotrench : a new architecture for photodetectors with increased sensitivity. *Appl. Phys. Lett.*, 97(12):121915, 2010.

[168] S. Vezzoli, M. Manceau, G. Lemenager, Q. Glorieux, E. Giacobino, L. Carbone, M. De Vittorio, and A. Bramati. Exciton fine structure of cdse/cds nanocrystals determined by polarization microscopy at room temperature. *ACS Nano*, 9(8):7992–8003, 2015.

Résumé

Le contrôle et l'optimisation des propriétés d'émission des nanomatériaux peuvent être obtenus par un couplage efficace entre nanoémetteurs et nanostructures permettant d'obtenir une directivité plus élevée, une dynamique d'émission plus rapide. Il est pour cela nécessaire d'obtenir l'accord spectral de l'émetteur avec les modes de nanostructures, le positionnement spatial du nanoémetteur à l'endroit où l'intensité du mode résonant de la nanostructure est maximale, et une orientation du dipôle nanoémetteur parallèle au champ électrique résonant. En plasmonique les résonances larges des modes permettent un accord spectral facile. L'accord spatial est plus difficile, mais des stratégies ont été mises en œuvre avec succès. Le contrôle de l'orientation du dipôle reste lui un défi. En plasmonique, par exemple, une interaction efficace ne peut être obtenue que pour des dipôles orthogonaux à la surface métallique. La détermination de l'orientation du dipôle émetteur est donc cruciale pour les dispositifs plasmoniques tels que les nano-antennes.

Dans ma thèse, j'ai contribué au développement d'une méthode polarimétrie visant à analyser le dipôle émetteur d'un nanoémetteur et son orientation. J'ai effectué des expériences et les ai analysées. Le modèle décrit l'émission d'un dipôle proche d'une interface plane dans un large éventail de conditions expérimentales réalistes, en particulier le cas où le nanoémetteur se trouve à proximité d'un film d'or. Dans cette situation, pour des nanocristaux de CdSe/CdS assimilable à deux dipôles orthogonaux dégénérés, l'imagerie défocalisée n'est pas suffisamment sensible pour fournir des informations quantitatives fiables sur l'orientation de l'émetteur. A contrario, la polarimétrie permet de répondre à cette question. Avec le même modèle, le diagramme d'émission correspondant à l'émission dipolaire en champ lointain pour toutes ces conditions expérimentales a été calculé. En combinant la polarimétrie et l'étude des diagrammes de rayonnement, on peut obtenir des informations sur la structure dipolaire et l'orientation des dipôles. J'ai appliqué cette méthode pour étudier les nanoplaquettes semi-conductrices colloïdales de CdSe/CdS avec différentes formes géométriques : plaquettes carrées minces, plaquettes rectangulaires minces et plaquettes cubiques. J'ai établi une relation entre les structures géométriques des plaquettes et la nature et l'orientation de leurs dipôles émetteurs associés.

Summary

Control and optimization of nanomaterial emission properties, can be obtained thanks to efficient coupling between nanoemitters and nanostructures for achieving higher directivity, quicker dynamics. The requirements are the spectral tuning of the emitter to the nanostructures modes, the spatial positioning of the nanoemitter at the location of maximum intensity of the resonant nanostructure mode, and a proper orientation of the dipole nanoemitter. In plasmonics, the spectrally broad resonances make the spectral tuning easy. Whereas for spatial tuning, many strategies have been implemented successfully, the control of the dipole orientation remains a challenge. In plasmonics, for example, efficient interaction can only be achieved for dipoles orthogonal to the metallic surface. The determination of the orientation of the emitting dipole is thus very crucial for plasmonic devices such as nanoantennas.

In my thesis, I contributed to the development of a polarimetric method aiming at the analysis of a nanoemitter's emitting dipole and its orientation. I performed experiments and analyzed them. The model I used describes the emission of a dipole close to a plane interface in a wide range of realistic experimental conditions, including a very common case in plasmonics when the nanoemitter lies close a gold film. In this situation for CdSe nanocrystals which can be considered as two orthogonal degenerated emitting dipoles, the more standard defocused imaging method is not sufficiently sensitive to provide reliable quantitative information on the emitter's orientation. With the same model, I also computed the emission diagram corresponding to the dipolar emission in far field for all these experimental conditions. By analyzing the emission's polarization together with the emission pattern, I could determine the three-dimensional orientation of an emitting dipole. I applied this method to investigate the dipolar structure and orientation of colloidal semiconducting CdSe/CdS nanoplatelets with different geometries: thin square platelets, thin rectangular platelets, and cubic platelets. I established a relationship between the geometric structures of the platelets and the dimensionality and orientation of their associated emitting dipoles.

List of Figures